

DEVELOPMENT, OPTIMIZATION AND EVALUATION OF TUMOR-SPECIFIC  
NANOSPONGE DRUG DELIVERY SYSTEMS AS CHEMOTHERAPEUTICS

By

Ghazal Hariri

Dissertation

Submitted to the Faculty of the  
Graduate School of Vanderbilt University  
in partial fulfillment of the requirements

for the degree of

DOCTOR OF PHILOSOPHY

in

Chemical and Physical Biology

December, 2014

Nashville, Tennessee

Committee:

Dr. Eva M. Harth

Dr. David Hachey

Dr. H. Charles Manning

Dr. Lawrence J. Marnett

Dr. Andries Zijlstra

*To my grandmother*

## ACKNOWLEDGEMENTS

I would like to thank the members of my committee for their incredible support over the years. They graciously provided me with their time, expertise, and encouragement. I would like to thank my mentor Dr. Eva Harth for providing me with a great project and letting me conduct interdisciplinary research in her laboratory. I would like to thank Dr. Andries Zijlstra, Dr. Larry Marnett, Dr. Charles Manning and Dr. Dave Hachey for their scientific insight and expertise. It was a privilege to have each of them on my committee. In addition I would like to thank Dr. Bruce Damon, Dr. Hassane Mchaourab and the Chemical and Physical Biology program for their guidance and wonderful support. Special thanks to Lindsay Meyers for her time and help with navigating the program.

Analytical drug quantification was performed with the assistance of Dr. Wade Calcutt and the Mass Spectrometry Core Laboratory. I would like to acknowledge the members of the Cell Imaging shared resource for training and assistance with numerous imaging sessions. Confocal imaging and data analysis was performed with the assistance of Dr. Bob Matthews, Dr. Sam Wells, and Carol Ann Bonner. Transmission electron microscopy was performed with the assistance of Dr. Janice Williams and Matthew Stephenson. In particular, Dr. Jay Jerome provided many helpful discussions regarding electron microscopy. Flow cytometry studies were performed with the Flow Cytometry Core laboratory and I thank Dave Flaherty, Brittany Matlock and Chris Warren for their time, help and support.

Funding was generously provided through the following grants: NCI 5R01 CA112385-05, NIBIB R21 EB009223-01, NSF CHE-0645737, ICMIC P50 funds, and Vanderbilt Institute for Clinical and Translational Research. In addition I would like to thank Dr. Dennis Hallahan of Washington University for funding and support through NCI 5R01 CA112385-05 for the HVGGSSV project.

I would like to thank the members of the Harth group, past and present for their help and support. In addition, I would like to thank Dr. Alice van der Ende for her guidance and patience when I first joined the lab and picked up this project. Alice was an excellent mentor, friend and chemist. I would also like to thank the Vanderbilt undergraduate students who contributed to this project: Tyler Merrill, Josh Greenbaum and Sam Weiner. They always came to lab ready to help with whatever needed. In addition, many summer students also contributed to different aspects of this project over the years. Aaron Edwards (Centre College) helped with animal studies and imaging, Petar Stupar (U. Belgrade, Serbia) with cyclic peptides, and Emily Douglass (Lipscomb) with optimization of thiol-ene click reactions.

Finally, I would like to express my gratitude to my friends for their encouragement and company throughout my studies. They have made my time here enjoyable and filled me up with their positive attitude. I am grateful for my wonderful family, in particular, my grandmother who inspired me to go after my dreams in life and make them real. This work is dedicated in her loving memory.

## ABSTRACT

Current chemotherapeutic treatments for cancer utilize systemic administration of cytotoxic drugs and produce many side effects in healthy tissues, making optimal treatment of cancer hard to achieve. Tumor targeted chemotherapy treatment enables these drugs to selectively treat cancer cells with minimal effect on healthy tissues. By using targeting agents that specifically recognize receptors present only on cancer cells and neovasculature, tumor-specific chemotherapy can be achieved. These targeting agents can be used to direct nanoparticle drug delivery carriers in order to deliver greater drug doses to tumor tissue, enhance bioavailability, pharmacokinetics and pharmacodynamics of many chemotherapy drugs, as well as reduce toxicity and undesirable side effects *in vivo*.

The development, optimization and evaluation of tumor-specific drug delivery systems composed of second generation ‘nanosponges’ has been investigated as a potential therapeutic for the treatment of lung cancer. This drug delivery system is hypothesized to optimize bioavailability and therapeutic efficacy of chemotherapy drugs in tumors, reduce side effects in normal tissues, and result in improved cancer treatment. These nanosponges have been developed from optimized linear polyester copolymers using tin (II) triflate catalyzed ring-opening polymerization methods. They contain functional groups for modification with targeting and imaging agents in order to both target malignant tumor cells as well as visualize them *in vitro* and *in vivo*. Tumor targeting peptides such as cyclo-RGD that target the  $\alpha_v\beta_3$  integrin receptor, and the HVGGSSV peptide that target radiation-inducible tax-interacting protein 1 receptor allow for tumor-specific targeting of nanosponges. These nanosponges enable

controlled linear drug release of small molecule chemotherapeutics that can optimize combination chemotherapy strategies for the treatment of lung cancer.

Due to their biodegradability, high encapsulation efficiency, and sustained linear drug release profiles, these optimized nanosponges are ideal for the encapsulation and controlled release of chemotherapy drugs. The applicability of a HVGGSSV peptide targeted nanosponge drug delivery system for sequential administration of a microtubule inhibitor (paclitaxel) and topoisomerase I inhibitor (camptothecin) was investigated in a lung cancer mouse model. Combination therapy with these two drugs will allow for multiple mechanisms of action for inhibiting cancer growth, resulting in enhanced cytotoxicity when delivered in varying sequences.

## TABLE OF CONTENTS

	Page
DEDICATION.....	ii
ACKNOWLEDGEMENTS.....	iii
ABSTRACT.....	v
LIST OF FIGURES.....	ix
LIST OF SCHEMES.....	xii
LIST OF ABBREVIATIONS.....	xiii
Chapter	
I. INTRODUCTION.....	1
Cancer Chemotherapy .....	1
Nanotechnology for Targeting, Imaging and Therapy.....	2
Nanoparticle Materials.....	3
Nanoparticle Cancer Therapeutics.....	6
Tumor Targeting.....	10
Molecular Imaging .....	12
Drug Quantification.....	15
Summary.....	16
References.....	18
II. SYNTHESIS OF SECOND GENERATION POLYESTER ‘NANOSPONGES’ VIA RING-OPENING POLYMERIZATION WITH TIN (II) TRIFLATE CATALYST	
Abstract.....	26
Introduction.....	27
Polymers for Drug Delivery.....	27
Ring-opening Polymerization.....	28
Material Properties.....	28
Catalyst Optimization.....	30
Experimental.....	32
Results and Discussion.....	36
Conclusion.....	51

References.....	52
III. NANOSPONGE DRUG ENCAPSULATION, RELEASE AND IN VITRO CELL STUDIES	
Abstract.....	57
Introduction.....	58
Drug Delivery Systems.....	58
Drug Combinations.....	59
Experimental.....	61
Results and Discussion.....	67
Conclusions.....	75
References.....	76
IV. SYNTHESIS AND BIOLOGICAL EVALUATION OF CYCLIC RGDEKf-Ahx-C FUNCTIONALIZED NANOSPONGES FOR IN VITRO TUMOR TARGETING AND IMAGING	
Abstract.....	80
Introduction.....	81
Integrins as Therapeutic Agents.....	81
RGD Peptide Ligands.....	81
Linear vs. Cyclic RGD Peptides.....	82
Synthesis and Optimization of RGD Peptides.....	82
Integrin Targeted Tumor Imaging.....	83
Experimental.....	85
Results and Discussion.....	91
Conclusions.....	97
References.....	98
V. IN VIVO TARGETING AND EFFICACY STUDIES WITH NANOSPONGES IN A MOUSE MODEL OF LUNG CANCER	
Abstract.....	101
Introduction.....	102
Experimental.....	105
Results and Discussion.....	116
Conclusions.....	128
References.....	129
VI. CONCLUSION AND FUTURE OUTLOOK.....	135
Appendix.....	140



## LIST OF FIGURES

Figure	Page
1.1 Nanotheranostics combine nanotechnology with therapy and diagnosis for oncology applications.....	3
1.2 Structures of paclitaxel and camptothecin chemotherapy drugs.....	8
1.3 Nanoparticle drug delivery systems approved by the United States Food and Drug Administration for treatment of cancer .....	9
1.4 Absorption at near-infrared wavelengths by common biological molecules.....	14
2.1 Commonly used cyclic ester monomers for ring-opening polymerization of polyesters.....	29
2.2 Ring-opening polymerization with tin (II) triflate catalyst.....	31
2.3 <sup>1</sup> H NMR of $\alpha$ -allyl- $\delta$ -valerolactone monomer in CDCl <sub>3</sub> .....	37
2.4 <sup>1</sup> H NMR of 2-oxepane-1,5-dione monomer in CDCl <sub>3</sub> .....	38
2.5 <sup>1</sup> H NMR of poly(VL- <i>co</i> -AVL) linear polymer in CDCl <sub>3</sub> .....	40
2.6 Characterization of poly(VL- <i>co</i> -AVL) linear copolymer.....	41
2.7 <sup>1</sup> H NMR of poly(VL- <i>co</i> -AVL- <i>co</i> -EVL) precursor in CDCl <sub>3</sub> .....	43
2.8 Characterization of poly(VL- <i>co</i> -AVL- <i>co</i> -EVL) copolymer.....	44
2.9 Characterization of poly(VL- <i>co</i> -AVL- <i>co</i> -OPD) linear copolymer.....	45
2.10 <sup>1</sup> H NMR of nanoparticles in DMSO- <i>d</i> <sub>6</sub> .....	47
2.11 Diagram of nanosponge formation via intermolecular crosslinking of poly(VL- <i>co</i> -AVL) linear copolymers with a diamine crosslinker.....	48
2.12 Size characterization of nanosponges made from tin (II) triflate.....	49
2.13 DSC analysis of poly(VL- <i>co</i> -AVL- <i>co</i> -EVL- <i>co</i> -OPD) nanosponges.....	50

<b>3.1</b>	Phases of the cell cycle.....	59
<b>3.2</b>	Drug release studies with poly(VL- <i>co</i> -AVL- <i>co</i> -EVL) nanosponges .....	68
<b>3.3</b>	MTT cytotoxicity assays with poly(VL- <i>co</i> -AVL- <i>co</i> -EVL) nanosponges.....	69
<b>3.4</b>	Flow cytometry studies of cell cycle distributions in LLC cells treated with dual drug combinations.....	70
<b>3.5</b>	Sequential treatment with NP-paclitaxel before NP-camptothecin tubulin polymerization.....	73
<b>3.6</b>	Flow cytometry analysis of caspase-dependent cell death in Lewis lung carcinoma cells.....	74
<b>4.1</b>	Thiol-ene ‘click’ reaction using DMPA photoinitiator.....	93
<b>4.2</b>	Photoinitiated thiol-ene ‘click’ attachment of cyclic RGD peptide to nanosponges.....	94
<b>4.3</b>	Imaging RGDEKf-Ahx-C-NP-AF488 binding to cells .....	95
<b>4.4</b>	Imaging vitronectin competition studies with RGD peptide.....	96
<b>5.1</b>	Synthesis of polyester nanoparticles functionalized with HVGGSSV targeting peptide, Alexa Fluor <sup>®</sup> 750 near-infrared fluorophore imaging agents, and Nanogold <sup>®</sup> .....	117
<b>5.2</b>	Near-infrared (NIR) fluorescence imaging of HVGGSSV-NPs in an LLC model at 24 hrs post-injection.....	118
<b>5.3</b>	TEM micrographs of LLC tumors treated with Nanogold <sup>®</sup> labeled HVGGSSV-NPs in a murine model at 24 hrs post-injection.....	119
<b>5.4</b>	Tumor growth delay analysis of HVGGSSV peptide targeted nanoparticles loaded with paclitaxel or camptothecin.....	121
<b>5.5</b>	Quantification of paclitaxel and camptothecin content in LLC tumor tissues.....	122
<b>5.6</b>	Immunohistochemical analysis of cell proliferation.....	123
<b>5.7</b>	Immunohistochemical analysis of cell death.....	124

**5.8** Immunohistochemical analysis of tumor vascularity.....125

## LIST OF SCHEMES

Scheme	Page
2.1 Synthesis of $\alpha$ -allyl- $\delta$ -valerolactone monomer (AVL).....	37
2.2 Synthesis of 2-oxepane-1,5-dione monomer (OPD).....	38
2.3 Preparation of poly(VL- <i>co</i> -AVL) copolymer.....	39
2.4 Preparation of poly(VL- <i>co</i> -AVL- <i>co</i> -OPD) copolymer.....	42
2.5 Preparation of poly(VL- <i>co</i> -AVL- <i>co</i> -EVL) copolymer .....	42
2.6 Synthesis of poly(VL- <i>co</i> -AVL- <i>co</i> -EVL) nanoparticles.....	46
4.1 Solid phase peptide synthesis and structure of cyclic RGDEKf-Ahx-C peptide.....	92

## LIST OF ABBREVIATIONS

ACN	acetonitrile
AF	Alexa Fluor <sup>®</sup>
AVL	$\alpha$ -allyl- $\delta$ -valerolactone
$\alpha_v\beta_3$	alpha v beta 3 integrin receptor
Å	Angström
A549	human lung adenocarcinoma cell line
CCD	charge-coupled device
CD31	endothelial cell marker
CDCl <sub>3</sub>	deuterated chloroform
COMU	(1-Cyano-2-ethoxy-2-oxoethylideneaminoxy)dimethylamino-morpholino-carbenium hexafluorophosphate
CPT	camptothecin
cRGD	tumor targeting cyclic RGD (Arg-Gly-Asp) peptide
C57BL6	inbred mouse strain
°	degrees
°C	degrees Celsius
$\delta$	delta
Da	Daltons
DAPI	4',6-diamidino-2-phenylindole
DCM	dichloromethane
DIPEA	N,N-diisopropylethylamine
DLS	dynamic light scattering

DMEM	Dulbecco's modified Eagle medium
DMF	dimethylformamide
DMPA	2,2-dimethoxy-2-phenylacetophenone
DMSO	dimethyl sulfoxide
DMSO-d <sub>6</sub>	deuterated dimethyl sulfoxide
DNA	deoxyribonucleic acid
DSC	differential scanning calorimetry
EGFR	epidermal growth factor receptor
EPR	enhanced permeability and retention effect
EtOH	ethanol
EVL	epoxyvalerolactone
FBS	fetal bovine serum
FDA	U.S. Food and Drug Administration
FITC	fluorescein isothiocyanate
Fmoc	Fluorenylmethyloxycarbonyl
g	gram
G <sub>0</sub>	resting phase in cell cycle
G <sub>1</sub>	pre-synthesis phase in cell cycle
G <sub>2</sub>	pre-mitosis phase in cell cycle
Gy	Gray
GPC	gel permeation chromatography
<sup>1</sup> H NMR	proton nuclear magnetic resonance
HMPA	hexamethylphosphoramide

HOBt	N-hydroxybenzotriazole
HPLC	high performance liquid chromatography
HPLC/MS	HPLC tandem mass spectrometry
hrs	hours
Hz	hertz
HVGGSSV	tumor targeting peptide (His-Val-Gly-Gly-Ser-Ser-Val)
IACUC	Institutional Animal Care and Use Committee
IC <sub>50</sub>	inhibitory concentration 50
i.v.	intravenous
IR	irradiated
kDa	kilodalton
Ki67	cell proliferation marker
kV	kilovolts
$\lambda$	lambda
L	liter
LLC	murine Lewis lung carcinoma cell line
M	mitosis phase in cell cycle
M	moles per liter
mCPBA	meta-Chloroperoxybenzoic acid
MDR	multidrug resistance
MeOH	methanol
mg	milligram
mg/kg	milligram per kilogram

mg/mL	milligram per milliliter
MHz	megahertz
min	minute
mL	milliliter
mL/min	milliliter per minute
mm	millimeter
mmol	millimole
mM	millimolar
mol	mole
M <sub>w</sub>	weight-average molecular weight
MWCO	molecular weight cut-off
MTT	3-(4,5-Dimethylthiazol-2-yl)-2,5-diphenyltetrazolium bromide
mV	millivolt
m/z	mass-to-charge ratio
NaCl	sodium chloride
n-BuLi	n-butyl lithium
NH <sub>4</sub> Cl	ammonium chloride
NHS	N-hydroxysuccinimidyl
NIR	near-infrared
nab	nanoparticle albumin-bound
nm	nanometer
NP	nanoparticle
NMR	nuclear magnetic resonance



nu/nu	nude mouse
OPD	2-oxepane-1,5-dione
ODmab	$\alpha$ -4- {N-[1-(4,4-dimethyl-2,6-dioxocyclohexylidene)-3-methylbutyl]-amino} benzyl ester
PBL	poly(butyrolactone)
PBS	phosphate-buffered saline
PC-3	human prostate adenocarcinoma cell line
PCL	poly(caprolactone)
PDI	polydispersity index
PEG	polyethylene glycol
PET	positron emission tomography
pH	potential hydrogen
PGA	poly(glycolic acid)
PLA	poly(lactic acid)
PLGA	poly(lactic- <i>co</i> -glycolic acid)
ppm	parts per million
PVL	poly(valerolactone)
PTX	paclitaxel
RGD	tumor targeting Arg-Gly-Asp peptide
ROI	region of interest
ROP	ring-opening polymerization
RP-HPLC	reverse phase HPLC
rpm	revolutions per minute

RT	radiation treatment
S	DNA synthesis phase in cell cycle
s.c.	subcutaneous
SE	standard error
Sn(Oct) <sub>2</sub>	tin(II) octanoate
Sn(OTf) <sub>2</sub>	tin(II) trifluoromethanesulfonate or triflate
T	temperature
T <sub>c</sub>	crystallization temperature
T <sub>g</sub>	glass transition temperature
T <sub>m</sub>	melting temperature
TEM	transmission electron microscopy
TFA	trifluoroacetic acid
THF	tetrahydrofuran
TIP-1	tax-interacting protein 1
TMS	trimethylsilane
μg	microgram
μL	microliter
μM	micromolar
μm	micrometer
μmol	micromole
UV	ultraviolet
UV-Vis	ultraviolet-visible spectroscopy
VEGF	vascular endothelial growth factor
vitamin E TPGS	D-α-tocopherol polyethylene glycol 1000 succinate

VL	$\delta$ -valerolactone
vWF	von Willebrand factor
W	Watts

## CHAPTER 1

### INTRODUCTION

#### *Cancer chemotherapy*

The majority of cancers diagnosed are solid tumors that can be surgically resected, however, remaining malignant cells are difficult to detect and remove and can potentially spread after surgical treatment.<sup>1-4</sup> Chemotherapy and radiotherapy are commonly used as second line treatments to eradicate remaining cancer cells after surgery, and in cases where surgery is not possible as first line treatments.<sup>1</sup> Achieving complete eradication of cancer cells has proven to be a challenge due not only to metastatic cells, but also to poor bioavailability of commonly used chemotherapy drugs, limited dosing due to toxicity, damage to normal tissues as a result of systemic administration of cytotoxic drugs, multidrug resistance (MDR), and low solubility of hydrophobic drugs under physiologic conditions.<sup>1-8</sup> Current chemotherapy regimens require systemic administration of cytotoxic drugs intravenously, with multiple rounds of treatment usually needed. Achievement of a high enough dose to kill the cancer while maintaining tolerability to the patient remains a challenge.<sup>1-8</sup> Additionally, many cancer patients are immunocompromised and the elevated toxicity resulting from certain treatment regimens is not well tolerated, possibly even contributing to patient mortality.<sup>1-8</sup> Typical cancer drugs are also highly hydrophobic and suffer from poor water solubility, requiring them to be administered along with a pharmaceutical grade solvent (such as castor oil, ethanol, and surfactants).<sup>2-8</sup> These solubility enhancing solvents cause severe allergic reactions and other undesirable side effects in patients, making them difficult to tolerate for immunocompromised cancer patients.<sup>2-8</sup> As a

result, systemic chemotherapy continues to have major drawbacks that impact treatment outcomes, patient survival and quality of life. Alternative formulations and drug delivery systems have been actively investigated to circumvent these problems. Nanoparticle drug delivery provides advantages over systemic ‘free’ drug treatment by allowing for more effective therapeutic doses to be administered while mitigating many of the side effects.

### ***Nanotechnology for targeting, imaging and therapy***

Development of nanoscale carriers for treatment of cancer has been of particular interest since the use of nanoparticles for delivery of chemotherapeutics to malignant tumors offers solutions to the problems associated with chemotherapy administration, dosing and formulation issues.<sup>2-8</sup> Nano-sized carriers are ideal for delivering drugs and imaging agents because they can control the release of drug locally, target surface receptors on cancer cells and neovasculature, and allow imaging of biodistribution *in vivo*.<sup>2-8</sup> These multifunctional ‘nanotheranostics’ can simultaneously deliver and release therapeutic agents, and be used as contrast agents for molecular imaging, making them ideal for both therapy and diagnosis (Figure 1.1).<sup>5,6</sup> This versatile nanoparticle is particularly suited to applications where treatment must be adapted to the continuously changing needs of the patient throughout the course of treatment. Additionally, it allows for greater convenience for patients with a single treatment serving multiple functions. The ability to monitor the effectiveness of treatment using imaging technology is also of huge benefit to physicians as it allows for optimized treatment protocols, and greater flexibility for switching from ineffective drugs to more effective ones in a timely manner.

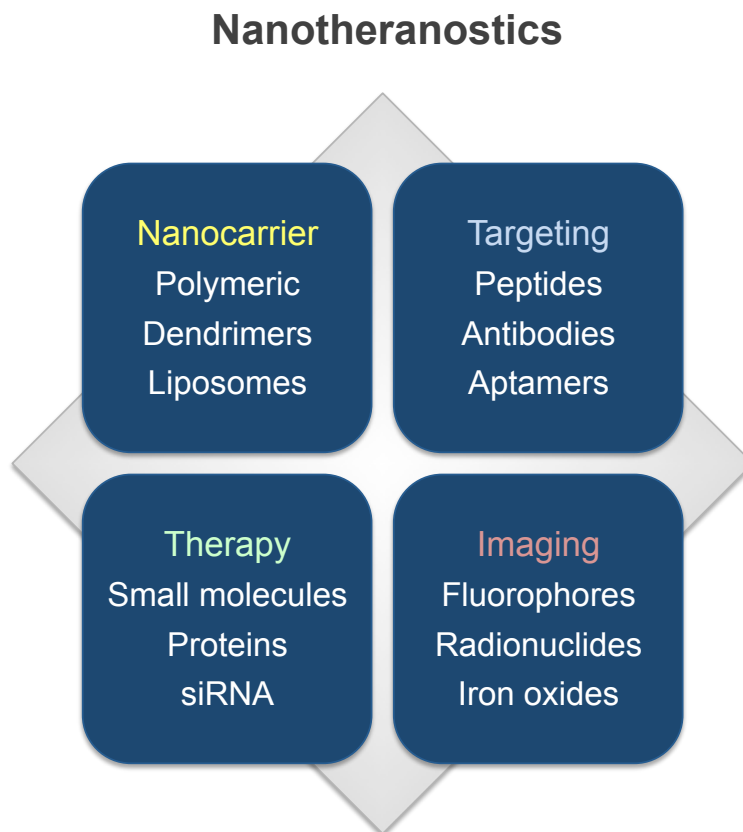


**Figure 1.1.** Nanotheranostics combine nanotechnology with therapy and diagnosis.

### *Nanoparticle materials*

Nanoparticles have been made from many different materials including synthetic and natural polymers, lipids, metals and other inorganic materials. Examples of nanoparticles formed from polymers include polymer-drug conjugates, micelles, dendrimers, and nanogels.<sup>2-8</sup> Depending on the application and physiological environment, materials can be rationally designed to enhance biocompatibility as well as optimize physicochemical properties.

Biodegradable polymers have been frequently used for the design of nanoparticles for drug delivery applications since they can degrade under physiological conditions, gradually release drug in a time-dependent manner, and are physiologically compatible.<sup>11,14,16,57</sup> In order for a polymer to be considered ‘biodegradable’, it must be capable of undergoing either

hydrolytic, enzymatic or oxidative degradation processes.<sup>11,4,16</sup> Hydrolytic and enzymatic degradation typically occur under physiological conditions given the abundance of water molecules and enzymes (such as hydrolases and esterases) available in blood and tissues, and are frequent degradation pathways for polymers used in the pharmaceutical industry.<sup>11,14,16</sup> Biocompatibility of these polymers is also important for polymers that remain *in vivo* for extended periods of time, thus the polymer itself and its degradation products must not be toxic or generate an immune response. Consequently, biodegradable polymers are highly suitable for delivering drugs due to greater biocompatibility and decreased immunogenicity, as well as controlled release of drugs via degradation.<sup>11,14,16</sup> In addition, functional groups can be built into these polymers to allow addition of targeting units such as peptides and antibodies, as well as imaging probes for visualization.<sup>11-19</sup> Depending on the polymer type, solubility and crystallinity can also be tuned to deliver unique polymers customized for specific applications.<sup>11-19, 68-70</sup>

A variety of biodegradable polymers have been previously studied including polyesters, polyanhydrides, polyurethanes, and polyacrylates.<sup>11,14,16</sup> These polymers can range from hydrophobic to hydrophilic, with varying degrees of hydrophobicity and hydrophilicity produced with copolymer composition. Of these, biodegradable polymers such as poly(lactide)-*co*-(glycolide) (PLGA) have been widely used for nanoparticle drug delivery systems due to controlled degradation and drug release properties and favorable biocompatibility profiles.<sup>10,20,67,82-85</sup> However, production of a sustained, linear drug release profile has been difficult to achieve in the past due to greater amounts of drug released initially (known as the ‘burst effect’).<sup>12-19</sup> Greater drug encapsulation efficiency, as determined by the amount of drug actually loaded into a nanoparticle compared to amount of drug attempted, has also made

biodegradable polymer-based nanoparticle preferable over other types of nanoparticles for drug delivery applications.<sup>10-20</sup>

The main advantage of using synthetic polymers for nanoparticles lies in their ability to be designed to accommodate particular applications. This “tunability” exploits the different properties of polymers and copolymer combinations to produce nanoparticles with desirable properties. Examples of properties that can be “tuned” include particle size, surface properties (charge, hydrophobicity, morphology, and functionalities) and payload density.<sup>2-8</sup> In addition, several of these factors such as size, surface modification and functionalization with targeting ligands can affect clearance and biodistribution of nanoparticles *in vivo*.<sup>2-8</sup> Nanoparticle size has been known to affect *in vivo* clearance, with a range of 10-120 nm considered an optimal range.<sup>2-8</sup> Nanoparticles smaller than 10 nm are rapidly cleared by the kidneys, while those in the upper size range can potentially get trapped within tumors via enhanced permeability and retention (EPR) effect.<sup>2-8</sup> Surface charge can also affect nanoparticle internalization within tumor tissue and cells, with a slight negative surface charge (-2 to -5 mV) allowing the nanoparticles to better penetrate into tumor cells.<sup>2-8</sup> Minimization of size and charge reduces scavenging by macrophages and the reticuloendothelial system (liver, spleen, lymph and bone marrow cells). Use of a neutral polymer such as polyethylene glycol (PEG) can also reduce surface charge, reduce aggregation caused by interactions between nanoparticles, and allow nanoparticles to evade the reticuloendothelial system and reduce immunogenicity (interaction with immune cells and provocation of an immune response).<sup>2-8</sup> In addition, surface modification with PEG increases circulation time. Hydrophobicity can be tuned in polymeric nanoparticles by altering the monomer type, polymer chain length and molecular weight, and addition of other modifiers such as PEG to enhance hydrophilicity.<sup>2-8,44-46</sup> Nanoparticle morphology can be affected by changes in



molecular arrangement, with variation in percent amorphous and crystalline regions producing changes in overall packing structure. Surface functionalities can be tuned with covalent attachment of peptides, antibodies, aptamers and other small molecule targeting ligands.<sup>2-8</sup> Surface density of these targeting ligands can be increased or decreased according to presence of functional groups available for bonding. Nanoparticles also enable multivalency, with multiple ligands on nanoparticle surfaces increasing likelihood of interaction with cell surface receptors.<sup>2-8,35-40</sup> Small molecules such as chemotherapy drugs, proteins and siRNA can be loaded within nanoparticles in varying degrees depending on nanoparticle size, porosity and hydrophobicity.

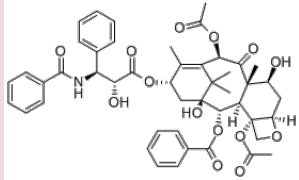
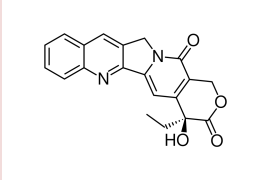
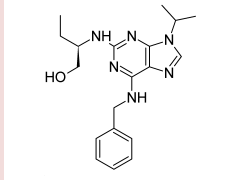
### ***Nanoparticle cancer therapeutics***

Nanoparticles are particularly useful for delivering small molecule drugs that are highly toxic, hydrophobic, and rapidly cleared *in vivo*. Use of nanoparticle carriers can safely solubilize these types of drugs, increase plasma half-life, deliver and release them within tumor tissues, vasculature and cells. One of the major benefits of using nanoparticles in drug delivery applications is not only increased deposition of drugs within tumors, but also reduced systemic exposure.<sup>2-8,35-48</sup> Toxic drugs have exposure limits that can prohibit treatment with optimal dosages needed for destruction of tumors. In order to avoid exceeding upper exposure limits and lethal toxicity levels, physicians are often forced to administer lower doses that may not be optimally effective. However, with nanoparticle drug delivery systems greater dosages can be achieved with lower side effects, allowing more optimal dosages to be administered with improved tolerability.<sup>2-8,35-48</sup> Nanoparticle drug delivery can also be used for neoadjuvant chemotherapy, reducing the size of a tumor before more radical treatments are performed.<sup>2-8</sup> This is important in cases where tumors in their original state are non-resectable due to close

proximity to major blood vessels, vital organs or extent of malignant tissue. Nanoparticle chemotherapy can allow more aggressive neoadjuvant treatments than systemic chemotherapy, potentially improving success of more radical treatments afterwards.<sup>2-8</sup>

Depending on the particular drug, dosage, and treatment schedule, nanoparticle materials can be modified to provide the desired characteristics. These might include encapsulation of hydrophobic drugs, various administration methods, biodegradability, controlled release, sustained release, and localized delivery of drug to maximize the therapeutic index and minimize systemic toxicity.<sup>2-8</sup> Problems that have been encountered with some polymeric nanoparticles include potential chemical instability, limited bioavailability, and lack of site specificity.<sup>10-16</sup> These problems are often addressed by modifying the polymer composition and incorporation of tumor-specific targeting ligands.<sup>13,35,54</sup> The design of the nanoparticles as well as their surface chemistry can be used to engineer nanoparticle carriers with properties that can enhance cancer treatment while minimizing side effects.

A variety of chemotherapy drugs have been encapsulated including paclitaxel, dexamethasone, 5-fluorouracil, and etoposide.<sup>2-20</sup> Applications for these types of drug delivery systems have increased over the last decade as more drugs have been encapsulated with greater efficiency. Highly hydrophobic drugs in particular have benefited from the development of biodegradable nanoparticles because they are difficult to solubilize for intravenous injection, and require use of a pharmaceutical grade solvent or surfactant. In this work, a nanoparticle drug delivery system comprised of biodegradable copolymers has been used to deliver the chemotherapeutic drugs paclitaxel and camptothecin due to their hydrophobicity and poor water solubility (Figure 1.2). In addition, a less hydrophobic drug, seliciclib, was also used for *in vitro* drug combination studies.

	Paclitaxel	Camptothecin	Seliciclib
<b>Structure</b>			
<b>Formula</b>	C <sub>47</sub> H <sub>51</sub> NO <sub>14</sub>	C <sub>20</sub> H <sub>16</sub> N <sub>2</sub> O <sub>4</sub>	C <sub>19</sub> H <sub>26</sub> N <sub>6</sub> O
<b>MW</b>	853.9	348.4	354.5
<b>Source</b>	Pacific Yew tree ( <i>Taxus brevifolia</i> )	Chinese happy tree ( <i>Camptotheca acuminata</i> )	synthetic small molecule
<b>Mechanism of Action</b>	mitotic inhibitor	topoisomerase I inhibitor	CDK (2,7,9) inhibitor
<b>Indication</b>	breast, lung, ovarian, head and neck cancer	ovarian, lung, colon cancer	lung cancer, leukemia, HIV, inflammation
<i>MW: molecular weight; CDK: cyclin-dependant kinase</i>			

**Figure 1.2.** Structures of chemotherapy drugs used in nanosponge drug delivery systems.

In clinical applications, paclitaxel has been administered using Cremophor<sup>®</sup> EL, a pharmaceutical grade solvent, in order to enhance water solubility.<sup>2-20</sup> However, low stability in circulation as well as significant side effects (neurotoxicity, hypersensitivity and allergic reactions) have made using these solvents undesirable and other formulations have been investigated. As a result, alternative nanoparticle formulations for taxanes have been developed and studied clinically including Abraxane<sup>®</sup>.<sup>2-20</sup> Abraxane<sup>®</sup> is an albumin-based nanoparticle used to deliver paclitaxel, initially approved by the FDA for use in the treatment of breast cancer in 2005, and also non-small cell lung cancer and pancreatic cancer in 2013 (Figure 1.3). Nanoparticle formulations of camptothecin have not been available on the market, but attempts have been made to modify the structure of camptothecin to enhance its water solubility, resulting in the analogues irinotecan and topotecan. Figure 1.3 shows other nanoparticle drug delivery

systems also approved by the United States FDA including several liposomal formulations for the anthracycline analogues doxorubicin (Doxil<sup>®</sup>) and daunorubicin (DaunoXome<sup>®</sup>), as well as vincristine (Marqibo<sup>®</sup>) and cytaribine (DepoCyt<sup>®</sup>).<sup>2-20</sup> PEGylated drug compounds have also been approved for L-asparaginase (Oncaspar<sup>®</sup>) and pegfilgrastim (Neulasta<sup>®</sup>) for blood cancers and disorders relating to chemotherapy.<sup>2-20</sup>

FDA Approved Nanoparticle Therapeutics for Cancer Treatment				
Drug Delivery System	Therapeutic Drug	Commercial Name	Indications	FDA Approval
Albumin-bound paclitaxel (nab)	Paclitaxel	Abraxane <sup>®</sup>	breast, non-small cell lung cancer, pancreatic cancer	2005, 2013
Liposomes	Vincristine	Marqibo <sup>®</sup>	Ph- acute lymphoblastic leukemia	2012
	Cytaribine	DepoCyt <sup>®</sup>	lymphomatous meningitis	2007
	Doxorubicin	Doxil <sup>®</sup>	Kaposi's sarcoma, ovarian cancer	1995, 1999
	Daunorubicin	DaunoXome <sup>®</sup>	Kaposi's sarcoma	1996
PEGylated drug	L-asparaginase	Oncaspar <sup>®</sup>	acute lymphoblastic leukemia	2006
	Pegfilgrastim	Neulasta <sup>®</sup>	neutropenia	2002

*FDA: food and drug administration; nab: nanoparticle albumin bound; Ph- : Philadelphia chromosome negative; PEG: polyethylene glycol; PLA: polylactic acid*

**Figure 1.3.** Nanoparticle drug delivery systems approved by the United States Food and Drug Administration for treatment of cancer.<sup>2-20</sup>

In this study, biodegradable nanosponges were used as nanocarriers to deliver chemotherapy drugs to tumors. Due to a cross-linked polymeric architecture, controlled low dose drug release profiles were produced that were highly suitable for this application.<sup>86-88</sup> Furthermore, development of a tumor-specific drug delivery system that enhanced drug solubility, provided sustained low dose drug release, and could be used with different drug combinations provided a unique opportunity for maximizing the potential of chemotherapy while reducing the limiting toxicities that lower treatment efficacy. Therefore, biodegradable nanosponges were optimized to target and treat tumors. Due to their biodegradable nano-network

(a cross-linked 3-dimensional scaffold), drug can be loaded into nanosponges and released in a controlled fashion upon degradation in physiological conditions. These nanoparticles can be synthesized in different sizes and network densities, and can be functionalized with tumor targeting ligands and imaging agents to enable visualization *in vivo*.<sup>86-88</sup> Moreover, hydrophobic drugs can be loaded into these nanosponges, enhancing solubility and producing formulations for parenteral administration.

### ***Tumor targeting***

In order to direct these nanoparticle carriers to specific sites, such as malignant tumors, targeting has played an increasingly important role in drug delivery systems. Both passive and active targeting strategies have been explored as ways to efficiently deliver drugs to tumors and enhance specificity.<sup>38-48</sup>

Passive targeting of drug delivery systems utilizes the enhanced permeability and retention (EPR) effect to selectively accumulate in tumors instead of other tissues.<sup>38-48</sup> By exploiting the greater permeability of tumor microvasculature and poor lymphatic drainage, nanoparticles greater than 50 kDa can be retained within tumor tissues.<sup>38-48</sup> Since this method of targeting does not require the use of targeting units but relies more on nanoparticle size and molecular weight, it is known as a *passive* targeting strategy. While this method is useful for delivering and trapping high molecular weight drugs within tumor tissues, it is not as effective for low molecular weight drugs due to rapid washout by tumor vascular blood flow.<sup>38-48</sup> In addition, variation between tumor types (and also within each individual tumor), size and location produces differences in blood vessel structure, and can impact treatment effectiveness.

Active targeting strategies require the use of receptor-ligand binding and are more specific in interaction and binding to tissue types and biomarkers for disease. Receptors present on the surface of cancer cells and their microvasculature can be targeted using peptides or antibodies that have high affinity and specificity for these receptors.<sup>38-48,63,64</sup> There are a variety of commonly used targets including the  $\alpha_v\beta_3$  integrin, tax-interacting protein 1 (TIP-1), epidermal growth factor receptor (EGFR), and vascular endothelial cell growth factor receptor (VEGF), among others.<sup>38-50,89-93</sup> Conjugation of peptides or antibodies that target these receptors can enable a nanoparticle to home specifically to tissues that express these receptors. Use of active over passive targeting strategies presents advantages including receptor specific binding, delivery of small molecule drugs independent of size, and greater concentration of drug within the tumor compared to normal organs.

Tumor-specific targeting using radiation-inducible receptors has been demonstrated in various tumor models.<sup>89-93</sup> Briefly, exposure of a solid tumor to sub-therapeutic levels of ionizing radiation is used to induce expression of receptors on tumor cells and neovasculature. Peptides developed using phage display technology can be targeted to these radiation-inducible receptors to enable tumor-specific binding.<sup>89-93,58-62</sup> Use of these peptides in conjunction with nanoparticles, small molecule therapeutics and contrast agents can produce radiation-targeted drug delivery and imaging systems for cancer treatment. In this work, the tax-interacting protein-1 (TIP-1) binding peptide (HVGSSV) was used as a targeting ligand for tumor-specific delivery of chemotherapeutic drugs and imaging agents.<sup>90-93</sup> This peptide was shown to bind to tumor cells exposed to a sub-therapeutic dose of 3 Gy ionizing radiation in lung, brain, breast, colon and prostate cancer models.<sup>90-93</sup> By targeting chemotherapy drugs specifically to tumor tissue, greater concentrations of drug can be delivered to tumors without exposing healthy tissues

to cytotoxic drugs. Toxic side effects produced from non-specific delivery often compromise cancer treatment because of damage to healthy tissues and decreased tolerance in patients, causing suboptimal dosages and treatment protocols. Furthermore, radiation is widely used in the majority of cancer treatments along with chemotherapy and surgery.<sup>1-8</sup> Technological and scientific advances have ensured accurate and efficient delivery of radiation dosages to tumor sites. Low dose radiation has also been reported to enhance drug delivery by inducing higher drug diffusion in solid tumors.<sup>1-8,90-93</sup> Since radiation can be used in combination with chemotherapy drugs to enhance biological efficacy, it can also be used in conjunction with radiation-targeted drug delivery systems to optimize therapeutic efficacy.

Another target for tumors is the  $\alpha_v\beta_3$  integrin adhesion receptor, a marker for angiogenesis. This integrin receptor has been widely used for both imaging and tumor targeted drug delivery, and it binds to a variety of peptides and proteins that contain the arginine-glycine-aspartic acid (RGD) recognition motif.<sup>48-50</sup> In particular, radiolabeled  $\alpha_v\beta_3$  integrin antagonists (such as Cilengitide) have been used to monitor and treat cancers successfully in clinical trials.<sup>48-</sup>

50

### ***Molecular imaging***

Nanoparticles can be modified with imaging probes for a variety of molecular imaging applications, such as optical imaging and positron emission tomography (PET). Optical imaging modalities have the advantage of higher temporal resolution and safer use (since they do not use ionizing radiation or radioactive materials), but they provide lower spatial resolution and sensitivity in deep tissues.<sup>49,56,71-79</sup> Some of the major limitations of optical imaging are related to the optical properties of tissues. A major limitation of optical imaging is the high scattering and absorption that occurs in biological tissues and the limited penetration of light *in vivo*.<sup>49,56,71-79</sup>

Since tissues and cells have numerous structures, boundaries and differences between each other, there are many different diffracting interfaces present. As a result, photons in the shorter wavelength visible range tend to be highly scattered, making it difficult to obtain depth resolved information from *in vivo* samples.<sup>49,56,71-79</sup> Some of these photons in the visible range (350–650 nm) are also absorbed, due to the presence of cytochromes and hemoglobin within cells and tissues (see Figure 1.4). Longer wavelength near infrared light (650-900 nm) tends to be absorbed and scattered less by tissues and cells, allowing light to penetrate deeper into tissue.<sup>49,56,71-79</sup> As a result, many fluorescent probes have been developed for use in near-infrared imaging. Despite this, probes in the higher range (closer to 900 nm) tend to have lower signal intensity and are less bright compared to ones on the lower end (closer to 650 nm), so probe wavelength has to be chosen carefully in order to provide optimal imaging. In addition, photostability of fluorophores is important for optimum image quality and consistency, and must be taken into account when choosing a fluorophore.

Near-infrared fluorescence (NIR) imaging is a particular kind of optical imaging that exploits the near-infrared range in the spectra to bypass the typical absorption and autofluorescence problems seen in optical imaging of biological tissues.<sup>49,56,71-79</sup> Lower autofluorescence allows for greater signal-to-background ratio. Typically, tissues exhibit a high photon absorbance in both the visible wavelength range (350–650 nm) and the infrared range (above 900 nm).<sup>49,56,71-79</sup> However, in the NIR range of 650–900 nm, the absorbance of water and tissues in the body is at a minimum and thus allows photons to penetrate tissue more efficiently and minimizes scattering.<sup>49,56,71-79</sup> Therefore, functional imaging of molecularly based events such as tumor-specific binding can be performed using optical imaging modalities in order to provide real time monitoring of biodistribution *in vivo*.<sup>49,56,71-79</sup> NIR imaging utilizes a



laser or bulb to excite a fluorophore at a specific wavelength, and the fluorophore then emits light at a different wavelength which then passes through a set of filters and is captured by a charge-coupled device (CCD) camera producing an image.<sup>49,56,71-79</sup> Although more recent advances have led to the development of tomographic (3D) optical imaging methods, planar (2D) optical imaging is more common.

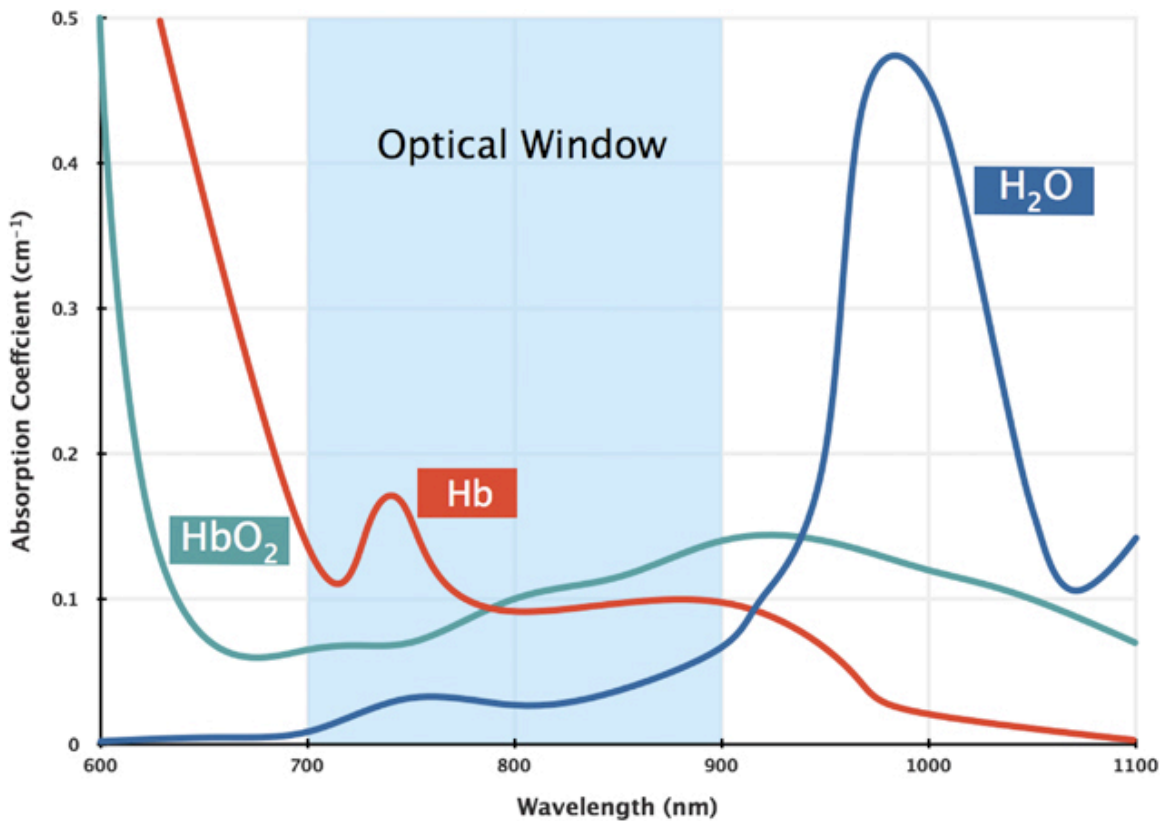


**Figure 1.4.** Absorption at near-infrared wavelengths by common biological molecules.<sup>74</sup>

While optical imaging is commonly used in small animals, applications in humans and larger subjects have been severely limited due to problems with light attenuation. Nuclear imaging techniques, like positron emission tomography (PET), offer a major advantage over optical techniques due to greater penetration of tissues with radioactive tracers compared to

optical tracers.<sup>94-97</sup> PET imaging provides superior sensitivity for imaging deeper tissues, but also presents challenges unique to radioactive tracers including development, half-life, and safety issues.<sup>94-97</sup> One of the main considerations with PET imaging would include selection of a radiotracer whose half-life is compatible with the kinetics of the nanoparticle drug delivery system *in vivo*. Radiotracers with shorter plasma half-lives than the nanoparticle drug delivery systems they are being used to image would present problems with image quality and consistency, as the radiotracer would undergo radioactive decay at a faster rate than the nanoparticles are cleared, producing lower signal intensity due to radioactive decay rather than nanoparticle clearance.

### ***Drug quantification***

Both NIR and PET imaging are non-invasive tools for visualizing tumor targeting *in vivo*, and a complement to more direct chemical quantification such as mass spectrometry. Measurement of radiance underestimates nanoparticle binding within the tumor because NIR light scatters throughout deeper tissues *in vivo*. Since the fluorescence intensity values are determined from intact tissue and not homogenized tissue, it is possible that the fluorescence intensity is not homogeneously distributed in the tissue and thus the values may vary in different segments of the same tissue. In contrast, HPLC-MS analysis of tumor drug content reflects concentration values determined directly from tissue homogenates.<sup>98-100</sup> While PET imaging can also be used along with scintigraphy of tissue homogenates to obtain radioactivity levels directly from tissues, this method requires careful handling and presents safety concerns due to radioactivity. HPLC-MS analysis circumvents limitations from both optical imaging by analyzing tissue homogenates, and those of PET imaging by providing a safer alternative to

radioactivity. In addition, HPLC-MS provides an analytical method for directly quantifying the actual drug or small molecule loaded within nanoparticle drug delivery systems, rather than indirect quantification via either an optical or radioactive imaging probe.<sup>98-100</sup> The use of HPLC-MS directly quantifies the content of chemotherapy drugs such as paclitaxel and camptothecin in tumors and other tissues.<sup>98-100</sup> Like other mass spectrometry methods, it is a highly sensitive tool for validating and complementing tumor targeting data provided by NIR optical imaging methods. Combining both optical imaging and mass spectrometry techniques enables confirmation of results using both imaging and chemical analysis of nanoparticle drug delivery systems targeted to tumors.

### ***Summary***

Development of nanoparticles for drug delivery and improved conjugating methods make it possible to design and create multifunctional nanoparticles for tumor-targeted drug delivery. Multifunctional nanoparticles composed of biodegradable polymers can be used to deliver controlled release of therapeutic drugs, functionalized with imaging agents for diagnostic purposes, and tumor-specific ligands for targeting of cancer. In this work, biodegradable polymeric ‘nanosponges’ were used to optimize targeted delivery of paclitaxel and camptothecin to lung cancer. Chapter 2 explores the optimization of linear polyester copolymers via tin (II) triflate catalyzed ring opening polymerization of lactone monomers. These low polydispersity polyesters are then used to produce optimized nanosponges. Chapter 3 shows the effect of paclitaxel or camptothecin loaded nanosponges in various schedules for the treatment of lung cancer cells *in vitro*. Chapter 4 discusses the synthesis of a cyclic RGD peptide targeted nanosponge for targeting and imaging in lung cancer cells. Chapter 5 explores the feasibility of

HVGGSSV peptide targeted nanosponges for targeting, imaging and treatment of lung cancer in an *in vivo* mouse model. Chapter 6 examines future directions and final conclusions from these works.

## References

1. Chabner B.A., Roberts T.G. Chemotherapy and the war on cancer. *Nat. Rev. Cancer* 2005, 5, 65-72.
2. Wang A.Z., Langer R., Farokhzad O.C. Nanoparticle Delivery of Cancer Drugs. *Annu. Rev. Med.* 2012, 63, 185-98.
3. Wagner V., Dullaart A., Bock A.K., Zweck A. The emerging nanomedicine landscape. *Nat. Biotechnol* 2006, 24, 1211-1217.
4. Jain R.K., Stylianopoulos T. Delivering nanomedicine to solid tumors. *Nat. Rev. Clin. Oncol.* 2010, 7, 653-664.
5. Caruthers S.D., Wickline S.A., Lanza G.M. Nanotechnological applications in medicine. *Curr. Opinion in Biotech.* 2007, 18, 26–30.
6. Steichen S.D., Caldorera-Moore M., Peppas N.A. A review of current nanoparticle and targeting moieties for the delivery of cancer therapeutics. *Eur. J. of Pharm. Sci.* 2012, 1-11.
7. Farokhzad O.C., Langer R. Impact of nanotechnology on drug delivery. *ACS Nano* 2009, 3, 16–20.
8. Ferrari M. Cancer nanotechnology: opportunities and challenges. *Nat. Rev. Cancer* 2005, 5, 161–171.
9. Langer R. Drug delivery and targeting. *Nature* 1998, 392, 5–10.
10. Chan J.M., Zhang L.F., Yuet K.P., Liao G., Rhee J.W., Langer R., Farokhzad O.C. PLGA-lecithin-PEG core-shell nanoparticles for controlled drug delivery. *Biomaterials* 2009, 30(8), 1627-34.
11. Feng S.S., Zhao L.Y., Zhang Z.P., Bhakta G., Win K.Y., Dong Y.C., Chien S. Chemotherapeutic engineering: Vitamin E TPGS-emulsified nanoparticles of biodegradable polymers realized sustainable paclitaxel chemotherapy for 168 h in vivo. *Chem. Eng. Science* 2007, 62(23), 6641-48.
12. Heidel J.D. and Davis M.E. Clinical developments in nanotechnology for cancer therapy. *Pharm. Res.* 2011, 28, 187–199.
13. Sokolsky-Papkov M., Agashi K., Olaye A., Shakesheff K., and Domb A.J. Polymer carriers for drug delivery and tissue engineering. *Adv. Drug Deliv. Rev.* 2007, 59, 187 – 206.

14. Nair L.S. and Laurencin C.T. Biodegradable polymers as biomaterials. *Prog. Polym. Sci.* 2007, 32, 762 – 98.
15. Cho K., Wang X., Nie S., Chen Z., Shin D.M. Therapeutic nanoparticles for drug delivery in cancer. *Clin. Cancer Res.* 2008, 14(5), 1310-1316.
16. Duncan R. The dawning era of polymer therapeutics. *Nat. Rev. Drug Discov.* 2003, 2, 347-60.
17. Peer D., Karp J.M., Hong S., Farokhzad O.C., Margalit R., Langer R. Nanocarriers as an emerging platform for cancer therapy. *Nat. Nanotechnol.* 2007, 2, 751-760.
18. Davis M.E., Chen Z., Shin D.M. Nanoparticle therapeutics: an emerging treatment modality for cancer. *Nat. Rev. Drug Discovery* 2008, 7, 771-782.
19. Yallapu M.M., Jaggi M., Chauhan S. Design and engineering of nanogels for cancer treatment. *Drug Discov Today* 2011, 16(9), 457–463.
20. Zhang Z., Huey L.S., Feng S.S. Folate-decorated poly(lactide-co-glycolide)-vitamin E TPGS nanoparticles for targeted drug delivery. *Biomaterials* 2007, 28(10), 1889-1899.
21. Moya-Ortega M.D., Alvarez-Lorenzo C., Concheiro A., Loftsson T. Cyclodextrin-based nanogels for pharmaceutical and biomedical applications. *International Journal of Pharmaceutics* 2012, 428, 152-163.
22. Kabanov A.V., Vinogradov S.V. Nanogels as Pharmaceutical Carriers: Finite Networks of Infinite Capabilities. *Angew. Chem. Int. Ed. Engl.* 2009, 48(30), 5418–5429.
23. Raemdonck K., Demeester J., De Smedt S. Advanced nanogel engineering for drug delivery. *Soft Matter* 2009, 5, 707–715.
24. Chacko R.T., Ventura J., Zhuang J., Thayumanavan S. Polymer nanogels: A versatile nanoscopic drug delivery platform. *Advanced Drug Delivery Reviews* 2012, 64, 836–851.
25. Li N., Wang J., Yang X., Li L. Novel nanogels as drug delivery systems for poorly soluble anticancer drugs. *Colloids and Surfaces B: Biointerfaces* 2011, 83, 237–244.
26. Oh J.K., Drumright R., Siegwart D.J., Matyjaszewski K. The development of microgels/nanogels for drug delivery applications. *Prog. Polym. Sci.* 2008, 33, 448–477.
27. Peer D., Karp J.M., Hong S., Farokhzad O.C., Margalit R., Langer R. Nanocarriers as an emerging platform for cancer therapy. *Nat. Nanotechnol.* 2007, 2, 751-760.
28. Murphy E.A., Majeti B.K., Mukthavaram R., Acevedo L.M., Barnes L.A., Cheresch D.A. Targeted nanogels: A versatile platform for drug delivery to tumors. *Mol. Cancer Ther.* 2011, 10(6), 972-982.

29. Maeda H., Wua J., Sawaa T., Matsumurab Y., Horic K. Tumor vascular permeability and the EPR effect in macromolecular therapeutics: a review. *J. Control Release* 2000, 65, 271–284.
30. Prabhakar U., Maeda H., Jain R.K., Sevick-Muraca E.M., Zamboni W., Farokhzad O.C., Barry S.T., Gabizon A., Grodzinski P., Blakey D.C. Challenges and key considerations of the enhanced permeability and retention effect for nanomedicine drug delivery in oncology. *Cancer Res* 2013, 73(8), 2412-2417.
31. Maeda H., Nakamura H., Fang J. The EPR effect for macromolecular drug delivery to solid tumors: improved tumor uptake, less systemic toxicity, and improved tumor imaging. *Adv Drug Deliver Rev* 2013, 65, 71-79.
32. Maeda H. Macromolecular therapeutics in cancer treatment: the EPR effect and beyond. *J. Control Release* 2012, 164, 138-44.
33. Folkman J. Angiogenesis in cancer, vascular, rheumatoid and other disease. *Nat. Med.* 1995, 1, 27-31.
34. Maeda H. The enhanced permeability and retention (EPR) effect in tumor vasculature: the key role of tumor-selective macromolecular drug targeting. *Adv. Enzyme Regul.* 2001, 41, 189-207.
35. Yu D., Lu Q., Xie J., Fang C., Chen H. Peptide-conjugated biodegradable nanoparticles as a carrier to target paclitaxel to tumor neovasculature. *Biomaterials* 2010, 31, 2278–2292.
36. Farokhzad O.C., Cheng J., Teply B.A., Sherifi I., Jon S., Kantoff P.W., Richie J.P., Langer R. Targeted nanoparticle-aptamer bioconjugates for cancer chemotherapy in vivo. *Proc. Natl. Acad. Sci.* 2006, 103(16), 6315–6320.
37. Cho K., Wang X., Nie S., Chen Z., Shin D.M. Therapeutic nanoparticles for drug delivery in cancer. *Clin. Cancer Res.* 2008, 14(5), 1310-1316.
38. Ross J.S., Schenkein D.P., Pietrusko R., et al. Targeted therapies for cancer. *Am. J. Clin. Pathol.* 2004, 122, 598-609.
39. Allen T.M. Ligand-targeted therapeutics in anticancer therapy. *Nat. Rev. Cancer* 2002, 2, 750-63.
40. Torchilin V.P. Targeted pharmaceutical nanocarriers for cancer therapy and imaging. *The AAPS Journal* 2007, 9(2), E128-E147.

41. Egusquiaguirre S.P., Igartua M., Hernández R.M., Pedraz J.L. Nanoparticle delivery systems for cancer therapy: advances in clinical and preclinical research. *Clin. Transl. Oncol.* 2012, 14, 83-93.
42. Wang A.Z., Langer R., Farokhzad O.C. Nanoparticle delivery of cancer drugs. *Annu. Rev. Med.* 2012, 63, 185-98.
43. Heidel J.D., Davis M.E. Clinical Developments in Nanotechnology for Cancer Therapy. *Pharm. Res.* 2011, 28, 187–199.
44. Wagner V., Dullaart A., Bock A.K., Zweck A. The emerging nanomedicine landscape. *Nat. Biotech.* 2006, 24, 1211-1217.
45. Jain R.K., Stylianopoulos T. Delivering nanomedicine to solid tumors. *Nat. Rev. Clin. Oncol.* 2010, 7, 653-664.
46. Caruthers S.D., Wickline S.A., Lanza G.M. Nanotechnological applications in medicine. *Curr. Opinion Biotech.* 2007, 18, 26–30.
47. Steichen S.D., Caldorera-Moore M., Peppas N.A. A review of current nanoparticle and targeting moieties for the delivery of cancer therapeutics. *Eur. J. Pharm. Sci.* 2012, 1-11.
48. Byrne J.D., Betancourt T., Brannon-Peppas L. Active targeting schemes for nanoparticle systems in cancer therapeutics. *Adv. Drug Deliv. Reviews* 2008, 60, 1615–1626.
49. Cheng Z., Wu Y., Xiong Z., Gambhir S., Chen X. Near-infrared fluorescent RGD peptides for optical imaging of integrin  $\alpha_v\beta_3$  expression in living mice. *Bioconjugate Chem.* 2005, 16, 1433-1441.
50. Pasqualini R., Koivunen E., Ruoslahti E. Alpha v integrins as receptors for tumor targeting by circulating ligands. *Nat. Biotech.* 1997, 15, 542-546.
51. Farokhzad O.C., Langer R. Impact of nanotechnology on drug delivery. *ACS Nano* 2009, 3, 16–20.
52. Ferrari M. Cancer nanotechnology: opportunities and challenges. *Nat. Rev. Cancer* 2005, 5, 161–171.
53. Langer R. Drug delivery and targeting. *Nature* 1998, 392, 5–10.
54. Langer R., Folkman J. Polymers for the sustained release of proteins and other macromolecules. *Nature* 1976, 263, 797–800.
55. Bartlett D.W., Su H., Hildebrandt I.J., Weber W.A., Davis M.E. Impact of tumor-specific targeting on the biodistribution and efficacy of siRNA nanoparticles measured by multimodality in vivo imaging. *Proc. Natl. Acad. Sci.* 2007, 104(39), 15549–15554.



56. Yu M.K., Park J., Jon S. Targeting Strategies for Multifunctional Nanoparticles in Cancer Imaging and Therapy. *Theranostics* 2012, 2(1), 3-44.
57. Yu D., Lu Q., Xie J., Fang C., Chen H. Peptide-conjugated biodegradable nanoparticles as a carrier to target paclitaxel to tumor neovasculature. *Biomaterials* 2010, 31, 2278–2292.
58. Sergeeva A., Kolonin M.G., Molldrem J.J. Pasqualini R., Arap W. Display technologies: Application for the discovery of drug and gene delivery agents. *Adv. Drug Delivery Rev.* 2006, 58, 1622–1654.
59. Bábíčková J., Tóthová L., Boor P., Celec P. In vivo phage display - A discovery tool in molecular biomedicine. *Biotech. Adv.* 2013, 31, 1247–1259.
60. Nilsson F., Tarli L., Viti F., Neri D. The use of phage display for the development of tumour targeting agents. *Adv. Drug Delivery Reviews* 2000, 43, 165-196.
61. Rafii S., AVECILLA S.T., Jin D.K. Tumor vasculature address book: Identification of stage-specific tumor vessel zip codes by phage display. *Cancer Cell* 2003, 331-333.
62. Ruoslahti E. Specialization of tumour vasculature. *Nat. Rev. Cancer* 2002, 2, 83-90.
63. Senter P.D. Potent antibody drug conjugates for cancer therapy. *Curr. Opinion in Chem. Biol.* 2009, 13, 235–244.
64. Alley S.C., Okeley N.M. Senter P.D. Antibody–drug conjugates: targeted drug delivery for cancer. *Curr. Opinion in Chem. Biol.* 2010, 14, 529-537.
65. Egusquiaguirre S.P., Igartua M., Hernández R.M., Pedraz J.L. Nanoparticle delivery systems for cancer therapy: advances in clinical and preclinical research. *Clin. Transl. Oncol.* 2012, 14, 83-93.
66. Yallapu M.M., Jaggi M., Chauhan S. Design and engineering of nanogels for cancer treatment. *Drug Discov Today* 2011, 16(9), 457–463.
67. Zhang Z., Huey L.S., Feng S.S. Folate-decorated poly(lactide-co-glycolide)-vitamin E TPGS nanoparticles for targeted drug delivery. *Biomaterials* 2007, 28(10), 1889-1899.
68. Zhuang J., Jiwanich S., Deepak V.D., Thayumanavan S. Facile preparation of nanogels using activated ester containing polymers. *ACS Macro Lett.* 2012, 1, 175–179.
69. Silvers A.L., Chang C., Emrick T. Functional aliphatic polyesters and nanoparticles prepared by organocatalysis and orthogonal grafting chemistry. *J. Polymer Science Part A: Polymer Chemistry*, 2012, 1-13.

70. Jérôme C., Lecomte P. Recent advances in the synthesis of aliphatic polyesters by ring-opening polymerization. *Adv Drug Delivery Rev* 2008, 60, 1056-1076.
71. Becker, A. et al. Receptor-targeted optical imaging of tumors with near-infrared fluorescent ligands. *Nat. Biotechnol.* 2001, 19, 327–331.
72. Weissleder R. and Ntziachristos V. Shedding light onto live molecular targets. *Nat. Med.* 2003, 9(1), 123-28.
73. Tung C.H., Lin Y., Moon W. and Weissleder R. Receptor-targeted near-infrared fluorescence probe for in vivo tumor detection. *Chem. Bio. Chem.* 2002, 3, 784–786.
74. Phan T.G., Bullen A. Practical intravital two-photon microscopy for immunological research: faster, brighter, deeper. *Immunology and Cell Biology* 2010, 88, 438-444.
75. Smith R.A., Guleryuz S., Manning H.C. Molecular imaging metrics to evaluate response to preclinical therapeutic regimens. *Front. Biosci.* 2011, 16, 393–410.
76. Zhang X., Bloch S., Akers W., Achilefu S. Near-infrared molecular probes for in vivo imaging. *Curr. Protoc. Cytom.* 2012, 1-28.
77. Luo S., Zhang E., Su Y., Cheng T., Shi C. A review of NIR dyes in cancer targeting and imaging. *Biomaterials* 2011, 32, 7127-7138.
78. Weissleder R., Ntziachristos V. Shedding light onto live molecular targets. *Nat. Medicine* 2003, 9(1), 123-128.
79. Bremer C., Ntziachristos V., Weissleder R. Optical-based molecular imaging: contrast agents and potential medical applications. *Eur. Radiol.* 2003, 13, 231-243.
80. Heath F., Haria P., Alexander C. Varying Polymer Architecture to Deliver Drugs. *The AAPS Journal* 2007, 9(2), E235-E240.
81. Qiu L.Y., Bae Y.H. Polymer architecture and drug delivery. *Pharm. Res.* 2006, 23(1), 1-30.
82. Su W., Cheng F., Shieh D., Yeh C., Su W. PLGA nanoparticles codeliver paclitaxel and Stat3 siRNA to overcome cellular resistance in lung cancer cells. *Int. J. Nanomedicine* 2012, 7, 4269-4283.
83. Danhier F., Ansorena E., Silva J.M., Coco R., Le Breton A., Préat V. PLGA-based nanoparticles: An overview of biomedical applications. *J. Control Release* 2012, 161, 505–522.
84. Win K.Y., Feng S.S. In vitro and in vivo studies on vitamin E TPGS emulsified poly (D, L-lactic-co-glycolic acid) nanoparticles for paclitaxel formulation. *Biomaterials* 2006,

27(10), 2285-2291.

85. Zhang Z., Feng S. Nanoparticles of poly(lactide)/vitamin E TPGS copolymer for cancer chemotherapy: Synthesis, formulation, characterization and in vitro drug release. *Biomaterials* 2006, 27, 262–270.
86. van der Ende A.E., Kravitz E.J. and E. Harth. Approach to formation of multifunctional polyester particles in controlled nanoscopic dimensions. *J. Am. Chem. Soc.* 2008, 130, 8706–8713.
87. van der Ende A.E., Sathiyakumar V., Diaz R., Hallahan D.E. and E. Harth. Linear release nanoparticle devices for advanced targeted cancer therapies with increased efficacy. *Polym. Chem.* 2010, 1, 93–96.
88. van der Ende A.E., Croce T., Hamilton S., Sathiyakumar V. and E. Harth. Tailored polyester nanoparticles: post-modification with dendritic transporter and targeting units via reductive amination and thiol-ene chemistry. *Soft Matter* 2009, 5, 1417–1425.
89. Passarella R.J., Spratt D.E., van der Ende A.E., et al. Targeted nanoparticles that deliver a sustained, specific release of paclitaxel to irradiated tumors. *Cancer Res.* 2010, 70, 4550-4559.
90. Wang H., Fu A., Han Z. and Hallahan D. Tax interacting protein (TIP-1): A potential radiation inducible receptor within cancer. *Int. J. Radiat. Oncol.* 2007, 69, S590-S591.
91. Hallahan D.E., Geng L., Cmelak A.J. et al. Targeting drug delivery to radiation-induced neoantigens in tumor microvasculature. *J. Control Release.* 2001, 74, 183-191.
92. Hariri G., Yan H.P., Wang H.L., Han Z.Z., and Hallahan D.E. Radiation-guided drug delivery to mouse models of lung cancer. *Clin. Cancer Res.* 2010, 16, 4968-4977.
93. Wang H.L., Yan H.P., Fu A., Han M.J., Hallahan D., Han Z.Z. TIP-1 translocation onto the cell plasma membrane is a molecular biomarker of tumor response to ionizing radiation. *PLoS One* 2010, 5.
94. Rudin M. and Weissleder R. Molecular imaging in drug discovery and development. *Nat. Rev. Drug Disc.* 2003, 2, 123-131.
95. Culver J., Akers W., Achilefu S. Multimodality molecular imaging with combined optical and SPECT/PET modalities. *J. Nucl. Med.* 2008, 49, 169-172.
96. Gambhir S.S. Molecular imaging of cancer with positron emission tomography. *Nat. Rev. Cancer.* 2002, 2, 683-693.
97. Peterson T.E. and Manning H.C. Molecular imaging: <sup>18</sup>F-FDG and a whole lot more. *J. Nucl. Med. Technol.* 2009, 37, 151-161.

98. Chipman S.D., Oldham F.B., Pezzoni G. and Singer J.W. Biological and clinical characterization of paclitaxel polyglumex (PPX, CT-2103), a macromolecular polymer-drug conjugate. *Int. J. Nanomedicine*. 2006, 1(4), 375-383.
99. Hou L., Yao J., Zhou J. Simultaneous LC-MS analysis of paclitaxel and retinoic acid in plasma and tissues from tumor-bearing mice. *Chromatographia*. 2011, 73, 471-480.
100. Khan S., Ahmad A., Guo W., Wang Y.F., Abu-Qare A., Ahmad I. A simple and sensitive LC/MS/MS assay for 7-ethyl-10-hydroxycamptothecin (SN-38) in mouse plasma and tissues: application to pharmacokinetic study of liposome entrapped SN-38 (LE-SN38). *J. Pharm. Biomed. Anal.* 2005, 37(1), 135-142.

## CHAPTER 2

### SYNTHESIS OF SECOND GENERATION POLYESTER ‘NANOSPONGES’ VIA RING-OPENING POLYMERIZATION WITH TIN (II) TRIFLATE CATALYST

#### ***Abstract***

Nanoparticles made from biomedical polymers are commonly used in drug delivery applications because they allow delivery of drugs with degradation of nanocarriers over time. These polymers typically come from a class of aliphatic polyesters that are produced via ring-opening polymerization of lactone monomers. While a large number of catalysts and initiators have been previously investigated in the literature for polymerization of lactones, the most common catalyst used for these applications is tin (II) octanoate. In order to produce a polymer with the desired reaction conditions and characteristics, catalyst selection plays a significant role. The aim of this study was to investigate tin (II) triflate as a catalyst for the ring-opening polymerization (ROP) of poly(VL-*co*-AVL) and poly(VL-*co*-AVL-*co*-OPD) copolymers. Both copolymers were prepared using tin (II) triflate and ethyl alcohol initiator, and results showed improved yields and monomer incorporation for both polymers, with narrower PDIs for poly(VL-*co*-AVL) copolymers compared to poly(VL-*co*-AVL-*co*-OPD) copolymers. Lower polydispersity in linear polymer precursors can translate into greater control and uniformity of resulting nanoparticle size distribution. This can in turn allow for more uniform drug release, making it easier to predict and control drug release profiles for nanoparticles both *in vitro* and *in vivo*.

## ***Introduction***

### *Polymers for drug delivery*

Biomedical polymers typically used in drug delivery applications have mostly come from a class of aliphatic polyesters widely known for their superior biocompatible and biodegradable properties.<sup>7-9,52,53</sup> Utilizing biodegradable materials has advantages for drug delivery applications because it allows delivery of drugs with degradation of the nanocarrier over time. Ideally, this material should degrade at a rate that is compatible with its purpose, and its degradation products should be non-toxic and physiologically compatible.<sup>7-9,52,53</sup> In addition, these materials should have mechanical properties (crystallinity, morphology, etc.) that are suitable for their intended applications. Polyesters are hydrolytically degraded, with ester bonds being broken over time at rates that can be controlled depending on the length of the polymer chains.<sup>4-6,10,12,14,51</sup> Aliphatic polyesters have been used as scaffolds for drug delivery systems with sustained release of drugs and other small molecules, as sutures and adhesives, and in tissue engineering applications.<sup>7-9,52,53</sup> Examples of some commonly used polyesters include homopolymers and copolymers of poly(lactic acid) (PLA), poly(glycolic acid) (PGA), poly(caprolactone) (PCL), poly(valerolactone) (PVL) and poly(butyrolactone) (PBL), among others (Figure 2.1).<sup>7-9,52,53</sup> The resulting polymers are composed of lactide and lactone monomer repeat units bearing different functional groups, and are suitable for a variety of applications. By changing the type and ratio of monomers used, the composition of these polymers can be controlled and different chemical and mechanical properties can be produced for specific applications. Polymerizations of these monomers are also similar, allowing for many different combinations of copolymers to be produced. Consequently, aliphatic polyesters have been widely used to produce nanoparticles for drug delivery applications.

### *Ring-opening polymerization*

Ring-opening polymerization of lactone monomers are important in the development of aliphatic polyesters for drug delivery applications. This polymerization method offers the potential for preparing homopolymers and copolymers with defined molecular weight, chain length, and architecture. These polymers exhibit varying architectures from block and random linear copolymers to branched and dendritic structures. Various functional groups pendant on polymer backbones can be used to customize the physical and chemical properties of these polymers, such as their hydrophilicity and rate of degradation, as well as providing options for further chemical modification. Polymerization with allyl valerolactone (AVL) monomer provides the possibility of partial epoxidation of these allyl groups for nanoparticle formation using amine/epoxide chemistry. Polymerization with 2-oxepane-1, 5-dione (OPD) monomer provides additional polar oxygens for increased hydrophilicity of resulting polymers. The sequence of monomers in a linear polymer chain is also of consideration, as preparation of a copolymer with random monomer distribution (ABABBA) instead of block (AAABBB) provides additional amorphousness and decreases the crystallinity of the copolymer, increasing hydrophilicity and rate of degradation.

### *Material properties*

The hydrolytic degradation rate of a polymer depends primarily on its hydrophobicity and crystallinity, as these factors determine how well water molecules can penetrate the polymer.<sup>6-10</sup> Greater hydrophobicity reduces interaction with water molecules and slows down degradation. In general, polymers with higher crystallinity degrade slower than polymers with lower crystallinity, and polymers with more amorphous regions degrade faster than those with fewer

amorphous regions. One way to introduce more amorphous regions into a polymer is to use more than one monomer, and thus produce a copolymer. The presence of any sterically hindering functional groups at scission sites (where ester bonds are cleaved) also decreases the rate of degradation.

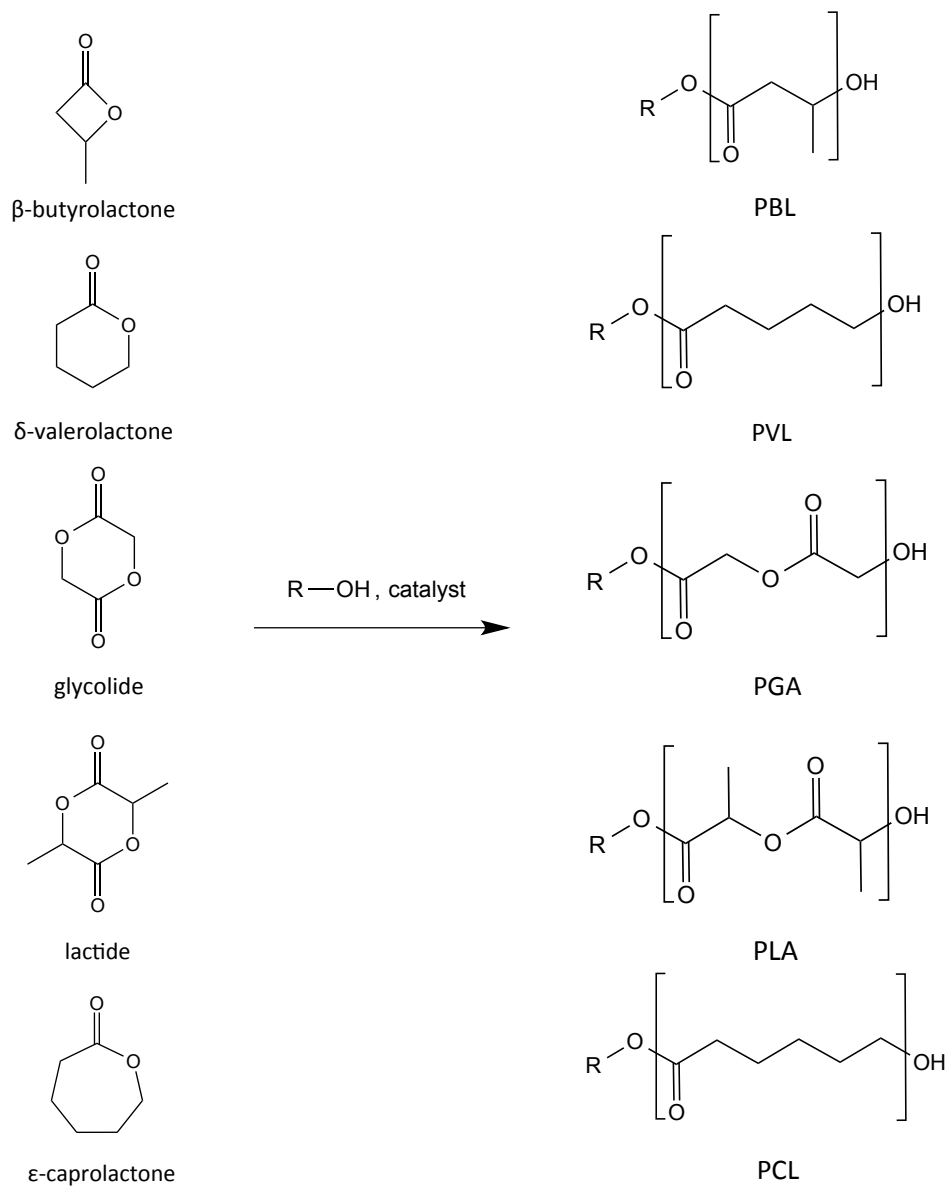


**Figure 2.1.** Commonly used cyclic ester monomers for ring-opening polymerization of polyesters.



### *Catalyst optimization*

A large number of catalysts and initiators have been previously investigated in the literature for polymerization of lactones.<sup>10,12,17,18,51</sup> In order to produce a polymer with the desired reaction conditions and characteristics, catalyst selection plays a significant role. The aim of this study was to investigate tin (II) trifluoromethanesulfonate (tin triflate or Sn(OTf)<sub>2</sub>) as a catalyst for the ring-opening polymerization (ROP) of poly(VL-*co*-AVL) and poly(VL-*co*-AVL-*co*-OPD) copolymers.

Tin (II) bis-(2-ethylhexanoate), also known as tin octanoate or Sn(Oct)<sub>2</sub>, has been the most extensively used metal catalyst for preparation of polymers using ROP methods.<sup>15,16</sup> Because it exhibits lower sensitivity towards water, it is easier to use in the preparation of polymers industrially. It also has received approval by the Food and Drug Administration (FDA) for the formulation of polymer coatings used in many food packaging materials.<sup>4-6,15,16</sup> However, high reaction temperatures (above 100 °C) are needed for its use in typical ROP methods, and resulting intermolecular and intramolecular esterification tend to produce polymers with wide polydispersities.<sup>10,12,17,18,51</sup> This can be problematic if polymers of uniform chain length are required, such as in the preparation of polymer-based nanoparticles.

The mechanism of initiation in tin triflate catalyzed polymerization of lactones is shown in Figure 2.2.<sup>10-13,17,18,51</sup> An initiating species (tin triflate initiator) is formed, followed by coordination-insertion of the monomer into the alkoxide bond produced, and then chain transfer of the active polymerizing center to remaining unreacted alcohol.<sup>10-13,17,18,51</sup> The coordination-insertion reaction with the lactone monomer creates the first actively propagating linear polymer chain end. This chain end is composed from the initiating alcohol and the active propagating center (from the first monomer unit and tin alkoxide).<sup>10-13,17,18,51</sup>



## ***Experimental***

### *Materials and Methods*

*Reagents.* Chemical reagents were purchased from Sigma-Aldrich and Strem Chemicals, and used as received unless otherwise stated.

*NMR Spectroscopy.* All  $^1\text{H}$  NMR spectra were acquired using a 400 MHz Bruker AV-400 NMR with deuterated chloroform ( $\text{CDCl}_3$ ) and tetramethylsilane as internal standard.

*Purification.* Biotage Isolera Spektra One flash purification system equipped with a UV  $\lambda$  absorbance detector (254 nm) was used to purify AVL monomers. Purification was performed using a SNAP HP 50 g silica column with a 5-20% ethyl acetate gradient in n-hexanes with a flow rate of 50 ml/min. All monomers (AVL and VL) were vacuum distilled using a Kugelrohr distillation apparatus (Sigma Aldrich).

*Gel-permeation chromatography (GPC).* All GPC was performed using a Waters chromatography system equipped with refractive index and dual  $\lambda$  absorbance detectors, four 5 mm Waters columns (300 mm x 7.7 mm) with pore size (100, 1000, 100,000 and 1,000,000 Å respectively). All samples were dissolved in tetrahydrofuran (THF) or dimethylformamide (DMF), with a 20  $\mu\text{l}$  injection volume and 1 mL/min flow rate.

*Transmission electron microscopy (TEM).* TEM imaging was performed on nanoparticles by dissolving approximately 5 mg in a solution of 1 : 0.4 mL isopropanol/acetonitrile. The dissolved nanoparticles were sonicated for 5 minutes and stained with 4 drops of a 3% phosphotungstic acid/water solution for 10 minutes. This solution was sonicated once more for 5 minutes before the copper grids were prepared. Ultrathin Carbon Type-A 400 mesh copper grids (Ted Pella, Redding, CA) were gently immersed into the stained nanoparticle solution and allowed to dry for 2 hrs prior to analysis. A 200 kV Philips CM20T transmission electron microscope was used to

acquire micrographs of the nanoparticles.

#### *δ-valerolactone monomer (VL)*

Technical grade  $\delta$ -valerolactone was Kugelrohr distilled to produce a colorless liquid product.

#### *Synthesis of allyl-substituted valerolactone monomer (AVL)*

A flame dried 500 mL two-necked round bottom flask was equipped with a stir bar, sealed with a rubber septum, and purged with nitrogen for 30 min. To the flask, 156.25 mL of anhydrous THF was added and cooled to  $-78\text{ }^{\circ}\text{C}$  in a dry ice/acetone bath. Following this, a basic solution of lithium diisopropylamine was produced by adding redistilled *n,n*-diisopropylamine (3.3 mL, 23.63 mmol) and *n*-butyl lithium (2.5 M in hexanes) (9.35 mL, 23.38 mmol) dropwise via syringe. This solution was stirred for 20 minutes. A nitrogen purged solution of distilled  $\delta$ -valerolactone **1** (1.97 mL, 21.23 mmol) in anhydrous THF (56 mL) was then added dropwise via syringe over 30 min. After an additional 30 min of stirring, a nitrogen purged solution of allyl bromide (2.21 mL, 25.54 mmol) in hexamethylphosphoramide (4.43 mL, 25.46 mmol) was added via syringe. The reaction mixture was warmed up to  $-40\text{ }^{\circ}\text{C}$  and stirred for 2 hrs. The reaction was quenched with excess  $\text{NH}_4\text{Cl}$  solution. The crude product was concentrated via rotary evaporator, washed three times with saturated NaCl solution, and dried with anhydrous  $\text{MgSO}_4$ . The crude product was purified via column chromatography (Biotage Isolera), analyzed by thin layer chromatography and Kugelrohr distilled. Chromatography with a gradient of 5-20% ethyl acetate in *n*-hexanes as eluent gave a yellow liquid product. Kugelrohr distillation produced a colorless liquid product. Yield: 3.56 g (89%).  $^1\text{H}$  NMR (400MHz,  $\text{CDCl}_3/\text{TMS}$ , ppm)  $\delta$ : 5.82 (m, 1H,  $\text{H}_2\text{C}=\text{CH}-$ ), 5.11 (m, 2H,  $\text{H}_2\text{C}=\text{CH}-$ ), 4.32 (m, 2H,  $-\text{C}(\text{O})\text{OCH}_2-$ ), 2.60 (m, 2H,  $\text{H}_2\text{C}=\text{CHCH}_2-$ ), 2.34 (m, 1H,  $\text{H}_2\text{C}=\text{CHCH}_2\text{CH}-$ ), 2.08 (m, 1H,  $\text{H}_2\text{C}=\text{CHCH}_2\text{CHCH}_2-$ ), 1.92 (m, 2H,  $\text{C}(\text{O})\text{OCH}_2\text{CH}_2-$ ), 1.57 (m, 1H,  $\text{H}_2\text{C}=\text{CHCH}_2\text{CHCH}_2-$ ).

### *Synthesis of 2-oxepane-1,5-dione monomer (OPD)*

To a 200 mL round bottom flask, equipped with stir bar, 1,4-cyclohexanedione (4.0 g, 35.84 mmol) and 3-chloroperoxybenzoic acid (4.5 g, 55.35 mmol) was added. Reagents were dissolved in dichloromethane (44 mL) and the reaction mixture was stirred and refluxed for 6 h at 44 °C in an oil bath. The reaction mixture was cooled to room temperature and solvent was removed via rotary evaporation. The crude product was washed five times with cold diethyl ether and dried under vacuum for 72 hrs. Isolated yield: 2.1g. <sup>1</sup>H NMR (400 MHz, CDCl<sub>3</sub>/TMS, ppm)  $\delta$ : 4.41 (t, J = 5.2 Hz, 2H, -C(O)OCH<sub>2</sub>CH<sub>2</sub>C(O)-), 2.81 (m, 4H, -CH<sub>2</sub>C(O)CH<sub>2</sub>-), 2.74 (m, 2H, -CH<sub>2</sub>C(O)O-), 2.69 (m, 2H, -CH<sub>2</sub>C(O)-).

### *Copolymerization of $\alpha$ -allyl- $\delta$ -valerolactone (AVL) 2 and $\delta$ -valerolactone (VL) 1.*

A flame dried 25 mL 3-necked round bottom flask was equipped with a stir bar, sealed with rubber septa and nitrogen purged. A stock solution of anhydrous ethanol in anhydrous tetrahydrofuran was prepared (1.7 M) in a 50 mL flame dried and nitrogen purged round bottom flask, and a stock solution of Sn(OTf)<sub>2</sub> catalyst in anhydrous tetrahydrofuran was prepared (3.7x10<sup>-2</sup> M) in a 10 mL flame dried and nitrogen purged round bottom flask. Ethanol (584  $\mu$ L, 1.0 mmol) and Sn(OTf)<sub>2</sub> (261  $\mu$ L, 9.64 x 10<sup>-6</sup> mol) were added via syringe to the 25 mL 3-neck round bottom flask and the catalyst/initiator solution was allowed to stir at room temperature for 30 minutes prior to simultaneous addition of  $\delta$ -valerolactone (2.22 g, 22.0 mmol) and  $\alpha$ -allyl(valerolactone) (0.777 g, 5.548 mmol) monomers via syringe. After addition of both monomers, the reaction was stirred for 24 h at room temperature. The resulting polymer was diluted with 1 mL anhydrous THF and purified by dropwise addition into 1 L of chilled methanol to remove any remaining monomer and catalyst. The methanol was decanted and the precipitate

redissolved in methylene chloride, rotary evaporated and dried *in vacuo*. The resulting polymer was observed as a waxy white solid.  $M_w = 3000$  Da;  $^1\text{H NMR}$  (400 MHz,  $\text{CDCl}_3/\text{TMS}$ , ppm)  $\delta$ : 5.72 (m,  $\text{H}_2\text{C}=\text{CH}-$ ), 5.04 (m,  $\text{H}_2\text{C}=\text{CH}-$ ), 4.08 (m,  $-\text{CH}_2-\text{O}-$ ), 3.64 (m,  $\text{CH}_3\text{CH}_2\text{O}-$ ), 2.34 (m, vl,  $-\text{CH}_2\text{CH}_2\text{C}(\text{O})\text{O}-$ , avl,  $\text{H}_2\text{C}=\text{CHCH}_2\text{CH}-$ ,  $\text{H}_2\text{C}=\text{CHCH}_2\text{CH}-$ ), 1.68 (m, avl and vl,  $-\text{CHCH}_2\text{CH}_2-$ ), 1.26 (t,  $\text{CH}_3\text{CH}_2\text{O}-$ ).

#### *Partial epoxidation of poly(VL-co-AVL) 5*

In a 100 mL round bottom flask, equipped with stir bar and rubber septum, a solution of poly(VL-co-AVL) (1.0 g,  $1.55 \times 10^{-3}$  mol) was dissolved in 8.5 mL of methylene chloride. To this solution, meta-chloroperoxybenzoic acid (121.25 mg,  $7.03 \times 10^{-4}$  mol) was added. The solution was stirred for 24 hrs at room temperature and then concentrated via rotary evaporator. The crude product was dissolved in a minimal amount of dichloromethane (2 mL) and precipitated into an Erlenmeyer flask containing 500 mL cold diethyl ether. The solution was decanted, and the white solid was rotary evaporated and dried *in vacuo* to obtain the final white waxy polymer. Yield: 0.768 g (76.8%).  $^1\text{H NMR}$  (400 MHz,  $\text{CDCl}_3/\text{TMS}$ , ppm)  $\delta$ : Decrease in allylic protons at 5.7 and 5.09 ppm and the appearance of small broad resonance peaks at 2.96, 2.75 and 2.47 ppm due to the formation of the epoxide. Same method used for partial epoxidation of poly(VL-co-AVL-co-OPD) copolymer (6).

#### *Formation of nanoparticles using intermolecular crosslinking*

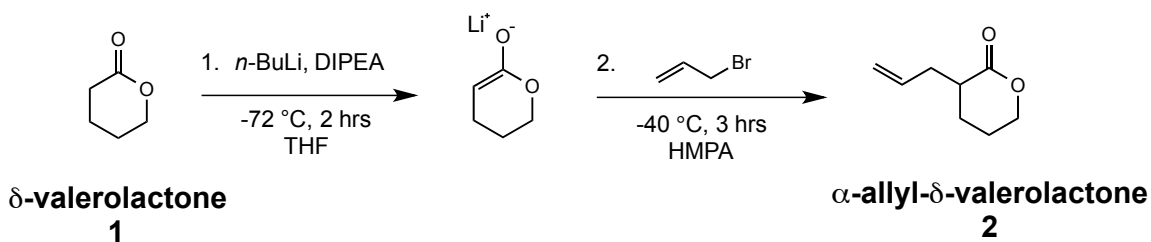
In a 250 mL round bottom flask equipped with stir bar and reflux condenser, a solution of 2,2'-(ethylenedioxy)diethylamine (10.5  $\mu\text{L}$ ,  $7.18 \times 10^{-5}$  mol) in 29.55 mL methylene chloride was heated at 45 °C. A solution of poly(VL-co-AVL-co-EVL), (0.200 g,  $M_w = 3000$  Da) dissolved in methylene chloride was added. The mixture was refluxed at 45 °C for 12 hrs. Residual diamine

crosslinker was removed via dialysis against methylene chloride with Spectra/Por Dialysis Tubing (MWCO = 10,000).  $^1\text{H}$  NMR (400 MHz,  $\text{CDCl}_3/\text{TMS}$ , ppm)  $\delta$ : Decrease in number of epoxide protons at 2.96, 2.75 and 2.47 ppm and the appearance of signals at 3.5 and 2.89 ppm corresponding to the protons near the secondary amine of the diamine crosslinker after the reaction. Same method used for formation of nanosponges from poly(VL-co-AVL-co-OPD-co-EVL) copolymer.

### ***Results and Discussion***

In order to produce polyester-based nanoparticles for drug delivery, linear random copolymer precursors were first synthesized from lactone monomers. These lactone monomers include  $\delta$ -valerolactone,  $\alpha$ -allyl- $\delta$ -valerolactone, and 2-oxepane-1,5-dione. Scheme 2.1 shows the synthesis of  $\alpha$ -allyl- $\delta$ -valerolactone (**2**) from commercially available  $\delta$ -valerolactone (**1**). The availability of an allyl functional group presents an opportunity for further modifications. The synthesis of this monomer involves the formation of an enolate from  $\delta$ -valerolactone, prior to nucleophilic attack by allyl bromide resulting in the allyl substituted  $\delta$ -valerolactone. This monomer product was purified by column chromatography and Kugelrohr distilled in an 89% yield. Figure 2.3 shows a proton NMR of the resulting product, with signals (f, g, h) corresponding to the allyl group in the monomer.

*Synthesis of Allyl-Substituted Valerolactone Monomer using Allyl Bromide*



**Scheme 2.1.** Synthesis of  $\alpha$ -allyl- $\delta$ -valerolactone monomer (AVL) (2).

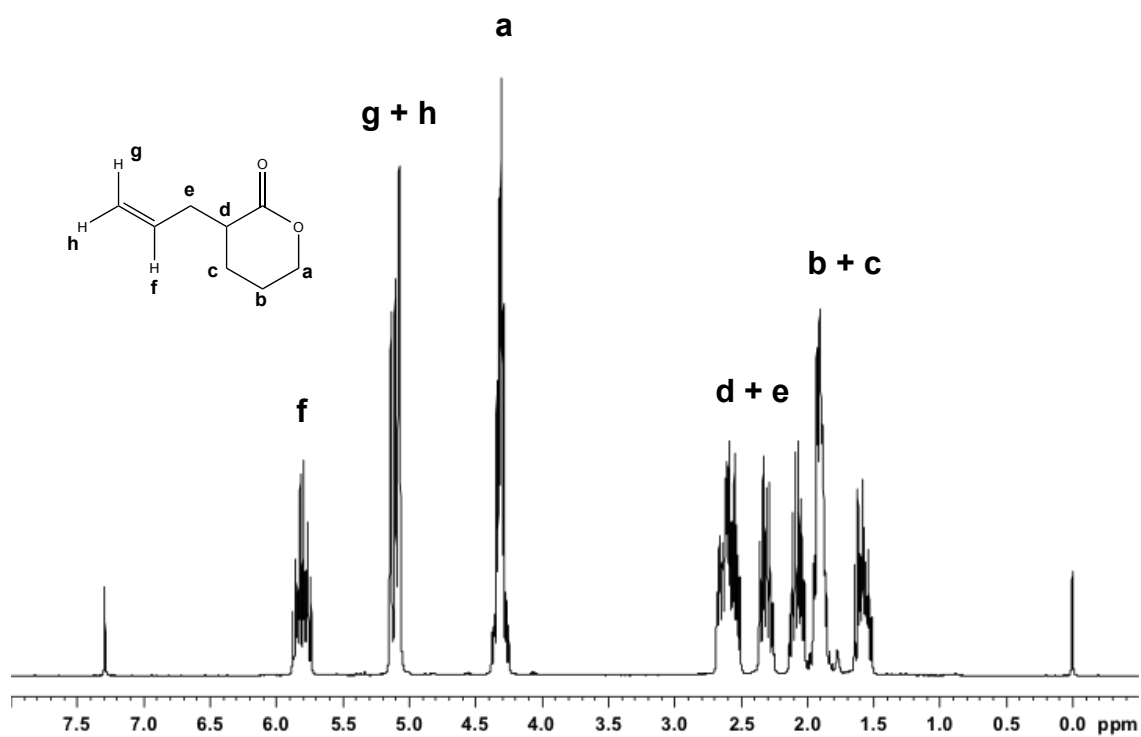
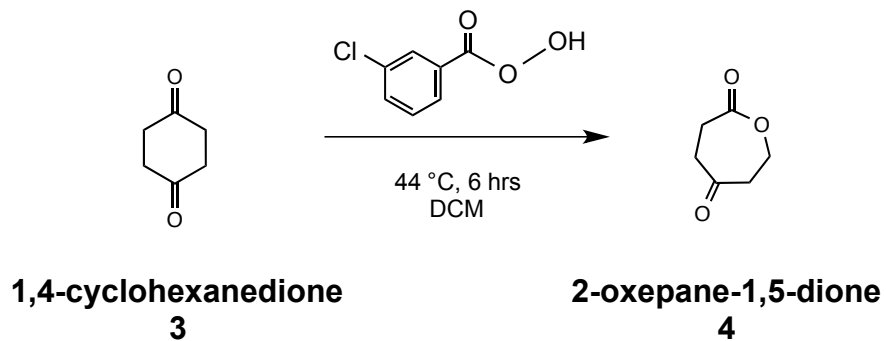


**Figure 2.3.**  $^1\text{H}$  NMR of  $\alpha$ -allyl- $\delta$ -valerolactone monomer in  $\text{CDCl}_3$ .

Synthesis of 2-oxepane-1,5-dione (4) monomer from commercially available 1,4-cyclohexanedione (3) is shown in scheme 2.2. This single step synthesis involves the Baeyer-Villiger oxidation of 1,4-cyclohexanedione with *m*-CPBA to produce a cyclic ester with an additional oxygen. This product was purified by filtration with a yield of 53%. Figure 2.4 shows a proton NMR of the resulting monomer product.



*Synthesis of 2-oxepane-1,5-dione monomer*



**Scheme 2.2.** Synthesis of 2-oxepane-1,5-dione monomer (OPD) (4).

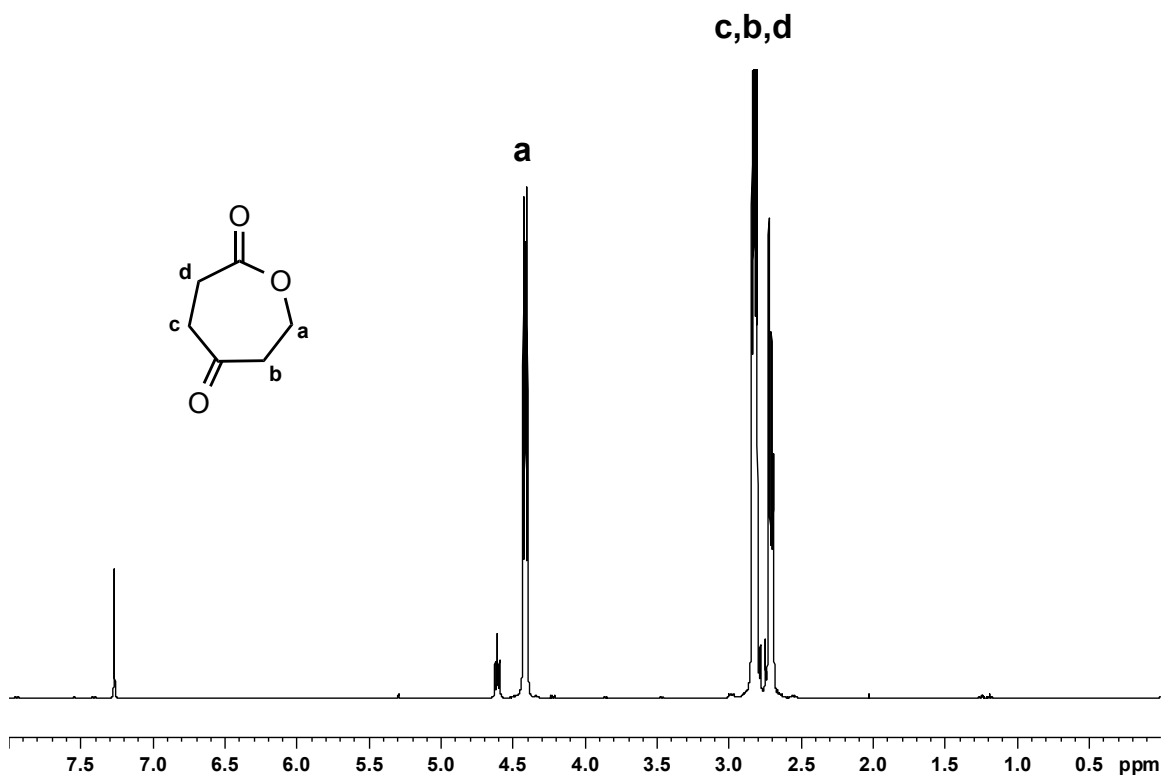
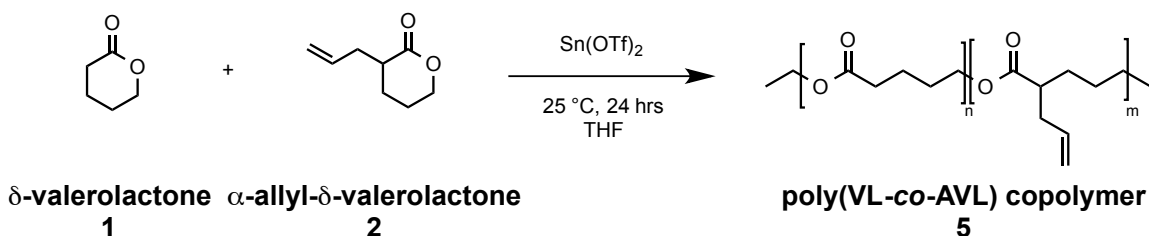


**Figure 2.4.**  $^1\text{H}$  NMR of 2-oxepane-1,5-dione monomer in  $\text{CDCl}_3$ .

Linear random copolymers of these monomers (VL, AVL and OPD) were then produced using ring-opening polymerization (ROP) with ethyl alcohol as an initiator. Previously, Sn(Oct)<sub>2</sub> was used as a catalyst for the ROP of these monomers, however, since linear polymer precursors of narrower polydispersity were desired, Sn(OTf)<sub>2</sub> was investigated as an alternative catalyst. The ROP copolymerization of VL (**1**) and AVL (**2**) using ethyl alcohol initiator led to the formation of poly(VL-*co*-AVL) copolymer (**5**), when in the presence of Sn(OTf)<sub>2</sub> catalyst at 25 °C for 24 hrs. Figure 2.6b shows a table of representative results from six reactions performed. These results show that copolymers of narrow polydispersity were produced with PDIs as low as 1.06, and a single narrow symmetrical peak as shown in the GPC chromatogram (figure 2.6c). Incorporation of the AVL monomer into the copolymer product ranged from 55.7% to 81.4%. Overall yields for this copolymer varied from 44.5% to as high as 94.0%. The molecular weights (M<sub>w</sub>) were calculated based on proton NMR, and were in the range expected. Figure 2.5 shows a proton NMR of the poly(VL-*co*-AVL) copolymer (**5**), with signals (m, n, o) corresponding to the allyl functional group from the AVL (**2**) monomer.

*Copolymerization of α-allyl-δ-valerolactone (AVL) 2 and δ-valerolactone (VL) 1.*



**Scheme 2.3.** Preparation of poly(VL-*co*-AVL) copolymer with Sn(OTf)<sub>2</sub> (**5**).

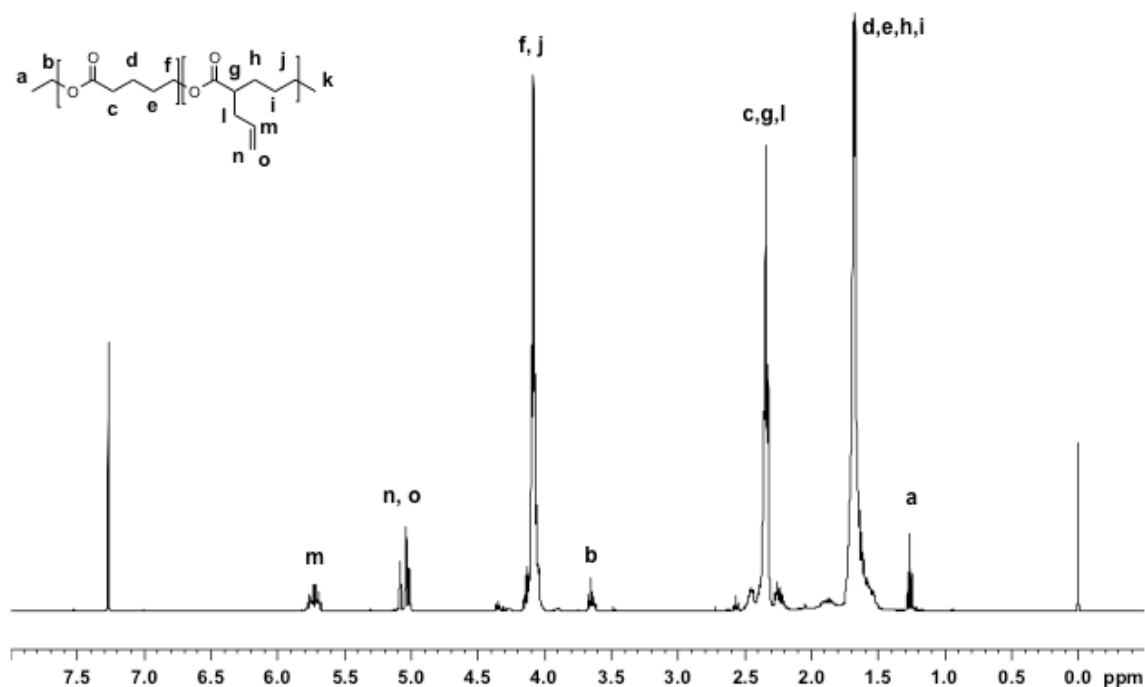
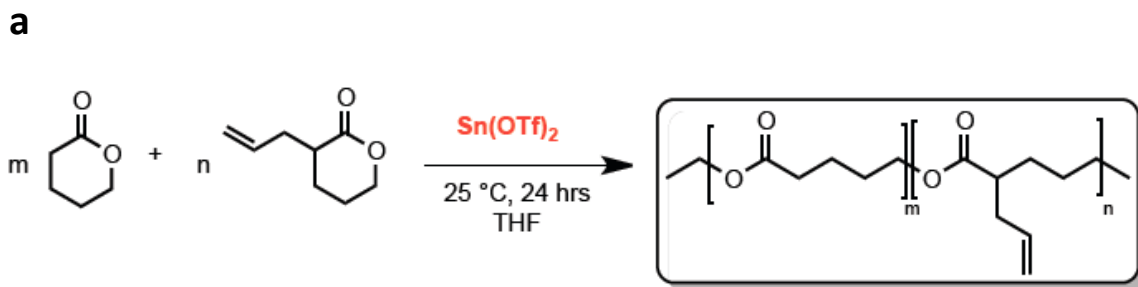


**Figure 2.5.**  $^1\text{H}$  NMR of poly(VL-*co*-AVL) linear polymer in  $\text{CDCl}_3$ .

The ROP copolymerization of VL (**1**), AVL (**2**) and OPD (**4**) using ethyl alcohol initiator led to the formation of poly(VL-*co*-AVL-*co*-OPD) copolymer (**6**), when in the presence of  $\text{Sn}(\text{OTf})_2$  catalyst at  $25\text{ }^\circ\text{C}$  for 24 hrs. Figure 2.9b shows a table of representative results from five reactions performed. These results show that copolymers were produced with a range in PDI from 1.30-1.35, but with a single wider symmetrical peak as shown in the GPC chromatogram (figure 2.9c). These copolymers are of wider polydispersity than copolymer (**5**) made without the use of OPD monomer. Incorporation of the OPD monomer into the copolymer product was much higher than the AVL monomer, and ranged from 89.0% to 98.8%. Overall yields for this copolymer varied from 76.3% to 90.0%. The molecular weights ( $M_w$ ) were calculated based on proton NMR, and were in the range expected.

Preparation of poly(VL-co-AVL) copolymer



**b**

Copolymer	% allyl incorporation	% yield	PDI	M <sub>w</sub> (kg/mol)	Reaction Time (hrs)
1	65.5%	44.5	1.07	2.17	18
2	61.9%	93.8	1.18	2.74	21
3	80.4%	56.8	1.06	2.07	18
4	81.4%	60.2	1.12	2.34	22
5	65.3%	87.5	1.06	4.64	21
6	55.7%	94.0	1.07	4.76	21

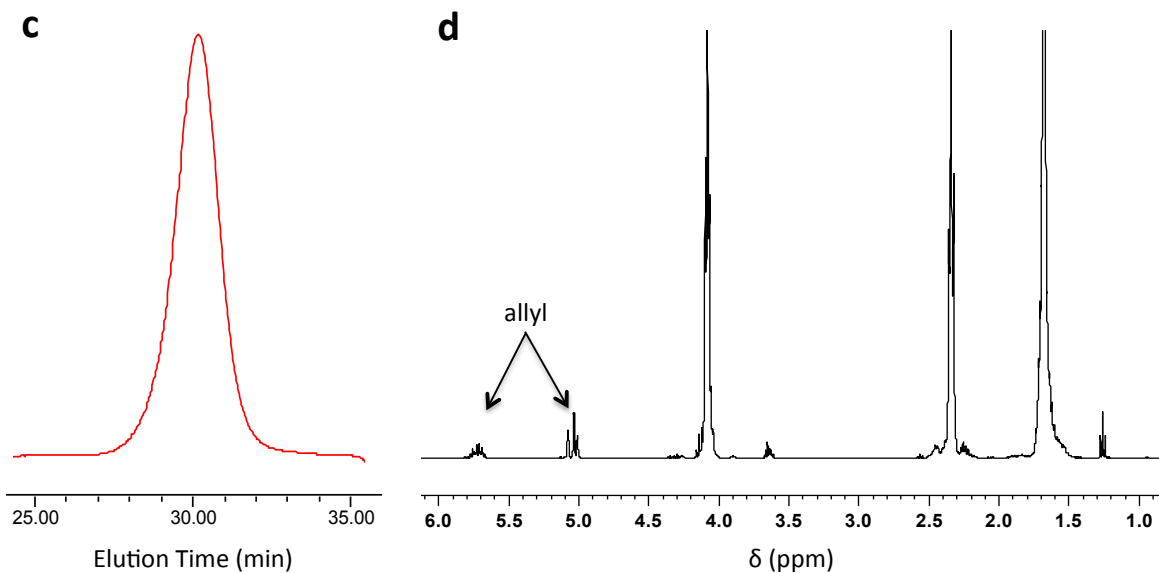
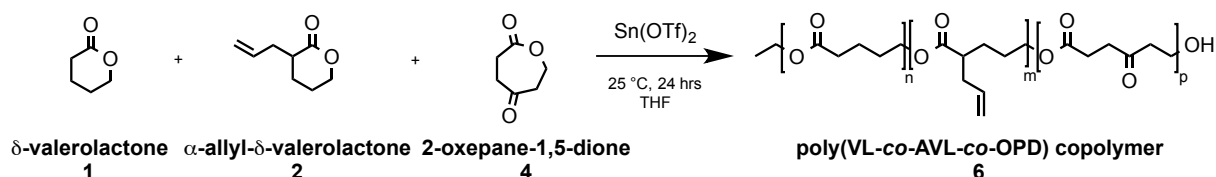


**Figure 2.6.** Characterization of poly(VL-co-AVL) linear copolymer. (A) Scheme for the ring-opening polymerization reaction of AVL and VL monomers using tin (II) triflate catalyst and its linear copolymer product. (B) Table showing % allyl incorporation from <sup>1</sup>H NMR, % yield, polydispersity from GPC, M<sub>w</sub> from <sup>1</sup>H NMR, and reaction time. (C) GPC trace and (D) <sup>1</sup>H NMR spectra in CDCl<sub>3</sub>.

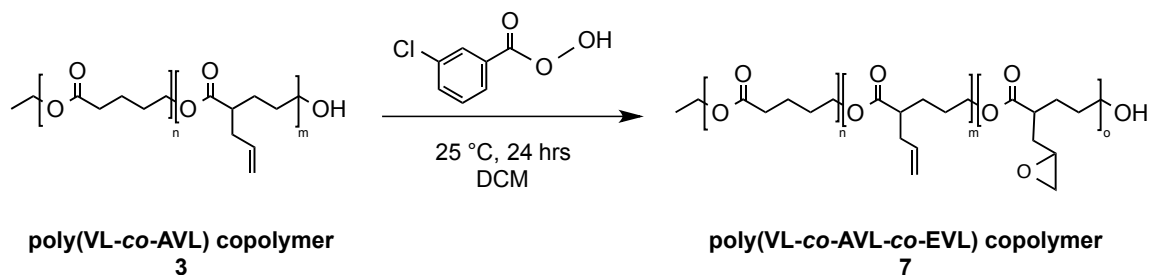
Copolymerization of 2-oxepane-1,5-dione (OPD) **4**,  $\alpha$ -allyl- $\delta$ -valerolactone (AVL) **2** and  $\delta$ -valerolactone (VL) **1**.



**Scheme 2.4.** Preparation of poly(VL-co-AVL-co-OPD) copolymer with Sn(OTf)<sub>2</sub> (**6**).

Partial epoxidation of allyl groups from these linear copolymers converts some of the allyl groups to epoxides, while maintaining the rest for further modifications after nanoparticle formation. Scheme 2.5 shows the partial epoxidation of allyl groups in (**3**) to epoxides in (**7**). The epoxidation of the double bond from the allyl was performed using *m*-CPBA, and produced the epoxidized product in a 76.8% yield. Figure 2.7 and 2.8 show a proton NMR of the resulting copolymer (**7**) product with a reduction in the signals corresponding to the allyl groups (l, m, n) and the appearance of new signals arising from the epoxide groups (t, u).

*Partial epoxidation of poly(VL-co-AVL) **5***



**Scheme 2.5.** Preparation of poly(VL-co-AVL-co-EVL) copolymer (**7**).

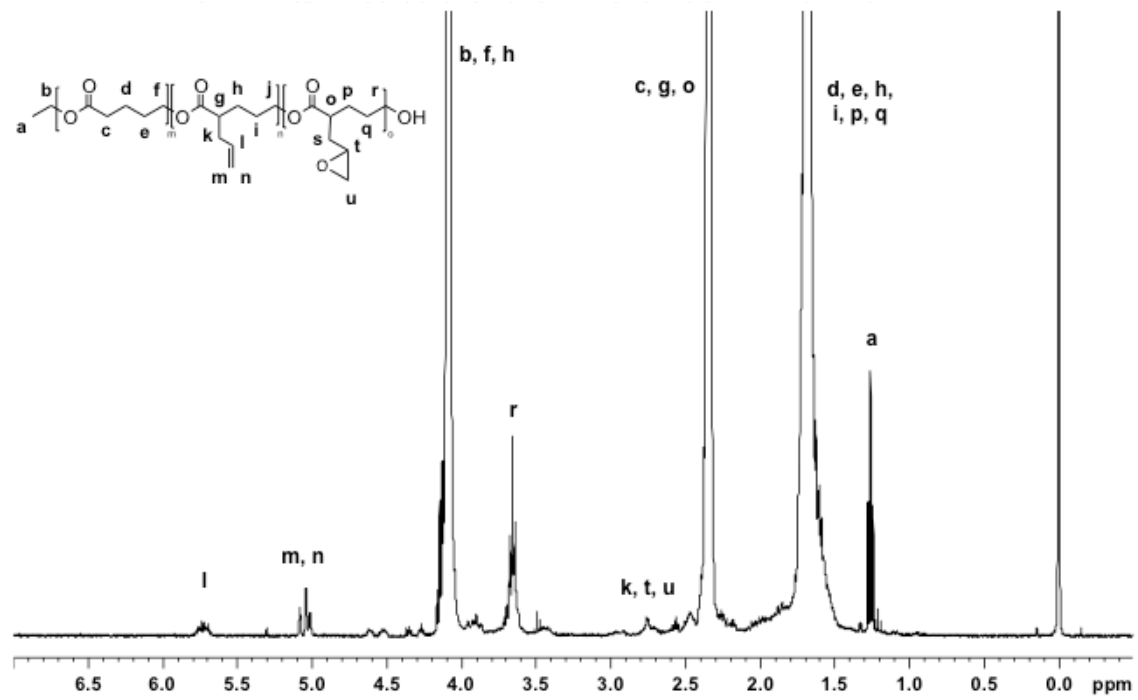


**Figure 2.7.**  $^1\text{H}$  NMR of poly(VL-co-AVL-co-EVL) precursor in  $\text{CDCl}_3$ .

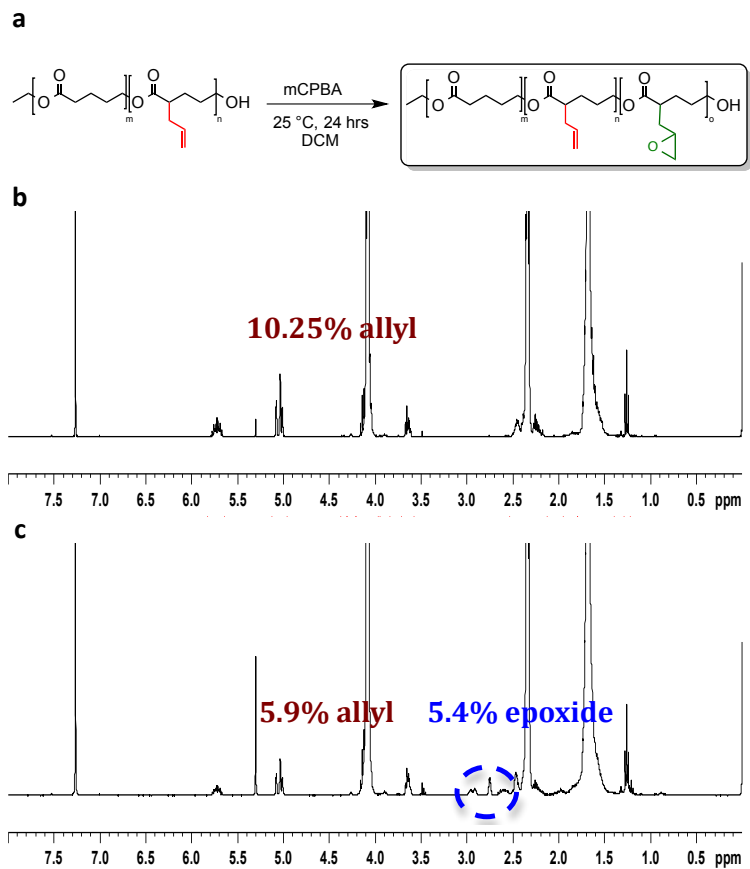


**Figure 2.8.** Characterization of poly(VL-*co*-AVL-*co*-EVL) copolymer. (A) Scheme for the partial epoxidation of allyl groups from its poly(VL-*co*-AVL) copolymer precursor (**3**). (B)  $^1\text{H}$  NMR spectrum in  $\text{CDCl}_3$  for the poly(VL-*co*-AVL) copolymer precursor, showing 10.25% allyl groups. (C)  $^1\text{H}$  NMR spectra in  $\text{CDCl}_3$  for the resulting poly(VL-*co*-AVL-*co*-EVL) copolymer showing conversion of 5.4% of the original allyl groups to epoxides, leaving 5.9% of the original allyl groups.

Preparation of poly(VL-co-AVL-co-OPD) copolymer

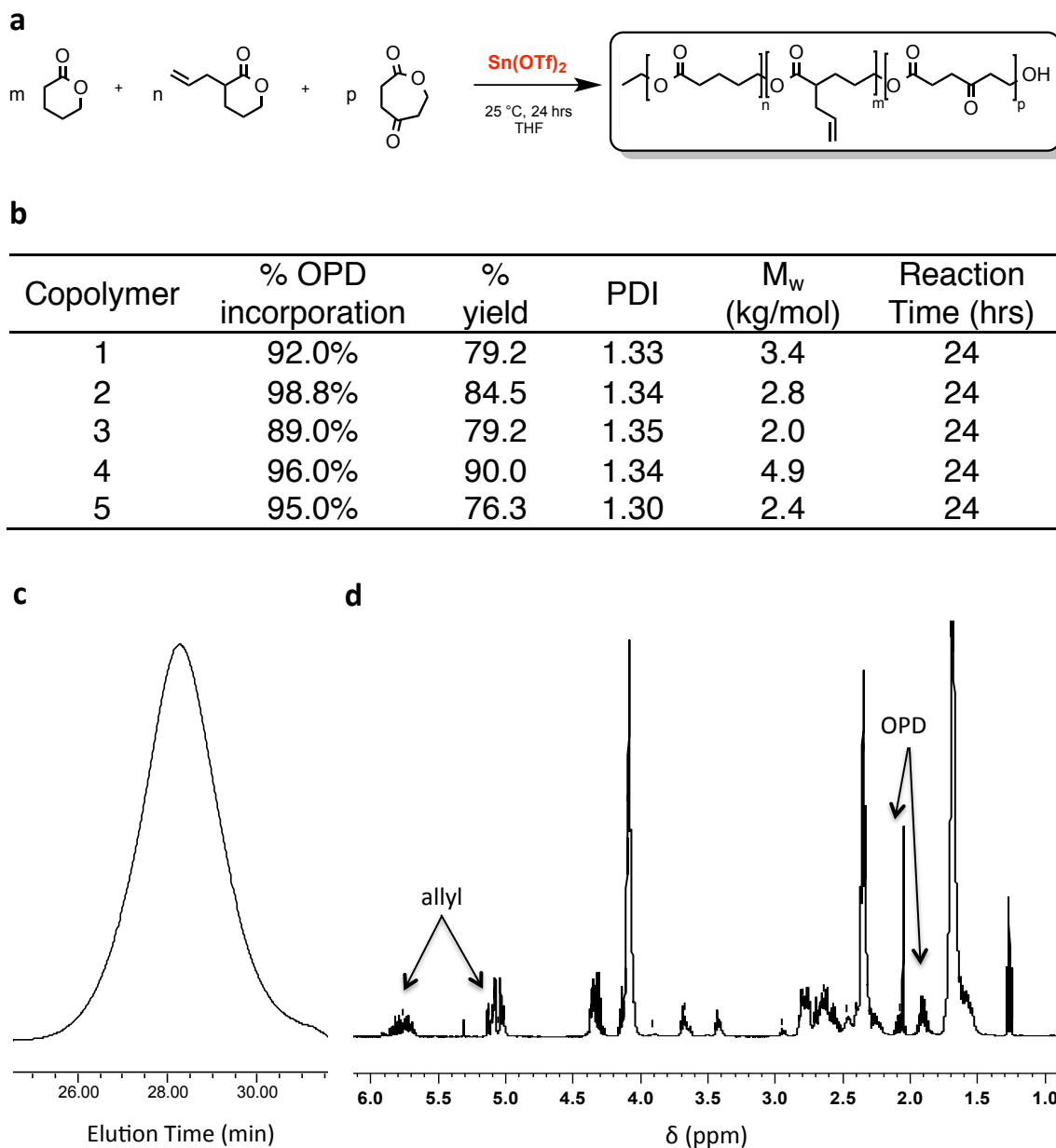
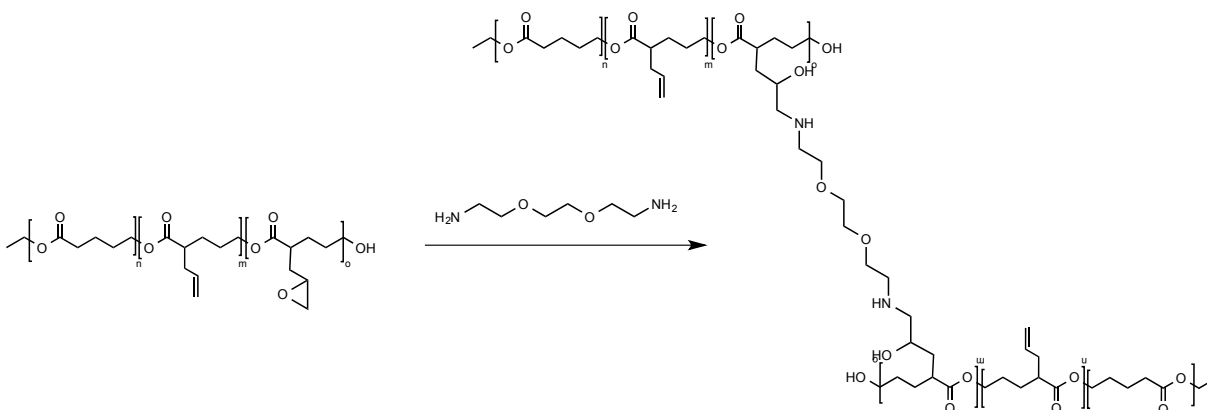


**Figure 2.9.** Characterization of poly(VL-co-AVL-co-OPD) linear copolymer. (A) Scheme for the ring-opening polymerization reaction of OPD, AVL and VL monomers using tin (II) triflate catalyst and its linear copolymer product. (B) Table showing % OPD incorporation from <sup>1</sup>H NMR, % yield, polydispersity from GPC, M<sub>w</sub> from <sup>1</sup>H NMR, and reaction time. (C) GPC trace and (D) <sup>1</sup>H NMR spectra in CDCl<sub>3</sub>.



Nanoparticles were formed from these partially epoxidized copolymers using an intermolecular crosslinking process as shown in scheme 2.6 and figure 2.11. These copolymers have both pendant allyl and epoxide groups, which can be used for various modifications. The epoxide groups are reacted with primary terminal amines from a crosslinker, while refluxing in dichloromethane for 12 hrs. By adjusting the ratio of amines to epoxides, the crosslinking density of the nanoparticle can be tailored to produce varying degradation and drug release rates. These nanoparticles are then purified by dialysis in dichloromethane. Figure 2.10 shows a proton NMR of nanoparticles formed from copolymer (7), with a decrease in the number of epoxide protons (between 2.5 - 3 ppm) and the appearance of new signals near 3.5 ppm (l-u) corresponding to the protons near the secondary amine from the crosslinker after completion of the reaction. Figure 2.11 shows the entire process for the formation of nanoparticles from lactone monomers.

*Formation of nanoparticles using intermolecular crosslinking*



**Scheme 2.6.** Synthesis of poly(VL-co-AVL-co-EVL) nanoparticles.

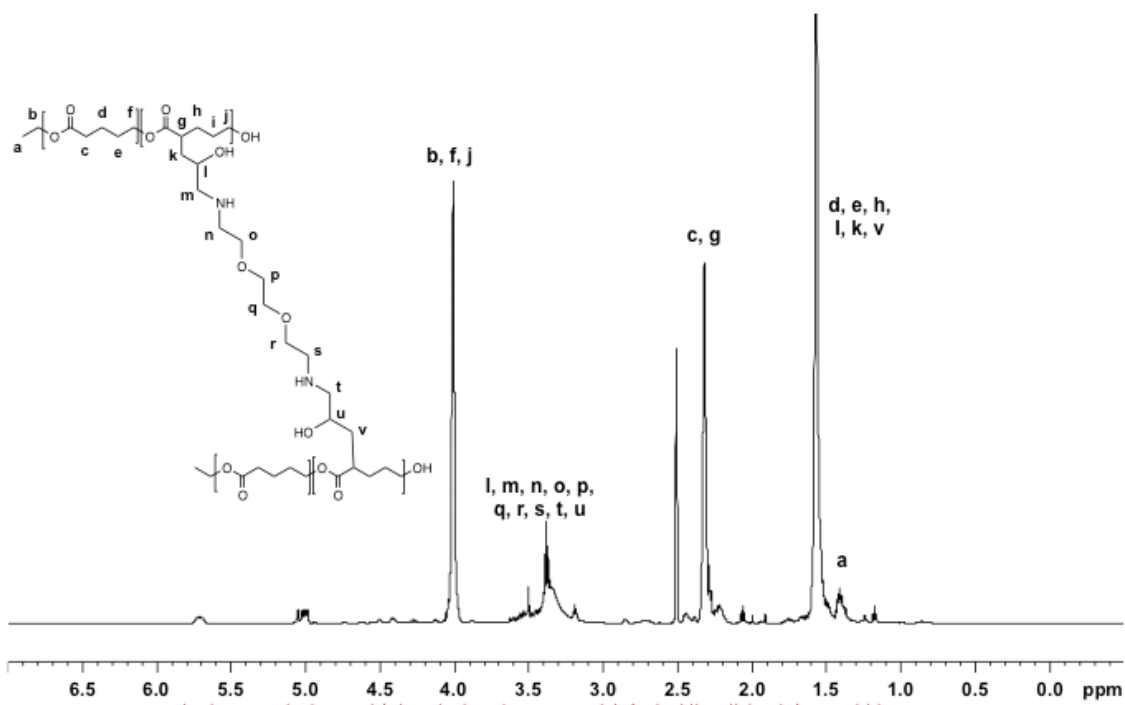


**Figure 2.10.**  $^1\text{H}$  NMR of nanoparticles in  $\text{DMSO-d}_6$ .

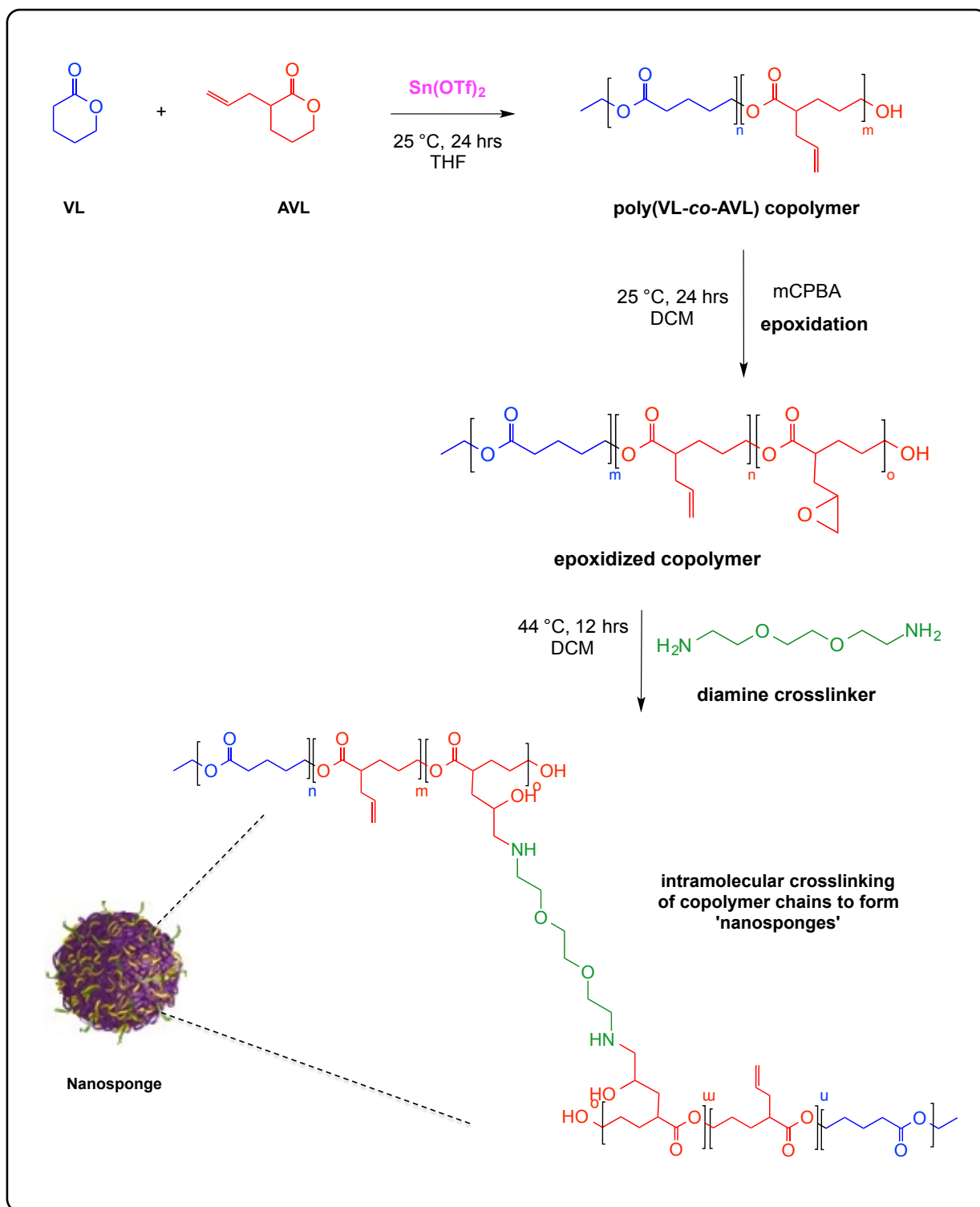


**Figure 2.11.** Diagram of ‘nanosponge’ formation via intermolecular crosslinking of poly(VL-co-AVL) linear copolymers with a diamine crosslinker.

### Characterization of intermolecularly cross-linked nanoparticles

Nanoparticles were characterized by TEM to analyze size and morphology. Figure 2.12 below shows nanoparticles prepared from both poly(VL-co-AVL-co-EVL) and poly(VL-co-AVL-co-OPD-co-EVL) copolymers partially oxidized to produce 5% epoxyvalerolactone (EVL) units. TEM analysis shows nanoparticles of spherical shape with uniform staining. Figure 2.12 shows a representative image taken at 3800x magnification illustrating the distribution of sizes for a typical batch of nanoparticles.

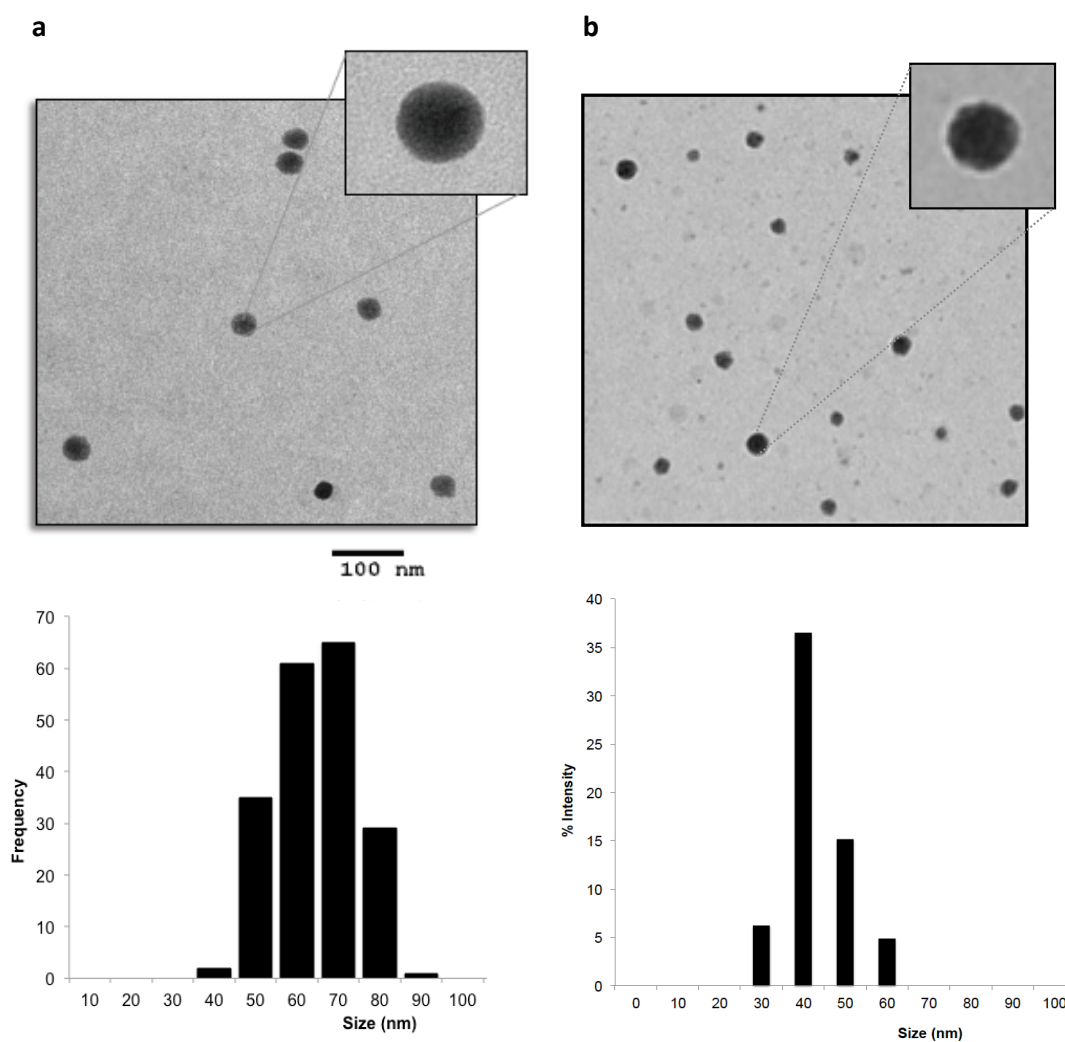
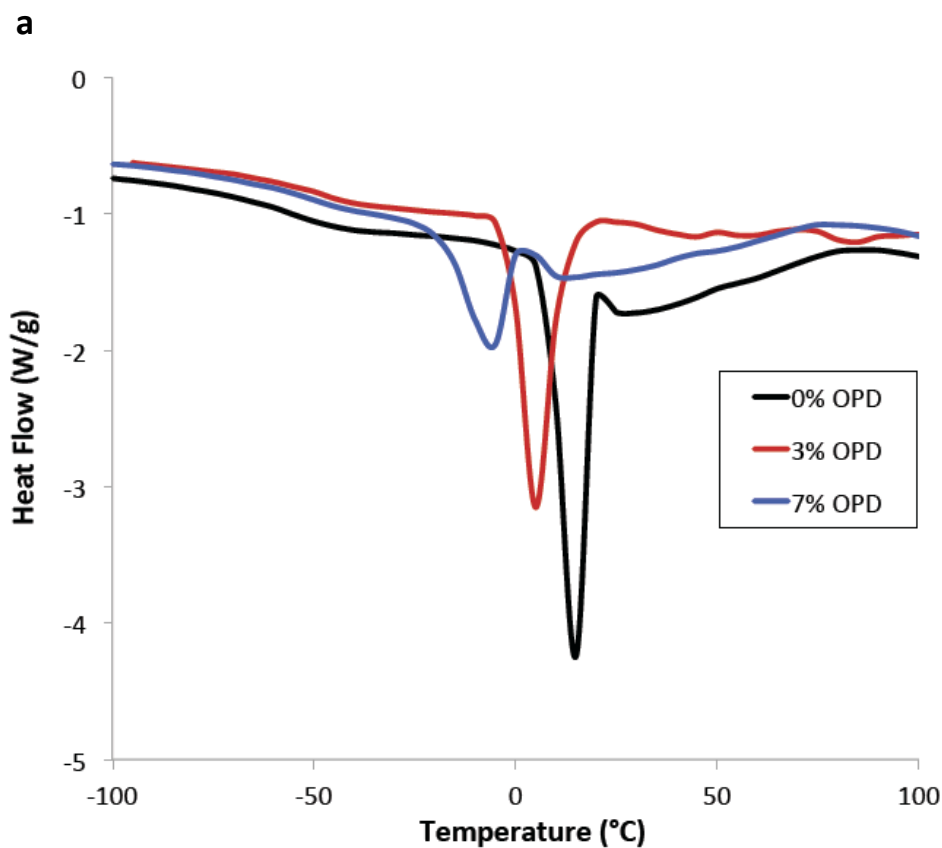


**Figure 2.12.** Size characterization of nanosponges made from tin (II) triflate. TEM micrographs and histograms of (A) poly(VL-co-AVL-co-EVL) nanosponges (left) and (B) poly(VL-co-AVL-co-OPD-co-EVL) nanosponges (right). Scale bar shows 100 nm.

Differential scanning calorimetry analysis of poly(VL-*co*-AVL-*co*-EVL) and poly(VL-*co*-AVL-*co*-EVL-*co*-OPD) nanoparticles was performed to evaluate amorphousness (Figure 2.13). Lower crystallization and melting temperatures were observed with increasing % OPD. All three samples show glass transition temperatures between -50 to -57.5°C, indicating that at physiological temperatures they are amorphous, making them suitable for *in vivo* applications.



**b**

Nanoparticle	%OPD	$T_g$ (°C)	$T_c$ (°C)	$T_m$ (°C)
1	0	-57.5	15	50
2	3	-52.5	5	45
3	7	-50	-15	45

**Figure 2.13.** DSC analysis of poly(VL-*co*-AVL-*co*-EVL-*co*-OPD) nanosponges showing (A) heat flux as a function of temperature. (B) Nanosponges with increasing % OPD at the glass transition temperature ( $T_g$ ), crystallization temperature ( $T_c$ ) and melting temperature ( $T_m$ ).

## **Conclusion**

Use of tin (II) triflate catalyst for ring opening polymerization of lactones is feasible and produces copolymers of narrow PDI with high incorporation of AVL and OPD. Copolymers of *poly(VL-co-AVL)* and *poly(VL-co-AVL-co-OPD)* were prepared and results showed better incorporation of OPD monomer (89-98.8%) in *poly(VL-co-AVL-co-OPD)* compared to AVL monomer (55.7-81.4%) in *poly(VL-co-AVL)*. However, these polymers also showed slightly broader PDI (1.3-1.35) compared to copolymers without OPD (1.06-1.18). PDI increased with presence of OPD, suggesting that the inclusion of this monomer in high quantities creates less uniform polymer chains and a broader distribution of chain lengths. Since this monomer is more polar and hydrophilic, it is possible that it attracts more moisture than the other monomers and this causes greater chain scission, creating a wider distribution of polymer chain lengths.

Reaction conditions for such tin (II) triflate polymerizations are preferable over those of tin (II) octanoate catalysts, with reactions proceeding at room temperature to completion in under 24 hrs compared to temperatures over 100 °C and 48 hrs. These improved conditions are not only more convenient for laboratory preparation of polyesters, they also provide improved yields, and improved monomer incorporation, resulting in greater efficiency per reaction. In addition, narrower polydispersities as achieved with tin (II) triflate compared to tin (II) octanoate produce more uniform polymer chains, which in turn translates to greater control and uniformity of nanoparticle size distribution. This is significant for *in vivo* applications because nanoparticles must remain under 200 nm in order to be compatible with physiological limitations (embolisms, immune response, etc.). In addition, greater uniformity of nanoparticle size distribution also allows for more uniform drug release, making it easier to predict and control drug release profiles for nanoparticles both *in vitro* and *in vivo*.

## References

1. van der Ende A.E., Kravitz E.J. and E. Harth. Approach to formation of multifunctional polyester particles in controlled nanoscopic dimensions. *J. Am. Chem. Soc.* 2008, 130, 8706–8713.
2. van der Ende A.E., Sathiyakumar V., Diaz R., Hallahan D.E. and E. Harth. Linear release nanoparticle devices for advanced targeted cancer therapies with increased efficacy. *Polym. Chem.* 2010, 1, 93–96.
3. van der Ende A.E., Croce T., Hamilton S., Sathiyakumar V. and E. Harth. Tailored polyester nanoparticles: post-modification with dendritic transporter and targeting units via reductive amination and thiol-ene chemistry. *Soft Matter* 2009, 5, 1417–1425.
4. Parrish B., Quansah J.K., and Emrick T. Functional polyesters prepared by polymerization of  $\alpha$ -allyl(valerolactone) and its copolymerization with  $\epsilon$ -caprolactone and  $\delta$ -valerolactone. *J. Polym. Sci. Part A: Polym. Chem.* 2002, 40, 1983–1990.
5. Labet M. and Thielemans W. Synthesis of polycaprolactone: a review. *Chem. Soc. Rev.* 2009, 38, 3484–3504.
6. Lecomte P. and Jerome C. Recent Developments in Ring-Opening Polymerization of Lactones. *Adv. Polym. Sci.* 2012, 245, 173–218.
7. Tang Z.Y., Wang Y., Podsiadlo P. and Kotov N.A. Biomedical applications of layer - by-layer assembly: From biomimetics to tissue engineering. *Adv. Mater.* 2006, 18, 3203–3224.
8. Langer R. Biomaterials in Drug Delivery and Tissue Engineering: One Laboratory's Experience. *Acc. Chem. Res.* 2000, 33, 94.
9. Peppas N.A., Langer R. New challenges in biomaterials. *Science* 1994, 263, 1715-20.
10. Mecerreyes D., Jerome R., Dubois P. Novel macromolecular architectures based on aliphatic polyesters: Relevance of the coordination-insertion ring opening polymerization. *Adv. Polym. Sci.* 1999, 147, 1.
11. Moller M., Kange R. and Hedrick J.L. Sn(OTf)<sub>2</sub> and Sc(OTf)<sub>3</sub>: efficient and versatile catalysts for the controlled polymerization of lactones. *J. Polym. Sci. A Polym. Chem.* 2000, 38, 2067–2074.
12. Albertsson A.C., Edlund U. and Stridsberg K. Controlled ring-opening polymerization of lactones and lactides. *Macromol. Symp.* 2000, 157, 39–46.

13. Stevens D.M., Watson H.A., LeBlanc M.A., Wang R.Y., Chou J., Bauer W.S., Harth E. *Polym. Chem.* 2013, 4, 2470-2474.
14. Lofgren A., Albertsson A.C., Dubois P., Jerome R. and Teyssie P. Synthesis and characterization of biodegradable homopolymers and block copolymers based on 1,5-dioxepan-2-one. *Macromolecules* 1994, 27, 5556-62.
15. Kowalski A., Duda A. and Penczek S. Kinetics and mechanism of cyclic esters polymerization initiated with tin (II) octoate. Polymerization of 1,1 - dilactide. *Macromolecules* 2000, 33, 7359-70.
16. Kowalski A., Duda A. and Penczek S. Kinetics and mechanism of cyclic esters polymerization initiated with tin (II) octanoate. Polymerization of  $\epsilon$ -caprolactone. *Macromol. Rapid Commun.* 1998, 19, 567-72.
17. Nomura N., Taira A., Tomioka T. and Okada M. A catalytic approach for cationic living polymerization: Sc(OTf)<sub>3</sub> catalyzed ring-opening polymerization of lactones. *Macromolecules* 2000, 33, 1497-99.
18. Albertsson A.C. and Varma I.K. Recent developments in ring opening polymerization of lactones for biomedical applications. *Biomacromolecules* 2003, 4, 1466-86.
19. Mohamed F. and van der Walle C.F. Engineering biodegradable polyester particles with specific drug targeting and drug release properties. *J. Pharm. Sci.* 2008, 97, 71 – 87.
20. Moya-Ortega M.D., Alvarez-Lorenzo C., Concheiro A., Loftsson T. Cyclodextrin-based nanogels for pharmaceutical and biomedical applications. *Int. J. Pharm.* 2012, 428, 152-163.
21. Kabanov A.V., Vinogradov S.V. Nanogels as Pharmaceutical Carriers: Finite Networks of Infinite Capabilities. *Angew. Chem. Int. Ed. Engl.* 2009, 48(30), 5418–5429.
22. Raemdonck K., Demeester J., De Smedt S. Advanced nanogel engineering for drug delivery. *Soft Matter* 2009, 5, 707-715.
23. Chacko R.T., Ventura J., Zhuang J., Thayumanavan S. Polymer nanogels: A versatile nanoscopic drug delivery platform. *Adv. Drug Delivery Rev.* 2012, 64, 836-851.
24. Li N., Wang J., Yang X., Li L. Novel nanogels as drug delivery systems for poorly soluble anticancer drugs. *Colloids and Surfaces B: Biointerfaces* 2011, 83, 237-244.
25. Oh J.K., Drumright R., Siegwart D.J., Matyjaszewski K. The development of microgels/nanogels for drug delivery applications. *Prog. Polym. Sci.* 2008, 33, 448-477.
26. Peer D., Karp J.M., Hong S., Farokhzad O.C., Margalit R., Langer R. Nanocarriers as an emerging platform for cancer therapy. *Nat. Nanotechnol.* 2007, 2, 751-760.



27. Murphy E.A., Majeti B.K., Mukthavaram R., Acevedo L.M., Barnes L.A., Cheres D.A. Targeted nanogels: A versatile platform for drug delivery to tumors. *Mol. Cancer Ther.* 2011, 10(6), 972-982.
28. Davis M.E., Chen Z., Shin D.M. Nanoparticle therapeutics: an emerging treatment modality for cancer. *Nat. Rev. Drug Discovery* 2008, 7, 771-782.
29. Yu D., Lu Q., Xie J., Fang C., Chen H. Peptide-conjugated biodegradable nanoparticles as a carrier to target paclitaxel to tumor neovasculature. *Biomaterials* 2010, 31, 2278–2292.
30. Farokhzad O.C., Cheng J., Teply B.A., Sherifi I., Jon S., Kantoff P.W., Richie J.P., Langer R. Targeted nanoparticle-aptamer bioconjugates for cancer chemotherapy in vivo. *Proc. Natl. Acad. Sci.* 2006, 103(16), 6315–6320.
31. Cho K., Wang X., Nie S., Chen Z., Shin D.M. Therapeutic nanoparticles for drug delivery in cancer. *Clin Cancer Res* 2008, 14(5), 1310-1316.
32. Torchilin V.P. Targeted pharmaceutical nanocarriers for cancer therapy and imaging. *The AAPS Journal* 2007, 9(2), E128-E147.
33. Egusquiaguirre S.P., Igartua M., Hernández R.M., Pedraz J.L. Nanoparticle delivery systems for cancer therapy: advances in clinical and preclinical research. *Clin. Transl. Oncol.* 2012, 14, 83-93.
34. Wang A.Z., Langer R., Farokhzad O.C. Nanoparticle delivery of cancer drugs. *Annu. Rev. Med.* 2012, 63, 185-98.
35. Heidel J.D. and Davis M.E. Clinical developments in nanotechnology for cancer therapy. *Pharm. Res.* 2011, 28, 187-199.
36. Wagner V., Dullaart A., Bock A.K., Zweck A. The emerging nanomedicine landscape. *Nat. Biotechnol.* 2006, 24, 1211-1217.
37. Jain R.K., Stylianopoulos T. Delivering nanomedicine to solid tumors. *Nat. Rev. Clin. Oncol.* 2010, 7, 653-664.
38. Caruthers S.D., Wickline S.A., Lanza G.M. Nanotechnological applications in medicine. *Curr. Opinion in Biotech.* 2007, 18, 26-30.
39. Steichen S.D., Caldorera-Moore M., Peppas N.A. A review of current nanoparticle and targeting moieties for the delivery of cancer therapeutics. *Eur. J. Pharm. Science* 2012, 1-11.

40. Byrne J.D., Betancourt T., Brannon-Peppas L. Active targeting schemes for nanoparticle systems in cancer therapeutics. *Adv. Drug Delivery Rev.* 2008, 60, 1615-1626.
41. Farokhzad O.C., Langer R. Impact of nanotechnology on drug delivery. *ACS Nano* 2009, 3, 16-20.
42. Ferrari M. Cancer nanotechnology: opportunities and challenges. *Nat. Rev. Cancer* 2005, 5, 161–171.
43. Langer R. Drug delivery and targeting. *Nature* 1998, 392, 5-10.
44. Langer R. and Folkman J. Polymers for the sustained release of proteins and other macromolecules. *Nature* 1976, 263, 797-800.
45. Bartlett D.W., Su H., Hildebrandt I.J., Weber W.A., Davis M.E. Impact of tumor-specific targeting on the biodistribution and efficacy of siRNA nanoparticles measured by multimodality in vivo imaging. *Proc. Natl. Acad. Sci.* 2007, 104(39), 15549-54.
46. Yallapu M.M., Jaggi M., Chauhan S. Design and engineering of nanogels for cancer treatment. *Drug Discov Today* 2011, 16(9), 457-463.
47. Yu M.K., Park J., Jon S. Targeting strategies for multifunctional nanoparticles in cancer imaging and therapy. *Theranostics* 2012, 2(1), 3-44.
48. Zhang Z., Huey L.S., Feng S.S. Folate-decorated poly(lactide-co-glycolide)-vitamin E TPGS nanoparticles for targeted drug delivery. *Biomaterials* 2007, 28(10), 1889-99.
49. Zhuang J., Jiwanich S., Deepak V.D., Thayumanavan S. Facile preparation of nanogels using activated ester containing polymers. *ACS Macro Lett.* 2012, 1, 175-179.
50. Silvers A.L., Chang C., Emrick T. Functional aliphatic polyesters and nanoparticles prepared by organocatalysis and orthogonal grafting chemistry. *J. Polym. Science Part A: Polym. Chem.* 2012, 1-13.
51. Jérôme C., Lecomte P. Recent advances in the synthesis of aliphatic polyesters by ring-opening polymerization. *Adv Drug Delivery Rev* 2008, 60, 1056-76.
52. Heath F., Haria P., Alexander C. Varying polymer architecture to deliver drugs. *The AAPS Journal* 2007, 9(2), E235-E240.
53. Qiu L.Y., Bae Y.H. Polymer architecture and drug delivery. *Pharm. Res.* 2006, 23(1), 1-30.
54. Su W., Cheng F., Shieh D., Yeh C., Su W. PLGA nanoparticles codeliver paclitaxel and Stat3 siRNA to overcome cellular resistance in lung cancer cells. *Int. J. Nanomedicine* 2012, 7, 4269-4283.

55. Danhier F., Ansorena E., Silva J.M., Coco R., Le Breton A., Préat V. PLGA-based nanoparticles: An overview of biomedical applications. *J. Control Release* 2012, 161, 505-522.
56. Win K.Y., Feng S.S. In vitro and in vivo studies on vitamin E TPGS emulsified poly (D, L-lactic-co-glycolic acid) nanoparticles for paclitaxel formulation. *Biomaterials* 2006, 27(10), 2285-91.
57. Zhang Z., Feng S. Nanoparticles of poly(lactide)/vitamin E TPGS copolymer for cancer chemotherapy: Synthesis, formulation, characterization and in vitro drug release. *Biomaterials* 2006, 27, 262-270.

## CHAPTER 3

### NANOSPONGE DRUG ENCAPSULATION, RELEASE AND IN VITRO CELL STUDIES

#### ***Abstract***

Development of nanoparticle drug delivery systems has allowed greater control over drug release and Despite these advances, however, solubilization of drugs and tailoring drug dosage remains a challenge.<sup>2,3</sup> To address these concerns, biodegradable drug carriers have been investigated and developed for targeting and release of hydrophobic drugs in a controlled manner.<sup>4-6</sup> In particular, ‘nanosponges’ are well suited for these applications due to their biodegradable polyester-based nano-network, composed of a cross-linked 3-dimensional scaffold. These nanoparticles can be produced in different sizes and crosslinking densities, and can be functionalized with tumor targeting units and imaging agents for visualization *in vivo*.<sup>7-9</sup> Hydrophobic drugs can be loaded into these nanoparticles, producing readily injectable formulations with linear sustained drug release.<sup>8</sup>

This study investigated the feasibility of using nanosponge encapsulated paclitaxel and camptothecin to determine the optimum drug combination and sequence for treating lung cancer. Here, the role of drug combination and sequence *in vitro*, in both mouse and human lung cancer cell lines, was investigated using synthesized nanosponges loaded with either paclitaxel (NP PTX) or camptothecin (NP CPT). Results showed not only that paclitaxel and camptothecin combination therapy produced the greatest G2/M phase arrest compared to monotherapy, but also that sequential administration of NP PTX followed by NP CPT further enhanced caspase-

dependent cell death compared to simultaneous administration. Paclitaxel, more so than camptothecin, was observed to drive cells into G2/M phase arrest and subsequent apoptosis. Further studies are necessary to determine the molecular basis for this effect in lung cancer. Sequential administration (NP PTX → NP CPT) of nanoparticle drug delivery systems resulted in greater cell death and decreased cell proliferation. Collectively, these studies suggest that dual combination treatment with administration of paclitaxel prior to camptothecin produces greater G2/M phase arrest, microtubule aggregation, cell death and reduced proliferation compared to simultaneous and monotherapy treatment.

## ***Introduction***

### ***Drug delivery systems***

The development of targeted drug delivery systems has allowed cytotoxic chemotherapeutics to be administered selectively to malignant tumors while sparing healthy tissues from undesirable side effects.<sup>1-6,15</sup> Despite these advances, however, solubilization of drugs and tailoring drug dosage remains a challenge.<sup>2,3</sup> To address these concerns, biodegradable drug carriers have been investigated and developed for targeting and release of hydrophobic drugs in a controlled manner.<sup>4-6</sup> In particular, ‘nanosponges’ are well suited for these applications due to their biodegradable polyester-based nano-network, composed of a cross-linked 3-dimensional scaffold. These nanoparticles can be produced in different sizes and crosslinking densities, and can be functionalized with tumor targeting units and imaging agents for visualization *in vivo*.<sup>7-9</sup> Hydrophobic drugs can be loaded into these nanoparticles, producing readily injectable formulations with linear sustained drug release.<sup>8</sup>

### ***Drug combinations***

The potential of sequential combination drug delivery using these targeted nanocarriers is investigated using mitotic inhibitors and topoisomerase I inhibitors, in addition to establishing tumor targeting of these nanosponges with the HVGGSSV peptide. Paclitaxel (Taxol<sup>®</sup>) has shown promise as a chemotherapeutic alone and in combination with other drugs such as camptothecin in the treatment of a variety of cancers.<sup>14-16,33</sup> As a mitotic inhibitor, its main mechanism of action involves the stabilization of microtubules and G2/M phase cell cycle arrest (Figure 3.1), disruption of mitosis, and apoptosis.<sup>14,15</sup>

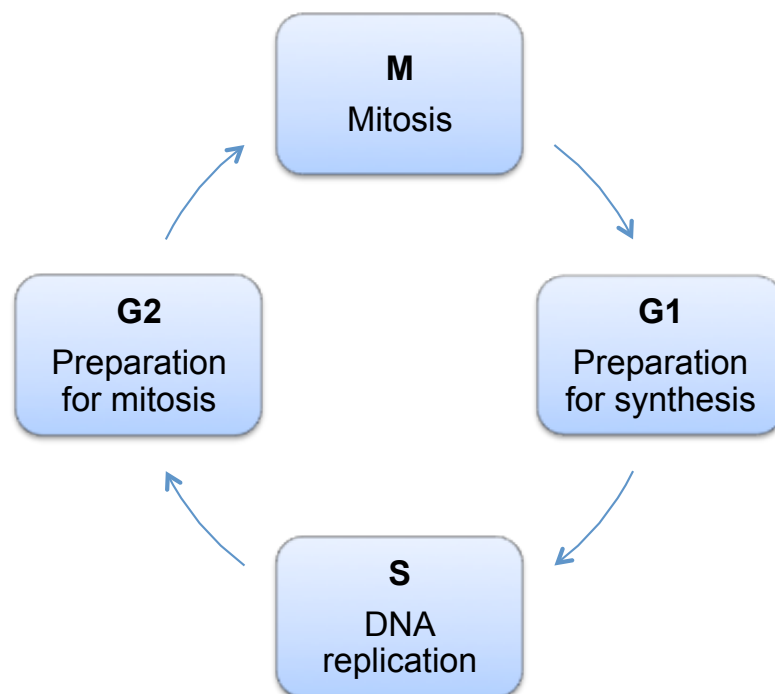


**Figure 3.1.** Phases of the cell cycle: G1 (growth phase 1) preparation for DNA synthesis (6-12 hrs), S phase DNA synthesis (6-8 hrs), G0 (not shown above) resting state, G2 (growth phase 2) preparation for mitosis (3-4 hrs), and M phase shows mitosis or cell division (1 hr).

Camptothecin is a topoisomerase I inhibitor that causes DNA damage by reversibly stabilizing the covalent enzyme-DNA intermediate, causing DNA double strand breaks, S/G2 cell cycle arrest (Figure 3.1) and apoptosis.<sup>16-19,22,23,34,37</sup> Despite its potency, the use of camptothecin in the clinic has been limited greatly due to its poor water solubility, toxicity and side effects. While analogues of camptothecin, such as Irinotecan and Topotecan, have been developed to enhance water solubility, toxicity still remains a limiting side effect.<sup>20</sup> Seliciclib (roscovitine) is a small molecule cyclin-dependent kinase (CDK) inhibitor whose main mechanism of action involves the preferential inhibition of CDK2, 7 and 9.<sup>38-40,31</sup> These CDKs affect the growth phase of the cell cycle by coordinating the division of cells in an accurate and timely manner (Figure 3.1). Disruption of their activation thus serves as a useful way to inhibit the growth and proliferation of cancer cells.<sup>38-40,31</sup> While not as hydrophobic a drug as paclitaxel and camptothecin, seliciclib can still benefit from nanoparticle technology as it can deliver greater concentrations of drug to tumors.

Targeted drug delivery systems that provide sustained release of highly hydrophobic small molecules specifically at tumor sites exhibit particular promise for combination chemotherapy, where delivery of lower doses for extended times can help enhance efficacy and reduce toxicity. Moreover, continuous low doses of drug over time (metronomic chemotherapy), also allows for greater anti-angiogenic efficacy.<sup>21</sup> Biodegradable targeted nanosponges with a cross-linked polymeric architecture create controlled low dose drug release profiles that are highly suitable for this application. In this chapter, the optimal dual drug combination and treatment schedule are determined for drug-loaded nanoparticles using *in vitro* assays in lung and prostate cancer cell lines. These results are then used in chapter 5 to investigate effects in an *in vivo* lung cancer model.

## ***Experimental***

### *Materials and Methods*

*Reagents.* Chemical reagents were purchased from Sigma-Aldrich and Strem Chemicals, and used as received unless otherwise stated. Chemotherapeutic drugs from LC Laboratories. Peptides (GCGGGNHVGGSSV) were purchased from EZBiolab Inc. (Carmel, IN). Spectra/Por<sup>®</sup> Dialysis membrane (MWCO=10,000) in 0.05% sodium azide was purchased from Spectrum Laboratories. SnakeSkin<sup>®</sup> Pleated Dialysis Tubing, regenerated cellulose, was purchased from Pierce Biotechnology.

### *Preparation of Monomers*

#### *$\delta$ -valerolactone monomer (VL)*

Technical grade  $\delta$ -valerolactone was Kugelrohr distilled to produce a colorless liquid product.

#### *$\alpha$ -allyl- $\delta$ -valerolactone monomer (AVL)*

A flame dried 500 mL two-necked round bottom flask was equipped with a stir bar, sealed with a rubber septum, and purged with nitrogen for 30 min. To the flask, 156.25 mL of anhydrous THF was added and cooled to -78 °C in a dry ice/acetone bath. Following this, a basic solution of lithium diisopropylamine was produced by adding redistilled n,n-diisopropylamine (3.3 mL, 23.63 mmol) and n-butyl lithium (2.5 M in hexanes) (9.35 mL, 23.38 mmol) dropwise via syringe. This solution was stirred for 20 minutes. A nitrogen purged solution of distilled  $\delta$ -valerolactone (1.97 mL, 21.23 mmol) in anhydrous THF (56 mL) was then added dropwise via syringe over 30 min. After an additional 30 min of stirring, a nitrogen purged solution of allyl bromide (2.21 mL, 25.54 mmol) in hexamethylphosphoramide (4.43 mL, 25.46 mmol) was added via syringe. The reaction mixture was warmed up to -40 °C and stirred for 2 hrs. The



reaction was quenched with excess  $\text{NH}_4\text{Cl}$  solution. The crude product was concentrated via rotary evaporator, washed three times with saturated  $\text{NaCl}$  solution, and dried with anhydrous magnesium sulfate. The crude product was purified via column chromatography (Biotage Isolera), analyzed by thin layer chromatography and Kugelrohr distilled. Chromatography with a gradient of 5-20% ethyl acetate in n-hexanes as eluent gave a yellow liquid product. Kugelrohr distillation produced a colorless liquid product. Yield: 3.56 g (89%).  $^1\text{H}$  NMR (400MHz,  $\text{CDCl}_3/\text{TMS}$ , ppm)  $\delta$ : 5.7 (m, 1H,  $\text{H}_2\text{C}=\text{CH}-$ ), 5.08 (m, 2H,  $\text{H}_2\text{C}=\text{CH}-$ ), 4.28 (m, 2H,  $-\text{C}(\text{O})\text{OCH}_2-$ ), 2.53-2.58 (m, 2H,  $\text{H}_2\text{C}=\text{CHCH}_2-$ ), 2.27 (m, 1H,  $\text{H}_2\text{C}=\text{CHCH}_2\text{CH}-$ ), 2.06 (m, 1H,  $\text{H}_2\text{C}=\text{CHCH}_2\text{CHCH}_2-$ ), 1.89 (m, 2H,  $\text{C}(\text{O})\text{OCH}_2\text{CH}_2-$ ), 1.55 (m, 1H,  $\text{H}_2\text{C}=\text{CHCH}_2\text{CHCH}_2-$ ).

#### *Preparation of Linear Polymer Precursors*

##### *Poly(VL-co-AVL) from $\text{Sn}(\text{OTf})_2$ catalyst*

A flame dried 25 mL 3-necked round bottom flask was equipped with a stir bar, sealed with rubber septa and nitrogen purged. A stock solution of anhydrous ethanol in anhydrous tetrahydrofuran was prepared (1.7 M) in a 50 mL flame dried and nitrogen purged round bottom flask, and a stock solution of  $\text{Sn}(\text{OTf})_2$  catalyst in anhydrous tetrahydrofuran was prepared ( $3.7 \times 10^{-2}$  M) in a 10 mL flame dried and nitrogen purged round bottom flask. Ethanol (584  $\mu\text{L}$ , 1.0 mmol) and  $\text{Sn}(\text{OTf})_2$  (261  $\mu\text{L}$ ,  $9.64 \times 10^{-6}$  mol) were added via syringe to the 25 mL 3-neck round bottom flask and the catalyst/initiator solution was allowed to stir at room temperature for 30 minutes prior to simultaneous addition of  $\delta$ -valerolactone (2.22 g, 22.0 mmol) and  $\alpha$ -allyl(valerolactone) (0.777 g, 5.548 mmol) monomers via syringe. After addition of both monomers, the reaction was stirred for 24 hrs at room temperature. The resulting polymer was diluted with 1 mL anhydrous THF and purified by dropwise addition into 1 L of chilled methanol to remove any remaining monomer and catalyst. The methanol was decanted and the precipitate

dissolved in methylene chloride, rotary evaporated and dried *in vacuo*. The resulting polymer was observed as a waxy white solid.  $M_w = 3000$  Da; PDI = 1.09;  $^1\text{H}$  NMR (400 MHz,  $\text{CDCl}_3/\text{TMS}$ , ppm)  $\delta$ : 5.72 (m,  $\text{H}_2\text{C}=\text{CH}-$ ), 5.04 (m,  $\text{H}_2\text{C}=\text{CH}-$ ), 4.08 (m,  $-\text{CH}_2-\text{O}-$ ), 3.64 (m,  $\text{CH}_3\text{CH}_2\text{O}-$ ), 2.34 (m, vl,  $-\text{CH}_2\text{CH}_2\text{C}(\text{O})\text{O}-$ , avl,  $\text{H}_2\text{C}=\text{CHCH}_2\text{CH}-$ ,  $\text{H}_2\text{C}=\text{CHCH}_2\text{CH}-$ ), 1.68 (m, avl and vl,  $-\text{CHCH}_2\text{CH}_2-$ ), 1.26 (t,  $\text{CH}_3\text{CH}_2\text{O}-$ ).

*Poly(VL-co-AVL) from Sn(Oct)<sub>2</sub> catalyst*

A flame dried 25 mL 3-necked round bottom flask was equipped with a stir bar, sealed with rubber septa and nitrogen purged. A stock solution of anhydrous ethanol in anhydrous tetrahydrofuran was prepared (1.7 M) in a 25 mL flame dried and nitrogen purged round bottom flask, and a stock solution of  $\text{Sn}(\text{Oct})_2$  catalyst in anhydrous tetrahydrofuran was prepared in a 10 mL flame dried and nitrogen purged round bottom flask. Ethanol (360  $\mu\text{L}$ ,  $6.14 \times 10^{-1}$  mol) and  $\text{Sn}(\text{Oct})_2$  (330  $\mu\text{L}$ ,  $1.22 \times 10^{-2}$  mol) were added via syringe to the 50 mL 3-neck round bottom flask and the catalyst/initiator solution was allowed to stir at room temperature for 30 minutes prior to simultaneous addition of  $\delta$ -valerolactone (2.46 g,  $28.53 \times 10^{-3}$  mol) and  $\alpha$ -allyl(valerolactone) (0.93 g,  $7.134 \times 10^{-3}$  mol) monomers via syringe. After addition of both monomers, the reaction was stirred for 48 hrs at 105 °C in an oil bath. The resulting polymer was diluted with 1 mL methylene chloride and purified by dropwise addition into 1.5 L of chilled diethyl ether to remove any remaining monomer and catalyst. The ether was decanted and the precipitate dissolved in methylene chloride, rotary evaporated and dried *in vacuo*. The resulting polymer was observed as a viscous yellow liquid.  $^1\text{H}$  NMR (300 MHz,  $\text{CDCl}_3/\text{TMS}$ , ppm)  $\delta$ : 5.72 (m,  $\text{H}_2\text{C}=\text{CH}-$ ), 5.04 (m,  $\text{H}_2\text{C}=\text{CH}-$ ), 4.08 (m,  $-\text{CH}_2-\text{O}-$ ), 3.64 (m,  $\text{CH}_3\text{CH}_2\text{O}-$ ), 2.34 (m, vl,  $-\text{CH}_2\text{CH}_2\text{C}(\text{O})\text{O}-$ , avl,  $\text{H}_2\text{C}=\text{CHCH}_2\text{CH}-$ ,  $\text{H}_2\text{C}=\text{CHCH}_2\text{CH}-$ ), 1.68 (m, avl and vl,  $-\text{CHCH}_2\text{CH}_2-$ ), 1.26 (t,  $\text{CH}_3\text{CH}_2\text{O}-$ ).

### *Poly(VL-co-AVL-co-EVL)*

In a 100 mL round bottom flask, equipped with stir bar and rubber septum, a solution of poly(VL-co-AVL) (1.0 g,  $1.55 \times 10^{-3}$  mol) was dissolved in 8.5 mL of methylene chloride. To this solution, meta-chloroperoxybenzoic acid (121.25 mg,  $7.03 \times 10^{-4}$  mol) was added. The solution was stirred for 24 hrs at room temperature and then concentrated via rotary evaporator. The crude product was dissolved in a minimal amount of dichloromethane (2 mL) and precipitated into an Erlenmeyer flask containing 500 mL cold diethyl ether. The solution was decanted, and the white solid was rotary evaporated and dried *in vacuo* to obtain the final white waxy polymer. Yield: 0.768 g (76.8%).  $^1\text{H}$  NMR (400MHz,  $\text{CDCl}_3/\text{TMS}$ , ppm)  $\delta$ : Decrease in allylic protons at 5.7 and 5.09 ppm and the appearance of small broad resonance peaks at 2.96, 2.75 and 2.47 ppm due to the formation of the epoxide.

### *Formation of nanosponges*

In a 250 mL round bottom flask equipped with stir bar and reflux condenser, a solution of 2,2'-(ethylenedioxy) diethylamine (10.5  $\mu\text{L}$ ,  $7.18 \times 10^{-5}$  mol) in 29.55 mL methylene chloride was heated at 45 °C. A solution of poly(VL-co-AVL-co-EVL), (0.200 g,  $M_w = 3000$  Da) dissolved in methylene chloride was added. The mixture was refluxed at 45 °C for 12 hrs. Residual diamine crosslinker was removed via dialysis against methylene chloride with Spectra/Por Dialysis Tubing (MWCO = 10,000). Nanosponges were made from poly(VL-co-AVL) using  $\text{Sn}(\text{OTf})_2$  and  $\text{Sn}(\text{Oct})_2$  catalysts.  $^1\text{H}$  NMR (400 MHz,  $\text{CDCl}_3/\text{TMS}$ , ppm)  $\delta$ : Decrease in number of epoxide protons at 2.96, 2.75 and 2.47 ppm and the appearance of signals at 3.5 and 2.89 ppm corresponding to the protons near the secondary amine of the diamine crosslinker after the reaction.

### *Drug Encapsulation of Paclitaxel and Camptothecin in Nanoparticles*

Poly(VL-co-AVL-co-EVL) nanoparticles were encapsulated separately with either paclitaxel or camptothecin and emulsified with D- $\alpha$ -tocopheryl polyethylene glycol 1000 succinate (vitamin E-TPGS). Nanoparticles (30 mg) and paclitaxel (10 mg) were dissolved together in 1 mL dimethyl sulfoxide (DMSO), and nanoparticles (30 mg) and camptothecin (30 mg) were dissolved together in 2 mL DMSO prior to dropwise addition to a solution of 0.5% and 2% vitamin E-TPGS in distilled water, respectively. The solution was stirred vigorously to form a cloudy white suspension over 1-2 minutes and decanted into 50 mL centrifuge tubes. They were centrifuged at 7800 rpm for 30 min, and the pellet washed three times by reconstitution in water and centrifugation at 7800 rpm for 30 min each. The emulsified drug encapsulated nanoparticles were then lyophilized to produce a powder and analyzed by UV-Vis spectrophotometry to give approximately 15% drug encapsulation for each drug. (See appendix for calibration curves for each drug).

### *Cell Culture*

Murine Lewis lung carcinoma (LLC) and A549 lung human carcinoma cells were obtained from the American Type Culture Collection (Rockville, MD.). They were grown to 70% confluence in Dulbecco's Modified Eagle Medium or F-12K medium each supplemented with 10% fetal bovine serum and 1% antibiotic/antimycotic, respectively. All cultures maintained at 37°C in incubator with 95% humidity and 5% CO<sub>2</sub>.

### *Flow Cytometry*

#### *Serum-starved cell cycle analysis*

LLC cells were phase synchronized with serum deprived cell media for 24 hrs prior to treatment at IC<sub>50</sub> concentrations for each drug or nanoparticle controls for 24 hrs. Sequential treatment

groups were also treated with drug loaded nanoparticles for 24 hrs (12 hrs each drug, washed with PBS before second drug), washed with PBS, detached and fixed with cold 70% ethanol. All cells were stained with a solution of propidium iodide (50  $\mu\text{g}/\text{mL}$ ) in PBS with 0.1% Triton X-100 and RNase (200  $\mu\text{g}/\text{mL}$ ) overnight at 4 °C. After washing twice with PBS, cells were filtered and analyzed by flow cytometry.

#### *Apoptosis studies*

LLC cells were seeded in 6-well tissue culture plates and incubated for 24 hrs. After 72 hrs treatment with drug encapsulated nanoparticles or untreated controls, cells were washed with PBS, detached and fixed with cold 70% ethanol. Cells were then incubated with rabbit anti-cleaved caspase-3 primary antibody, washed and incubated with FITC labeled secondary antibody. After washing twice with PBS, cells were filtered and apoptotic cell populations were quantified by flow cytometry. All flow cytometry performed using a Becton Dickinson 3-laser LSRII flow cytometer. Results were analyzed using FlowJo software.

#### *Microtubule and proliferation studies: Cell imaging*

Human A549 lung carcinoma cells were grown on cover slips and treated with drug loaded nanoparticles or vehicle (DMSO) for 72 hrs, at  $\text{IC}_{50}$  (10  $\mu\text{M}$  for NP PTX and 1  $\mu\text{M}$  for NP CPT) concentrations for each drug or nanoparticle controls. Simultaneous treatment groups were treated with drug-loaded nanoparticles for 72 hrs (NP PTX/NP CPT) Sequential treatment groups were treated with drug-loaded nanoparticles for 72 hrs. NP PTX  $\rightarrow$  NP CPT group was exposed to PTX for 36 hrs, washed with PBS and exposed to CPT for another 36 hrs. NP CPT  $\rightarrow$  NP PTX group was exposed to CPT for 36 hrs, washed with PBS and exposed to PTX for another 36 hrs. All groups were washed twice with PBS and fixed with 4% paraformaldehyde. Microtubules were stained with anti-beta tubulin antibody conjugated with FITC. Proliferating

cells were stained with human anti-Ki67 antibody conjugated with Alexa Fluor 647. Slides were mounted using FluoroShield prior to confocal microscopy. *In vitro* imaging was performed using a Zeiss LSM 710 Meta Inverted confocal microscope at 63x magnification. Images were acquired from three fields of view and the numbers of cells showing changes in microtubule morphology or expression of Ki67 cell proliferating marker were counted. Bar graphs shown represent the number of cells as a percentage of total cells counted. All images were analyzed using MetaMorph and ZEN image acquisition and analysis software.

## ***Results and discussion***

### *Drug release studies: Paclitaxel and Camptothecin*

Poly(VL-co-AVL-co-EVL) nanosponges of varying cross-linking density (5% and 8%) were loaded separately with paclitaxel or camptothecin for analysis of drug release over time (Figure 3.2). Nanosponges with lower cross-linking density (5% epoxide) were observed to have a faster drug release rate for paclitaxel, with over 20% of total drug loaded being released by 24 hrs. In contrast, nanosponges of similar cross-linking density loaded with camptothecin showed less than 10% release by 24 hrs. Nanosponges with higher cross-linking density (8% epoxide) were observed to have a relatively slower drug release rate for paclitaxel, with approximately 10% release by 24 hrs. This pattern is also observed with camptothecin, with approximately 10% release by 24 hrs as well. Differences in molecular weight and hydrophobicity may affect the rate of drug release in these drugs, by affecting the rate at which individual drug molecules diffuse out of the nanosponge.

### *Cytotoxicity Studies*

Nanosponges were loaded separately with paclitaxel, camptothecin, or seliciclib and used to treat mouse and human lung carcinoma cells. *In vitro* dose-response curves for mouse lung cancer cells LLC (left) and human A549 (right) were treated with various drug combinations for 24 hrs (Figure 3.3). In both cell lines, the combination of paclitaxel/camptothecin lowered  $IC_{50}$  values most followed by camptothecin/seliciclib and paclitaxel/seliciclib.

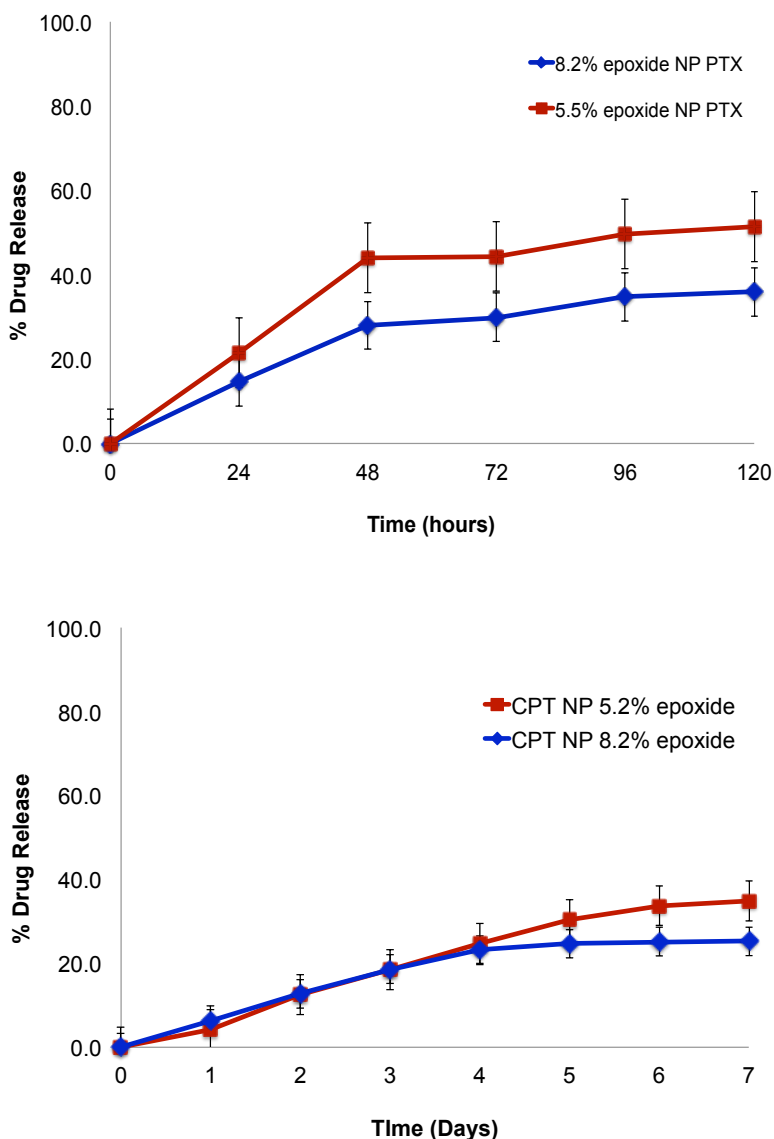


**Figure 3.2.** Drug release studies with poly(VL-co-AVL-co-EVL) nanosponges in phosphate buffered saline at 37 °C. (A) Paclitaxel loaded nanosponges with 5% and 8% cross-linking density and (B) Camptothecin loaded nanosponges with 5% and 8% cross-linking density.

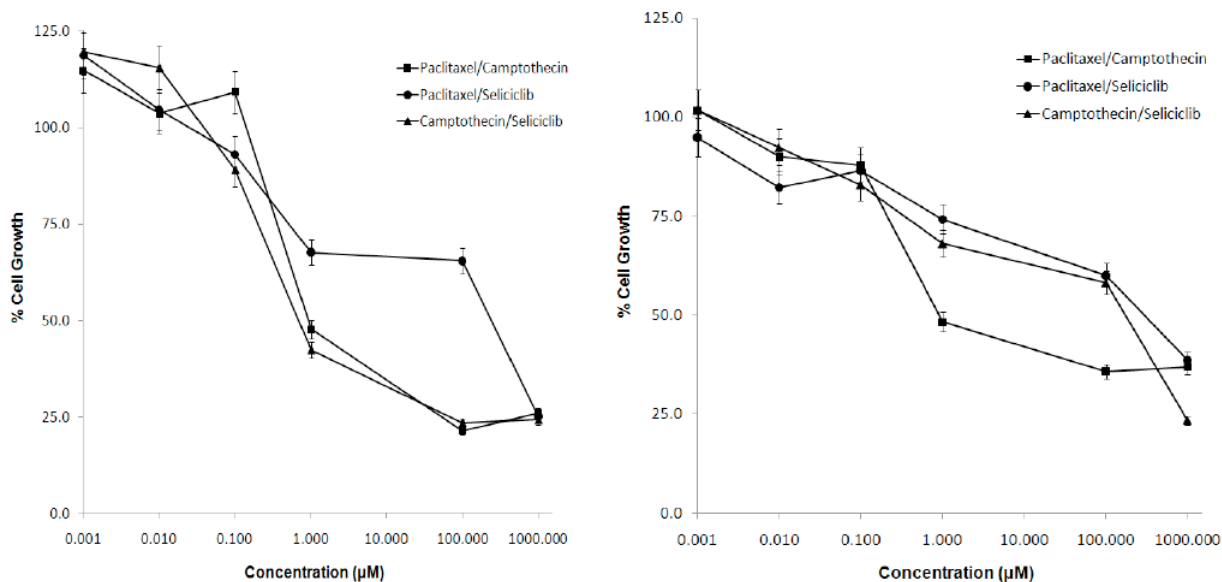


**Figure 3.3.** MTT cytotoxicity assays with poly(VL-*co*-AVL-*co*-EVL) nanosponges of 5% epoxide cross-linking density. *In vitro* dose-response curves for lung cancer cells LLC (left) and A549 (right) treated with various drug combinations for 24 hrs. In both cell lines, the combination of paclitaxel/camptothecin lowered IC<sub>50</sub> values most followed by camptothecin/selaciclib and paclitaxel/selaciclib.

In this study we synthesized ‘nanosponges’ (see chapter 2) for tumor-specific delivery of hydrophobic small molecule chemotherapeutics paclitaxel (NP PTX) and camptothecin (NP CPT), and to evaluate *in vitro* effects on cell cycle, microtubule dynamics, cell death and proliferation. In order to study the effects of this drug combination on cell cycle, LLC cells were phase synchronized by serum starvation prior to treatment with monotherapy controls and dual drug combinations for 24 hrs (Figure 3.4A-C). Flow cytometry analysis of cell cycle showed the highest levels of G2/M phase arrest with sequential NP PTX → NP CPT treatment (67%), a 28% increase compared to simultaneous treatment, and 34% increase over the reverse sequential treatment NP CPT → NP PTX. Sequential NP PTX → NP CPT showed 13% increase compared to NP PTX and 26% increase over NP CPT monotherapy controls, and 52% increase over NP controls (Figure 3.4A-C). Interestingly, the highest levels of S phase arrest were seen with



simultaneous treatment, and among the lowest in the sequential NP PTX → NP CPT group, indicating the sequence of drug administration drove many more cells into G2/M phase arrest than would otherwise have occurred with the drug combination itself (Figure 3.4).

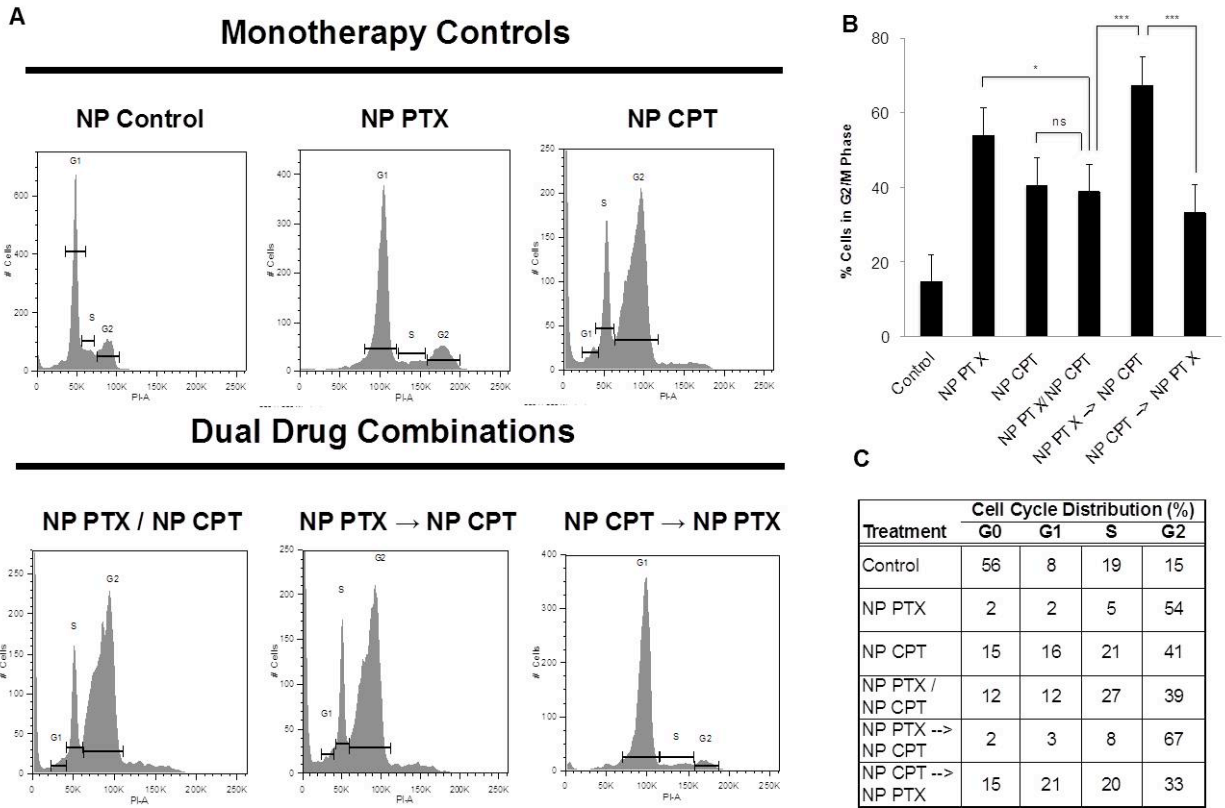


**Figure 3.4.** Flow cytometry histograms (A) representing cell cycle distributions of LLC cells treated with dual drug combinations (simultaneous NP PTX/NP CPT and sequential NP CPT→ NP PTX and NP PTX→ CPT) or monotherapy controls (NP Control, NP PTX and NP CPT). G2/M phase cell cycle arrest in response to monotherapy and dual drug combinations (B). Percentage of cells in all measured cell cycles: G0, G1, S and G2 phases after monotherapy and dual drug treatment (C).

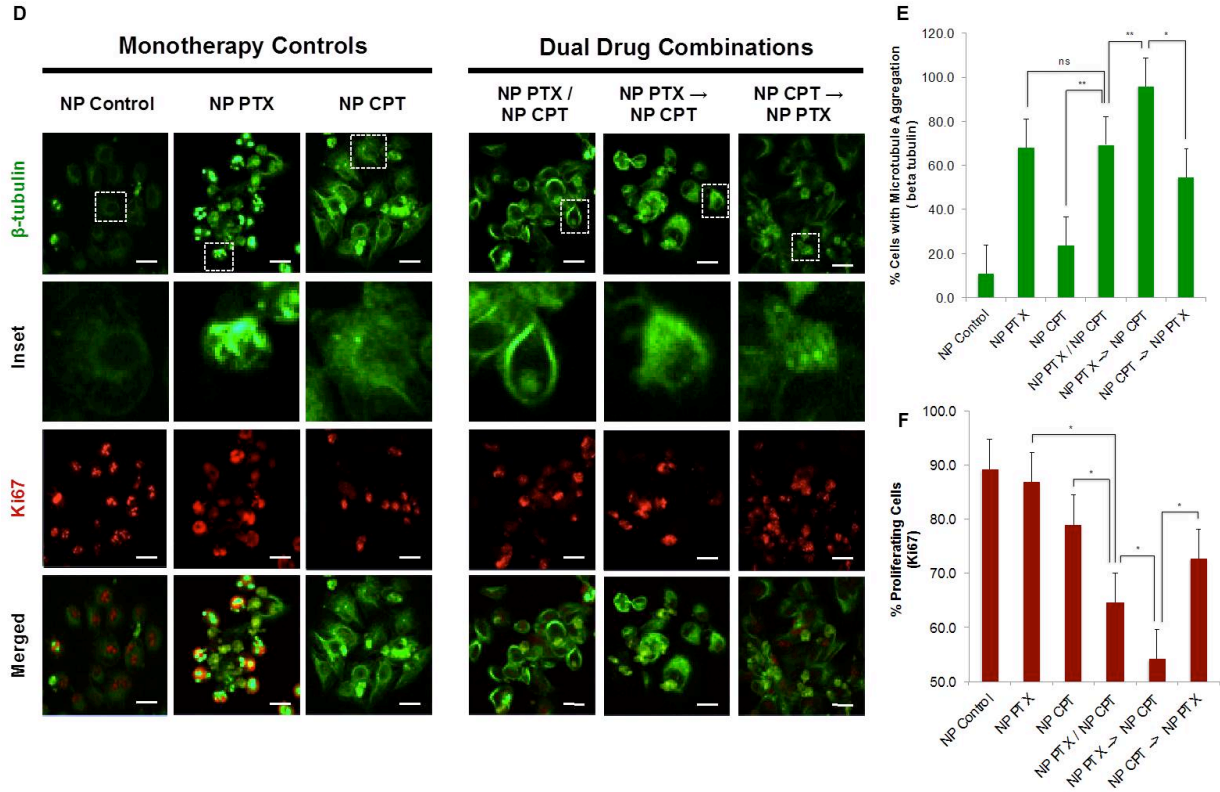


**Figure 3.4.** Confocal microscopy analysis of microtubule aggregation and cell proliferation in A549 lung carcinoma cells treated for 72 hrs at  $IC_{50}$  concentrations for each drug. Cells were fixed, stained for cellular beta tubulin (green) and Ki67 (red) in 63x magnification. Scale bar indicates 20  $\mu$ m (D). Percentage of dual drug treated cells vs. monotherapy controls exhibiting microtubule aggregation (green) (E), percentage of dual drug treated cells vs. monotherapy controls expressing Ki67, a marker for cellular proliferation (red) (F). Bars, mean and SE for  $n=3$ , unpaired Student's t test ( $p<0.05$ ).

Since microtubules and their associated proteins play a role in the cell cycle and help regulate mitosis, microtubule disrupting drugs such as paclitaxel can have multiple effects on cells.<sup>24,25</sup> Therefore, the effect of paclitaxel and camptothecin drug combinations on microtubule morphology in lung cancer cells was examined. Figure 3.4 shows confocal images of marked microtubule aggregation seen in all paclitaxel treatment groups compared to NP only controls. The greatest percentage of cells with morphological changes in microtubule structure can be seen with sequential NP PTX → NP CPT treatment, with 95.8% of cells exhibiting microtubule-induced ‘bundles’ compared to normal microtubule networks seen in NP controls (Figure 3.4). The reverse sequence showed only 54.5% of cells affected, and simultaneous treatment produced 69.4% of cells with microtubule changes (Figure 3.4). In comparison, NP PTX showed the greatest microtubule changes among the monotherapy controls with 67.9% of cells affected and NP CPT showed only 23.7% cells with affected microtubules (Figure 3.4E). Interestingly, the simultaneous dual drug combinations (NP PTX / NP CPT) primarily showed evidence of microtubule ‘bundles’, where NP PTX monotherapy controls showed microtubule ‘asters’ radiating from centrosomes (Figure 3.4D, insets). These morphological changes are consistent with cell cycle changes as mitotic asters generally appear in cells undergoing mitosis whereas bundling occurs more throughout G2 phase.<sup>24-27</sup> These results may indicate that addition of camptothecin contributes to cell cycle arrest and prevents entry into mitosis. Additionally, reorganization of microtubules into bundles may correlate with sensitivity of cells to camptothecin, with initial exposure to paclitaxel enhancing the sensitivity of lung cancer cells to the effects of camptothecin. Changes in cell proliferation can also be seen with the least number of cells proliferating (54.2%)

with sequential NP PTX → NP CPT treatment, compared to the reverse sequence at 72.7% and simultaneous treatment showing 62.9% proliferation. Monotherapy controls had the highest levels of proliferation with NP PTX showing 86.8% of cells still proliferating, NP CPT showing 71.1%, and NP controls with the highest population of cells proliferating at 89.2% (Figure 3.4F). In addition, sequential treatment with paclitaxel and camptothecin was also performed on PC-3 prostate cancer cells in order to observe changes in microtubule morphology (Figure 3.5). Results from these studies validate those observed in lung cancer cell lines, indicating that cells receiving the sequential treatment NP PTX → NP CPT showed the greatest level of microtubule polymerization compared to both monotherapy and reverse sequence controls.

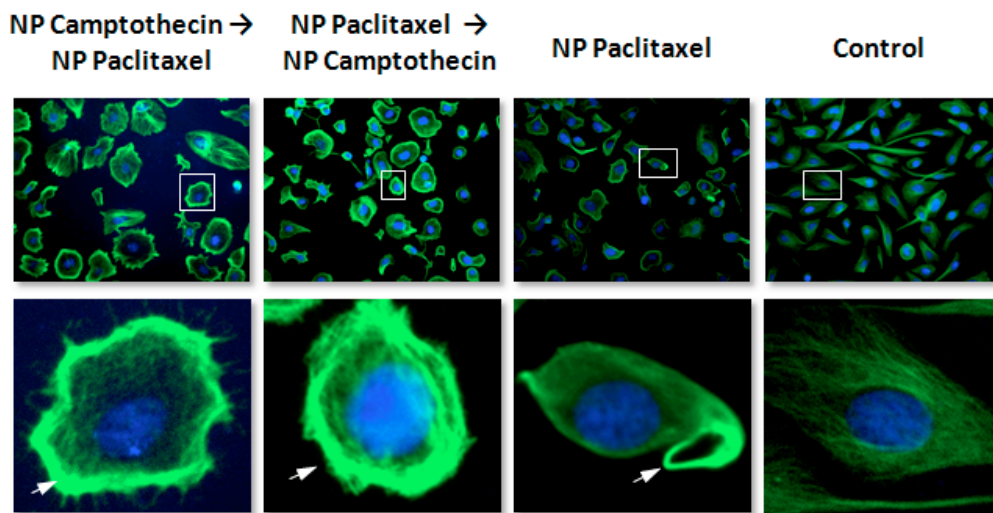


**Figure 3.5.** Sequential treatment with NP-paclitaxel before NP-camptothecin exhibited greater tubulin polymerization compared to the reverse sequence, NP-paclitaxel alone and untreated controls. PC-3 cells treated 24 hrs with NP camptothecin 12 hrs followed by NP-paclitaxel, and the reverse sequence of NP-paclitaxel then NP-camptothecin. Cells stained for tubulin polymerization (green) and nuclei counterstained with DAPI (blue). Fluorescence microscopy images obtained at 20x magnification.

In order to evaluate effects on cell death, LLC cells treated as described above were fixed and stained for caspase-3 expression, prior to analysis by flow cytometry. Figure 3.6 shows that cells receiving the sequential treatment NP PTX → NP CPT expressed the highest levels of caspase-3 protein, followed by the reverse sequence and NP PTX only, simultaneous NP PTX/NP CPT, NP CPT and NP controls.

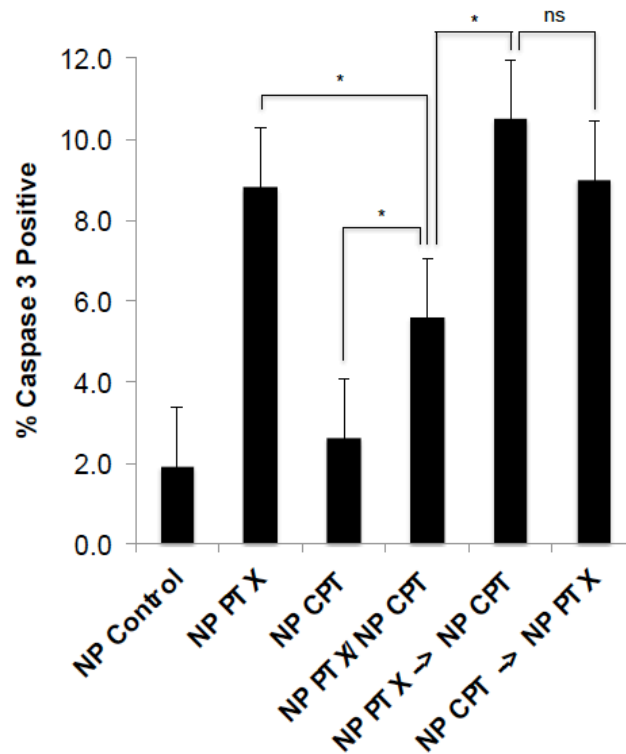


**Figure 3.6.** Flow cytometry analysis of caspase-dependent cell death in Lewis lung carcinoma cells treated for 72 hrs at  $IC_{50}$  concentrations for each drug. Cells were stained for presence of caspase-3 and analyzed by flow cytometry. Bars, mean and SE for  $n=3$ , unpaired Student's t test ( $p<0.05$ ).

## ***Conclusion***

This study investigated the feasibility of using nanosponge encapsulated paclitaxel and camptothecin to determine the optimum drug combination and sequence for treating lung cancer. Here, the role of drug combination and sequence *in vitro*, in both mouse and human lung cancer cell lines, was investigated using synthesized nanosponges loaded with either paclitaxel (NP PTX) or camptothecin (NP CPT). Results showed not only that paclitaxel and camptothecin combination therapy produced the greatest G2/M phase arrest compared to monotherapy, but also that sequential administration of NP PTX followed by NP CPT further enhanced caspase-dependent cell death compared to simultaneous administration. Paclitaxel, more so than camptothecin, was observed to drive cells into G2/M phase arrest and subsequent apoptosis. Further studies are necessary to determine the molecular basis for this effect in lung cancer. Sequential administration (NP PTX → NP CPT) of nanoparticle drug delivery systems resulted in greater cell death and decreased cell proliferation. Collectively, these studies suggest that dual combination treatment with administration of paclitaxel prior to camptothecin produces greater G2/M phase arrest, microtubule aggregation, cell death and reduced proliferation compared to simultaneous and monotherapy treatment. In addition, paclitaxel appears to show a ‘priming’ effect on the cells that enhances camptothecin’s effect on cells when given second.

## References

1. Chabner B.A., Roberts T.G. Timeline - Chemotherapy and the war on cancer. *Nat. Rev. Cancer* 2005, 65-72.
2. Hallahan D.E., Qu S.M., Geng L. et al. Radiation-mediated control of drug delivery. *Am. J. Clin. Oncol.* 2001, 24, 473-480.
3. Rosa D.D., Ismael G., Dal Lago L., Awada A. Molecular targeted therapies: lessons from years of clinical development. *Cancer Treat. Rev.* 2008, 34, 61-80.
4. Steichen S.D., Caldorera-Moore M., Peppas N.A. A review of current nanoparticle and targeting moieties for the delivery of cancer therapeutics. *Eur. J. Pharm. Sci.* 2013, 48, 416-427.
5. Wang A.Z., Langer R., Farokhzad O.C. Nanoparticle Delivery of Cancer Drugs. *Annu. Rev. Med.* 2012, 63, 185-198.
6. Park J.H., Lee S., Kim J.H., Park K., Kim K., Kwon I.C. Polymeric nanomedicine for cancer therapy. *Prog. Polym. Sci.* 2008, 33, 113-137.
7. van der Ende A.E., Kravitz E.J., Harth E. Approach to formation of multifunctional polyester particles in controlled nanoscopic dimensions. *J. Am. Chem. Soc.* 2008, 130, 8706-8713.
8. van der Ende A.E., Sathiyakumar V., Diaz R., Hallahan D.E., Harth E. Linear release nanoparticle devices for advanced targeted cancer therapies with increased efficacy. *Polym. Chem.* 2010, 1, 93-96.
9. van der Ende A., Croce T., Hamilton S., Sathiyakumar V., Harth E. Tailored polyester nanoparticles: post-modification with dendritic transporter and targeting units via reductive amination and thiol-ene chemistry. *Soft Matter* 2009, 5, 1417-1425.
10. Passarella R.J., Spratt D.E., van der Ende A.E., et al. Targeted nanoparticles that deliver a sustained, specific release of paclitaxel to irradiated tumors. *Cancer Res.* 2010, 70, 4550-4559.
11. Hallahan D.E., Geng L., Cmelak A.J., et al. Targeting drug delivery to radiation-induced neoantigens in tumor microvasculature. *J. Control Release.* 2001, 74, 183-191.
12. Han C.Z., Liu Z.M., Zhang X., Pogwizd S., He B. Noninvasive Three-Dimensional Cardiac Activation Imaging From Body Surface Potential Maps: A Computational and Experimental Study on a Rabbit Model. *IEEE Trans. Med. Imaging* 2008, 27, 1622-1630.

13. Hariri G., Yan H.P., Wang H.L., Han Z.Z., Hallahan D.E. Radiation-guided drug delivery to mouse models of lung cancer. *Clin. Cancer Res.* 2010, 16, 4968–4977.
14. Wang H.L., Yan H.P., Fu A., Han M.J., Hallahan D., Han Z.Z. TIP-1 translocation onto the cell plasma membrane is a molecular biomarker of tumor response to ionizing radiation. *PLoS One* 2010, 5(8), e12051.
15. Weigel T.L., Lotze M.T., Kim P.K., Amoscato A.A., Luketich J.D., Odoux C. Paclitaxel-induced apoptosis in non-small cell lung cancer cell lines is associated with increased caspase-3 activity. *J. Thorac. Cardiovasc. Surg.* 2000, 119, 795-803.
16. Joung Y.K., Park K.D. Controlled release systems of growth factors using heparinized polymeric carriers. *Tissue Eng. Regener. Med.* 2008, 5, 156-164.
17. Pommier Y. Drugging topoisomerases: lessons and challenges. *ACS Chem. Biol.* 2013, 8, 82-95.
18. Pommier Y., Leo E., Zhang H.L., Marchand C. DNA topoisomerases and their poisoning by anticancer and antibacterial drugs. *Chem. Biol.* 2010, 17, 421-433.
19. Pommier Y. DNA topoisomerase I inhibitors: chemistry, biology, and interfacial inhibition. *Chem. Rev.* 2009, 109, 2894-2902.
20. Pommier Y. Topoisomerase I inhibitors: camptothecins and beyond. *Nat. Rev. Cancer* 2006, 6, 789-802.
21. Kerbel R.S., Kamen B.A. The anti-angiogenic basis of metronomic chemotherapy. *Nat. Rev.* 2004, 4, 423-436.
22. Yurkovetskiy A.V., Fram R.J. XMT-1001, a novel polymeric camptothecin pro-drug in clinical development for patients with advanced cancer. *Adv. Drug Delivery Rev.* 2009, 61, 1193-1202.
23. Mu L., Elbayoumi T.A., Torchilin V.P. Mixed micelles made of poly(ethylene glycol)-phosphatidylethanolamine conjugate and D-alpha-tocopheryl polyethylene glycol 1000 succinate as pharmaceutical nanocarriers for camptothecin. *Int. J. Pharm.* 2005, 306, 142-149.
24. Rusan N.M., Fagerstrom C.J., Yvon A.M.C. and Wadsworth P. Cell cycle-dependent changes in microtubule dynamics in living cells expressing green fluorescent protein-alpha tubulin. *Mol. Biol. Cell* 2001, 12, 971-980.
25. Hughes J.R., Meireles A.M., Fisher K.H., et al. A microtubule interactome: Complexes with roles in cell cycle and mitosis. *PloS Biol.* 2008, 6, 785-795.



26. Roberts J.R., Rowinsky E.K., Donehower R.C., Robertson J. and Allison D.C. Demonstration of the cell-cycle positions of Taxol-induced asters and bundles by sequential measurements of tubulin immunofluorescence, DNA content, and autoradiographic labeling of Taxol-sensitive and Taxol-resistant cells. *J. Histochem. Cytochem.* 1989, 37, 1659-1665.
27. Gan P.P., McCarroll J.A., Po'uha S.T., Kamath K., Jordan M.A. and Kavallaris M. Microtubule dynamics, mitotic arrest, and apoptosis: drug-induced differential effects of beta III-tubulin. *Mol. Cancer Ther.* 2010, 9, 1339-1348.
28. Wang H., Fu A., Han Z. and Hallahan D. Tax interacting protein (TIP-1): A potential radiation inducible receptor within cancer. *Int. J. Radiat. Oncol.* 2007, 69, S590-S591.
29. Neri D. and Bicknell R. Tumour vascular targeting. *Nat. Rev. Cancer* 2005, 5, 436-446.
30. Pasquier E., Kavallaris M. and Andre N. Metronomic chemotherapy: new rationale for new directions. *Nat. Rev. Clin. Oncol.* 2010, 7, 455-465.
31. Malumbres M. and Barbacid M. Cell cycle, CDKs and cancer: a changing paradigm. *Nat. Rev. Cancer.* 2009, 9, 153-164.
32. Jordan M.A., Wilson L. Microtubules as a target for anticancer drugs. *Nat. Rev. Cancer.* 2004, 4, 253-265.
33. Yamada K., Ikehara M., Tanaka G., Nomura I., Oshita F., Noda K. Dose escalation study of paclitaxel in combination with fixed-dose irinotecan in patients with advanced non-small cell lung cancer (JCOG 9807). *Oncology.* 2004, 66, 94-100.
34. Zhang L., Hu Y., Jiang X., Yang C., Lu W., Yang Y.H. Camptothecin derivative-loaded poly(caprolactone-co-lactide)-b-PEG-b-poly(caprolactone-co-lactide) nanoparticles and their biodistribution in mice. *J. Controlled Release.* 2004, 96, 135-148.
35. Pei X.H., Nakanishi Y, Takayama K., Bai F., Kawasaki M., Tsuruta N., Mizuno K. and Hara N. Effect of CPT-11 in combination with other anticancer agents in lung cancer cells. *Anticancer Drugs.* 1997, 8(3), 231-237.
36. Kaczirek K., Schindl M., Weinhausel A., et al. Cytotoxic activity of camptothecin and paclitaxel in newly established continuous human medullary thyroid carcinoma cell lines. *J. Clin. Endocrinology and Metabolism.* 2004, 89(5), 2397-2401.

37. Fukuoka M., Niitani H., Suzuki A., Motomiya M., et al. A phase II study of CPT-11, a new derivative of camptothecin, for previously untreated non-small-cell lung cancer. *J. Clin. Oncology*. 1992, 10(1), 16-20.
38. Galimberti F., Thompson S.L., Liu X., Li H., et al. Targeting the cyclin E-Cdk-2 complex represses lung cancer growth by triggering anaphase catastrophe. *Clin. Cancer Res.* 2010, 16, 109-120.
39. Aldoss I.T., Tashi T. and Ganti A.K. Seliciclib in malignancies. *Expert Opin. Investi. Drugs*. 2009, 18(12), 1957-65.
40. Sanderowicz A.M. Small-molecule cyclin-dependent kinase modulators. *Oncogene*. 2003, 22(42), 6609-20.

## CHAPTER 4

### SYNTHESIS AND BIOLOGICAL EVALUATION OF CYCLIC RGDEKf-Ahx-C FUNCTIONALIZED NANOSPONGES FOR IN VITRO TUMOR TARGETING AND IMAGING IN A LUNG CANCER MODEL

#### ***Abstract***

Integrins are an important target for many chemotherapeutic treatments, and RGD targeted nanoparticles have the potential to deliver various imaging and therapeutic agents to the  $\alpha_v\beta_3$  integrin expressing tumor vasculature. Development of RGD probes for tumor imaging has created the need for greater affinity and stability of these ligands *in vivo*. Cyclic RGD peptides exhibit enhanced stability and decreased susceptibility to chemical and enzymatic degradation compared to their linear counterparts. In this study we synthesized a cyclic RGD peptide of the sequence RGDEKf-Ahx-C as a targeting ligand for tumor-specific targeting of nanoparticles to lung cancer cells *in vitro*. This cyclic RGD tumor targeting peptide was synthesized using solid phase peptide synthesis, attached to nanoparticles, and modified with a fluorescent probe for *in vitro* cell imaging applications. Confocal microscopy showed competitive binding of cyclic RGD targeted nanoparticles compared to untargeted controls and competitive binding vitronectin controls. These results indicate that this cyclic RGD peptide binds specifically in a dose responsive way to the  $\alpha_v\beta_3$  integrin receptor present on lung cancer cells *in vitro*, and can be used to target nanoparticles specifically to this receptor on cancer cells.

## ***Introduction***

### *Integrins as therapeutic targets*

Integrins are heterodimeric glycoproteins that mediate cellular adhesion to other cells and extracellular matrix.<sup>1</sup> They also function as receptors by binding to ligands with exposed arginine-glycine-aspartate (RGD) sequences.<sup>2</sup> These receptors interact with extracellular ligands and stimulate intracellular signaling and gene expression in various cellular processes. They also play a role in invasion and metastasis of cancer cells, tumor growth and angiogenesis.<sup>1-6</sup> As a result, integrins have become an attractive target for many chemotherapeutic treatments, and the development of RGD peptide ligands that could bind to these integrin receptors has been a rich source of potential tumor targeting agents.

### *RGD peptide ligands*

The Arg-Gly-Asp (RGD) amino acid sequence was found to be a binding ligand to the  $\alpha_v\beta_3$  integrin in the early 1970s by Ruoslahti and colleagues.<sup>8-12</sup> It was originally identified as a cell binding site in the extracellular matrix protein fibronectin, but later on this sequence was recognized as the amino acid motif present in many natural ligands binding the  $\alpha_v\beta_3$  receptor, including fibrinogen, fibronectin, and vitronectin.<sup>8-12</sup> Proteins that contain an RGD binding motif, along with their integrin receptors, are a major recognition system for cell adhesion processes. The integrin-binding activity of adhesion proteins can be reproduced by short synthetic peptides containing the RGD sequence. The diverse applications for these peptides include inhibiting angiogenesis and tumor

formation, coating surfaces for use as biomaterials, enhancing drug delivery systems, and imaging for diagnostic purposes.<sup>3-5</sup>

### *Linear vs. Cyclic RGD peptides*

Development of RGD probes for tumor imaging has created the need for greater affinity and stability of these ligands *in vivo*.<sup>22-25</sup> As a result, differences in conformation and structure have been studied between many linear and cyclized forms of different RGD containing peptides to determine the most stable conformation. Optimization of peptide length and spatial orientation has led to the development of cyclic RGD peptides that more closely mimic naturally occurring proteins that bind the  $\alpha_v\beta_3$  integrin receptor.<sup>8</sup> It has been demonstrated that cyclization of these RGD peptides enhances stability and decreases susceptibility to chemical and enzymatic degradation, partly because of the increased conformational stability of the cyclic peptide compared to the linear peptide.<sup>14,19</sup> One of these cyclic peptides, cyclo(RGDf(NMe)V) (Cilengitide) has been used to treat glioblastoma in clinical trials.<sup>18-24</sup> Another way to improve affinity is to increase the number of molecules available for binding (multivalency) via nanoparticles.<sup>13,20,21</sup> This binding strategy exploits the surface of nanoparticles as a platform for peptide ligand attachment, and is an effective way for obtaining high affinity molecular binding.<sup>20,21</sup>

### *Synthesis and optimization of RGD peptides*

Optimization of solid-phase peptide synthesis requires the use of coupling reagents best suited to the formation of peptide bonds. Typical peptide synthesis methods

use a benzotriazole (such as HOBt and its derivatives) in combination with carbodiimides, or immonium (HBTU) and phosphonium (PyBOP) salts.<sup>15,16</sup> More recently, a uronium salt (COMU) has been shown to have greater coupling efficiency and lower racemization than its predecessors, making it a superior reagent for the formation of an amide bond.<sup>15,16</sup> In addition, shorter coupling reaction times and higher purity peptides make COMU a suitable choice for synthesis of cyclic peptides.<sup>15,16</sup>

### *Integrin targeted tumor imaging*

To reach tumor cells and tumor-associated parenchymal cells, drugs must cross the vascular barrier and penetrate into the stroma. Cancer tissue is heterogeneous, with vast differences in tumor structure and physiology. These features translate into steep drug gradients and variability in the uptake and distribution of anti-cancer drugs.<sup>7</sup> Although cancer cells are inherently more vulnerable to chemotherapy than the majority of normal cells, most chemotherapy drugs are not very selective and can harm normal tissues as well. Because of the particular characteristics of the tumor microenvironment and tumor angiogenesis, it is possible to design drug delivery systems that specifically bring chemotherapy drugs to tumors. Nanometer-sized drug delivery systems can target tumors by a passive or active process. Active targeting involves drug delivery to a specific site based on molecular recognition, providing the greatest efficiency for cancer chemotherapy.<sup>5</sup> One approach is to conjugate a ligand that can interact with a receptor at the target cell site to a nanoparticle. The angiogenic phenotype of the tumor vasculature, and some proteins or receptors expressed at the surface of the endothelial cells are considered attractive targets for delivering nanoparticles to tumors. The most popular

example is the integrin adhesion molecule  $\alpha_v\beta_3$ . The  $\alpha_v$  integrin subunit is highly expressed on endothelial cells lining tumors, whereas it is poorly expressed in healthy endothelial cells. Targeting the  $\alpha_v\beta_3$  integrin with drugs may thus provide an opportunity to destroy tumor vessels but keep vessels from normal tissues intact. However, the use of complicated modification techniques and the poor conjugation efficiency of the targeting ligands have limited the application of most of the nano-sized drug delivery systems.<sup>8</sup>

Peptides based on mentioned the RGD sequence have been used extensively as tumor targeting ligands in diagnostics and therapeutics, as they bind preferentially to  $\alpha_v\beta_3$  integrins. RGD-targeted nanocarriers have the potential to deliver various therapeutic agents to the  $\alpha_v\beta_3$ -expressing tumor vasculature. Since the integrins are specifically over-expressed at the surface of tumor cells and angiogenic endothelial cells at the tumor site, RGD-mediated drug delivery generally leads to high levels of accumulation in tumor tissues compared to unmodified drug or non-targeted drug delivery systems. Both linear RGD and cyclic RGD have been applied for targeted delivery of drugs, genes and polymers. Furthermore, there are studies showing that cyclic RGD peptides are more stable than their linear precursors.<sup>14,19</sup> The increase in stability of the cyclic peptide compared with the linear peptide is due to decreased structural flexibility imposed by the ring.<sup>12</sup> In this study we synthesized a cyclic RGD peptide of the sequence RGDEKf-Ahx-C as a targeting ligand for tumor-specific targeting of nanoparticles to lung cancer cells *in vitro*.

## Experimental

### *Materials and Methods*

#### *Materials*

Chemical reagents were purchased from Sigma-Aldrich and Strem Chemicals, chemotherapeutic drugs from LC Laboratories. Spectra/Por Dialysis membrane (MWCO=10,000) in 0.05% sodium azide was purchased from Spectrum Laboratories.

#### *Preparation of Monomers*

##### *$\delta$ -valerolactone monomer (VL)*

Technical grade  $\delta$ -valerolactone was Kugelrohr distilled to produce a colorless liquid product.

##### *$\alpha$ -allyl- $\delta$ -valerolactone monomer (AVL)*

A flame dried 500 mL two-necked round bottom flask was equipped with a stir bar, sealed with a rubber septum, and purged with nitrogen for 30 min. To the flask, 156.25 mL of anhydrous THF was added and cooled to -78 °C in a dry ice/acetone bath. Following this, a basic solution of lithium diisopropylamine was produced by adding redistilled n,n-diisopropylamine (3.3 mL, 23.63 mmol) and n-butyl lithium (2.5 M in hexanes) (9.35 mL, 23.38 mmol) dropwise via syringe. This solution was stirred for 20 minutes. A nitrogen purged solution of distilled  $\delta$ -valerolactone (1.97 mL, 21.23 mmol) in anhydrous THF (56 mL) was then added dropwise via syringe over 30 min. After an additional 30 min of stirring, a nitrogen purged solution of allyl bromide (2.21 mL, 25.54 mmol) in hexamethylphosphoramide (4.43 mL, 25.46 mmol) was added via syringe. The reaction mixture was warmed up to -40 °C and stirred for 2 hrs. The reaction was quenched with excess NH<sub>4</sub>Cl solution. The crude product was concentrated via rotary



evaporator, washed three times with saturated NaCl solution, and dried with anhydrous magnesium sulfate. The crude product was purified via column chromatography (Biotage Isolera), analyzed by thin layer chromatography and Kugelrohr distilled. Chromatography with a gradient of 5-20% ethyl acetate in n-hexanes as eluent gave a yellow liquid product. Kugelrohr distillation produced a colorless liquid product. Yield: 3.56 g (89%).  $^1\text{H}$  NMR (400 MHz,  $\text{CDCl}_3/\text{TMS}$ , ppm)  $\delta$ : 5.7 (m, 1H,  $\text{H}_2\text{C}=\text{CH}-$ ), 5.08 (m, 2H,  $\text{H}_2\text{C}=\text{CH}-$ ), 4.28 (m, 2H,  $-\text{C}(\text{O})\text{OCH}_2-$ ), 2.53-2.58 (m, 2H,  $\text{H}_2\text{C}=\text{CHCH}_2-$ ), 2.27 (m, 1H,  $\text{H}_2\text{C}=\text{CHCH}_2\text{CH}-$ ), 2.06 (m, 1H,  $\text{H}_2\text{C}=\text{CHCH}_2\text{CHCH}_2-$ ), 1.89 (m, 2H,  $\text{C}(\text{O})\text{OCH}_2\text{CH}_2-$ ), 1.55 (m, 1H,  $\text{H}_2\text{C}=\text{CHCH}_2\text{CHCH}_2-$ ).

#### *Preparation of Linear Polymer Precursors*

##### *Poly(VL-co-AVL)*

A flame dried 25 mL 3-necked round bottom flask was equipped with a stir bar, sealed with rubber septa and nitrogen purged. A stock solution of anhydrous ethanol in anhydrous tetrahydrofuran was prepared (1.7 M) in a 50 mL flame dried round and nitrogen purged round bottom flask, and a stock solution of  $\text{Sn}(\text{OTf})_2$  catalyst in anhydrous tetrahydrofuran was prepared ( $3.7 \times 10^{-2}$  M) in a 10 mL flame dried and nitrogen purged round bottom flask. Ethanol (584  $\mu\text{L}$ , 1.0 mmol) and  $\text{Sn}(\text{OTf})_2$  (261  $\mu\text{L}$ ,  $9.64 \times 10^{-6}$  mol) were added via syringe to the 25 mL 3-neck round bottom flask and the catalyst/initiator solution was allowed to stir at room temperature for 30 minutes prior to simultaneous addition of  $\delta$ -valerolactone (2.22 g, 22.0 mmol) and  $\alpha$ -allyl(valerolactone) (0.777 g, 5.548 mmol) monomers via syringe. After addition of both monomers, the reaction was stirred for 24h at room temperature. The resulting polymer was diluted with 1 mL anhydrous THF and purified by dropwise addition into 1 L of chilled methanol to

remove any remaining monomer and catalyst. The methanol was decanted and the precipitate redissolved in methylene chloride, rotary evaporated and dried *in vacuo*. The resulting polymer was observed as a waxy white solid.  $M_w = 3000$  Da; PDI = 1.09;  $^1\text{H}$  NMR (400 MHz,  $\text{CDCl}_3/\text{TMS}$ , ppm)  $\delta$ : 5.72 (m,  $\text{H}_2\text{C}=\text{CH}-$ ), 5.04 (m,  $\text{H}_2\text{C}=\text{CH}-$ ), 4.08 (m,  $-\text{CH}_2-\text{O}-$ ), 3.64 (m,  $\text{CH}_3\text{CH}_2\text{O}-$ ), 2.34 (m, vl,  $-\text{CH}_2\text{CH}_2\text{C}(\text{O})\text{O}-$ , avl,  $\text{H}_2\text{C}=\text{CHCH}_2\text{CH}$ ,  $\text{H}_2\text{C}=\text{CHCH}_2\text{CH}-$ ), 1.68 (m, avl and vl,  $-\text{CHCH}_2\text{CH}_2-$ ), 1.26 (t,  $\text{CH}_3\text{CH}_2\text{O}-$ ).

#### *Poly(VL-co-AVL-co-EVL)*

In a 100 mL round bottom flask, equipped with stir bar and rubber septum, a solution of poly(VL-co-AVL) (1.0 g,  $1.55 \times 10^{-3}$  mol) was dissolved in 8.5 mL of methylene chloride. To this solution, meta-chloroperoxybenzoic acid (121.25 mg,  $7.03 \times 10^{-4}$  mol) was added. The solution was stirred for 24 hrs at room temperature and then concentrated via rotary evaporator. The crude product was dissolved in a minimal amount of dichloromethane (2 mL) and precipitated into an Erlenmeyer flask containing 500 mL cold diethyl ether. The solution was decanted, and the white solid was rotary evaporated and dried *in vacuo* to obtain the final white waxy polymer. Yield: 0.768 g (76.8%).  $^1\text{H}$  NMR (400 MHz,  $\text{CDCl}_3/\text{TMS}$ , ppm)  $\delta$ : Decrease in allylic protons at 5.7 and 5.09 ppm and the appearance of small broad resonance peaks at 2.96, 2.75 and 2.47 ppm due to the formation of the epoxide.

#### *Formation of nanoparticles*

In a 250 mL round bottom flask equipped with stir bar and reflux condenser, a solution of 2,2'-(ethylenedioxy)diethylamine (10.5  $\mu\text{L}$ ,  $7.18 \times 10^{-5}$  mol) in 29.55 mL methylene chloride was heated at 45 °C. A solution of poly(VL-co-AVL-co-EVL), (0.200 g,  $M_w = 3000$  Da) dissolved in methylene chloride was added. The mixture was refluxed at 45 °C

for 12 h. Residual diamine crosslinker was removed via dialysis against methylene chloride with Spectra/Por Dialysis Tubing (MWCO =10,000).  $^1\text{H}$  NMR (400 MHz,  $\text{CDCl}_3/\text{TMS}$ , ppm)  $\delta$ : Decrease in number of epoxide protons at 2.96, 2.75 and 2.47 ppm and the appearance of signals at 3.5 and 2.89 ppm corresponding to the protons near the secondary amine of the diamine crosslinker after the reaction.

### *Peptide Targeted Nanoparticles*

#### *Addition of targeting peptide via photoinitiated thiol-ene 'click' reaction*

Poly(VL-co-AVL-co-EVL) nanosponges were dissolved in dichloromethane and purified using Sephadex column chromatography, rotary evaporated and dried *in vacuo*. Anhydrous, degassed DMSO (1 mL) was used to dissolve 20 mg of poly(VL-co-AVL-co-EVL) nanosponges, 10 mg of cRGD peptide and 1 mg DMPA. Mixture was stirred for 2 days in an oil bath at 37 °C under ultraviolet light at 365 nm. The product was purified by dialysis (MWCO 10,000) against methanol/acetonitrile (1:1) for 2 days, rotary evaporated and dried *in vacuo*.

#### *Quantification of peptide units on nanoparticles via $^1\text{H}$ NMR:*

Since the primary thiol functional group from the cysteine residue in the peptide (RGDEKf-Ahx-C) reacts with the allyl groups in the nanoparticle in a 1:1 stoichiometry, the allyl groups that are consumed in the reaction directly correlate with how many peptides are bound to the nanoparticle. By comparing the percent allyl groups in the nanoparticle before and after peptide attachment, the difference can be used to calculate the number of bound peptides. The nanoparticle peak at 4.08 ppm is used as an internal standard for determining the number of unmodified allyl groups remaining after the photoinitiated thiol-ene click reaction for peptide attachment.

*Modification of RGDEKf-Ahx-C-NPs for confocal imaging with NHS Alexa Fluor 488*

RGDEKf-Ahx-C modified poly(VL-co-AVL-co-EVL) nanosponges and unmodified nanoparticles were separately dissolved in anhydrous DMSO. To each solution, NHS Alexa Fluor 488 was added and the resulting mixture was stirred for 6 hrs (covered in foil to protect from light). The product was purified by dialysis (MWCO =10,000) against methanol/acetonitrile (1:1) overnight, rotary evaporated and dried *in vacuo* (covered in foil to protect from light).

*Solid Phase Peptide Synthesis of RGDEKf-Ahx-C peptide*

All Amino acids used were protected by 9-fluoromethoxycarbonyl (Fmoc) and were purchased from Advanced ChemTech (Louisville, KY). They included Fmoc-L-Glu(ODmab)-OH, Fmoc-L-Asp(OtBu)-OH, Fmoc-L-Gly-OH, Fmoc-L-Arg(Pbf)-OH, Fmoc-L-Lys(Boc)-OH, Fmoc-D-Phe-OH, and Fmoc-epsilon-Ahx-OH spacer. An Fmoc-Cys(Trt)-2-Cl-Trt resin was purchased from AAPPTec (Louisville, KY). (1-Cyano-2-ethoxy-2-oxoethylideneaminoxy)dimethylamino-morpholino-carbenium hexafluorophosphate (COMU), N,N-Diisopropylethylamine (DIPEA), trifluoroacetic acid (TFA), N,N-dimethylformamide (DMF), dichloromethane (DCM) and piperidine were purchased from Sigma Aldrich (St. Louis, MO). HPLC grade acetonitrile (ACN) and methanol (MeOH) were obtained from Sigma Aldrich (St. Louis, MO). All chemicals were of reagent grade and used as received. HPLC purification of crude peptide was performed on a reverse phase column which was eluted with CH<sub>3</sub>CN in 0.1% aqueous TFA and detected at OD 220 nm.

### *Synthesis of cyclic peptides*

Cyclic RGDEKf-Ahx-C was synthesized on the resin via solid-phase peptide synthesis methodology using Fmoc strategy, and cyclized in the solvent. The synthesis route could be seen in Scheme S1. Briefly, a swelling resin, and further elongation led to a linear protected peptide. In each elongation step, coupling was performed with a 2-fold excess of Fmoc-amino acid in the presence of COMU/DIPEA mixed solution for 30 min, and Fmoc groups were cleaved with 20% (v/v) piperidine in DMF for 10 min. After cleavage from resin by 5% TFA/DCM for 2 h, the linear protected peptides were cyclized in the solvent by COMU/DIPEA for 2 h. The crude product was yielded after all the protecting groups were removed by using 95% TFA/H<sub>2</sub>O for 2 hrs. The crude cyclic peptides were further purified by preparative reversed-phase high performance liquid chromatography (RP-HPLC).

### *NMR Analysis*

The <sup>1</sup>H NMR spectra were obtained on a 600 MHz (Bruker) spectrometer with DMSO-d<sub>6</sub> and TMS as an internal standard.

### *Cell Culture*

Human lung carcinoma (A549) cells were purchased from American Type Culture Collection (ATCC; Manassas, VA). Cells were cultured at 37 °C in a 5% CO<sub>2</sub> atmosphere in Dulbecco's modified Eagle's medium (DMEM, Gibco) supplemented with 10% fetal bovine serum (FBS, Gibco), penicillin antibiotic and streptomycin antimycotic. All cultures maintained at 37°C in incubator with 95% humidity and 5% CO<sub>2</sub>.

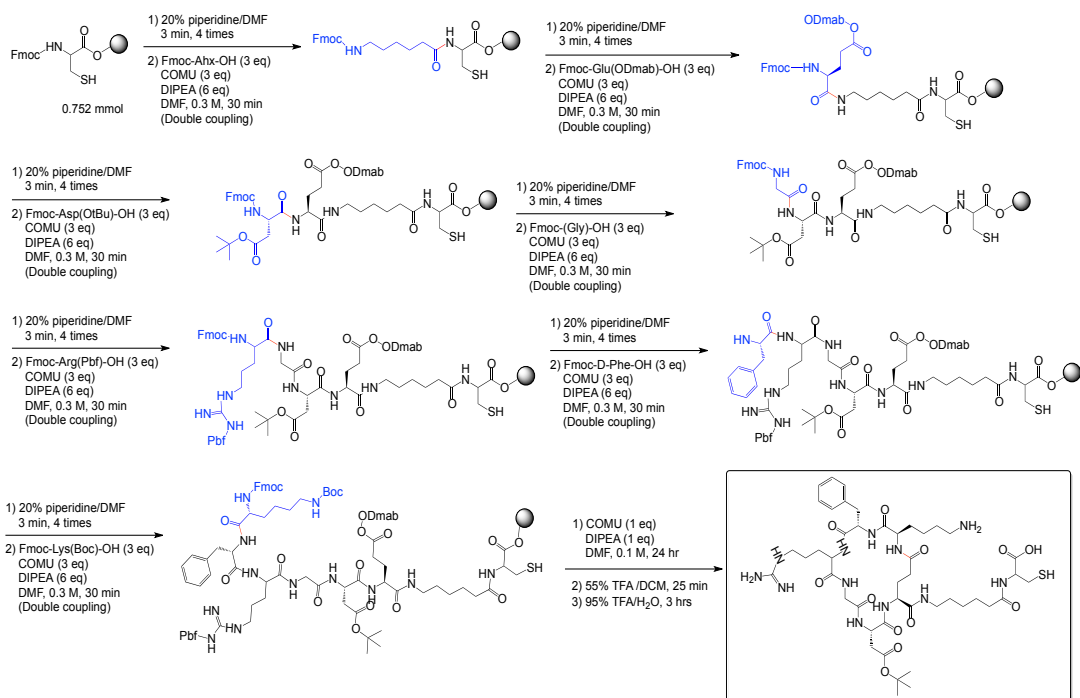
### *Cell Imaging*

Human A549 lung carcinoma cells were grown on cover slips and treated with synthesized cRGD-NP, untargeted NP controls, or blocked with 1 mg/ml Vitronectin for 1 hr. All groups were washed twice with PBS and fixed with 4% paraformaldehyde. Cells were fixed and visualized by confocal microscopy. *In vitro* imaging was performed using a Zeiss LSM 710 Meta Inverted confocal microscope at 63x magnification. Images were acquired from three fields of view. Bar graph shows percent fluorescent intensity. All images were analyzed using MetaMorph and ZEN image acquisition and analysis software.

### ***Results and discussion***

Cyclic RGD peptide was prepared by solid-phase peptide synthesis methods (Scheme 4.1). In order to synthesize linear and cyclic RGDEKf-Ahx-C peptides, Merrifield solid-phase peptide synthesis (SPPS) methods were used along with Fmoc/tBu chemistry.<sup>17</sup> An N-protected C-terminal cysteine was anchored via its carboxyl group to a polystyrene resin (Scheme 4.1). The peptide sequence was then built linearly from the C-terminus to the N-terminus using repeated cycles of deprotection and amino acid coupling reactions.<sup>17</sup> The linear peptide was then cleaved from the resin and any remaining protecting groups removed.<sup>17</sup> The cyclic peptide was cyclized on the resin prior to cleavage and removal of remaining protecting groups. The base-labile N-Fmoc group was used to protect the amino functional groups on each amino acid as well as acid-labile side-chain protecting groups.<sup>17</sup> An ODmab protecting group was used to protect the glutamic acid carboxyl group, prior to being removed with 2% hydrazine in DMF (Scheme 4.1). The ODmab protection of the carboxyl groups is compatible with the

Fmoc strategy as it is stable in piperidine used for peptide synthesis.<sup>18</sup> Removal of the ODmab group left a deprotected carboxylic acid group available for the final cyclization reaction.



**Scheme 4.1.** Solid-phase peptide synthesis and structure of cyclic RGDEKf-Ahx-C.

Nanosponges of 50-100 nm size were prepared from poly(VL-co-AVL-co-EVL) polymers, and functionalized with cyclic RGDEKf-Ahx-C peptide using thiol-ene ‘click’ chemistry. The primary thiol functional group from the cysteine residue was reacted with allyl functional groups from the nanosponge in a photoinitiated thiol-ene ‘click’ reaction (Figure 4.1). The photoinitiator 2,2-dimethoxy-2-phenylacetophenone (DMPA) was used in catalytic amounts to initiate a radical reaction in the presence of ultraviolet light (365

nm).<sup>33,34</sup> Upon absorption of light, DMPA undergoes a homolytic bond cleavage to produce two new radicals.<sup>33,34</sup> These radical species initiate the thiol-ene reaction by attacking the R-SH bond and generating a new sulfenyl radical that propagates the reaction by adding to an alkene to form a new carbon radical.<sup>33,34</sup> Since this typically occurs on the least substituted carbon of the alkene (due to greater stability of the radical intermediate formed), the reaction is said to exhibit anti-Markovnikov regioselectivity. This new carbon radical further propagates the reaction by reacting with another thiol to generate another sulfenyl radical, repeating the cycle.<sup>33,34</sup> The reaction terminates when two of these sulfenyl or carbon radicals meet and react to form a new bond.<sup>33,34</sup>

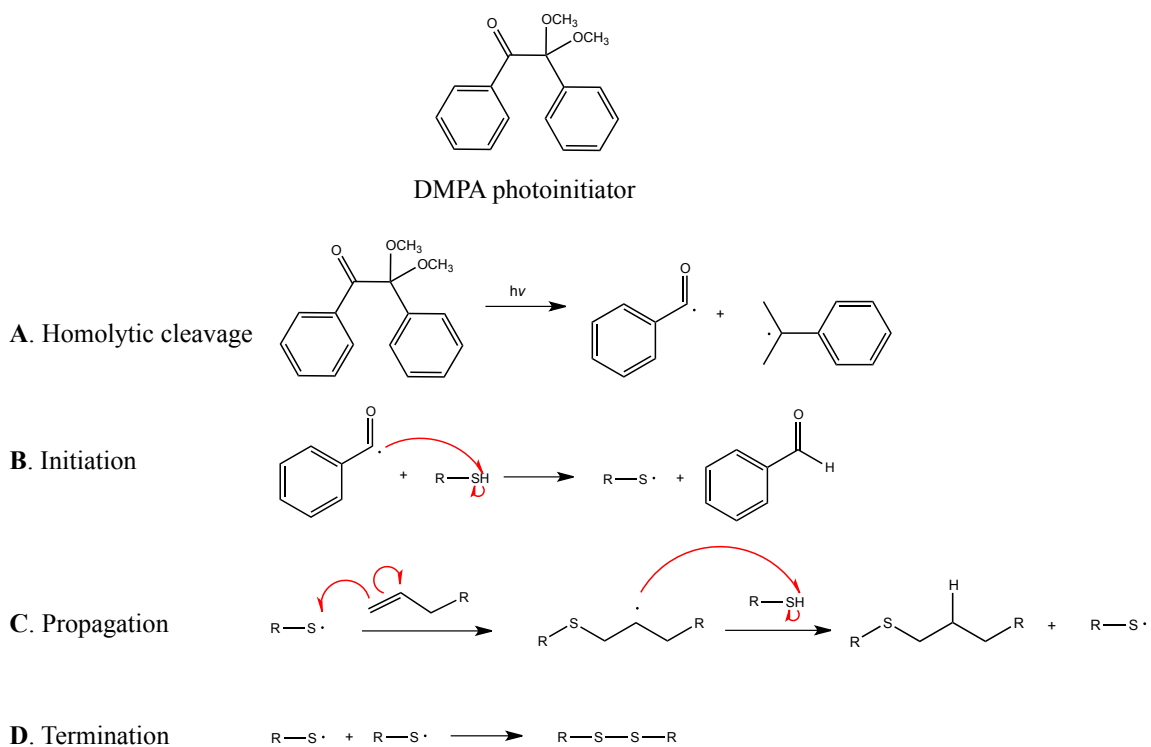


**Figure 4.1.** Thiol-ene ‘click’ reaction using DMPA photoinitiator. (A) DMPA absorbs light and undergoes homolytic bond cleavage producing new radicals. (B) Initiation of thiol-ene ‘click’ reaction and generation of sulfenyl radical (C) Propagation of reaction with sulfenyl and carbon radicals. (D) Termination of reaction when two radicals meet and form a new bond.



RGD peptides have been shown to bind to integrins present on cancer cells. Nanosponges of 50-100 nm size were modified with these peptides using DMPA photoinitiated thiol-ene ‘click’ reactions to produce peptide functionalized nanosponges (Figure 4.1). These modified nanosponges were then analyzed by  $^1\text{H}$  NMR to confirm peptide conjugation (Figure 4.2), prior to further functionalization with fluorescent imaging units including Alexa fluor 488 for *in vitro* studies.

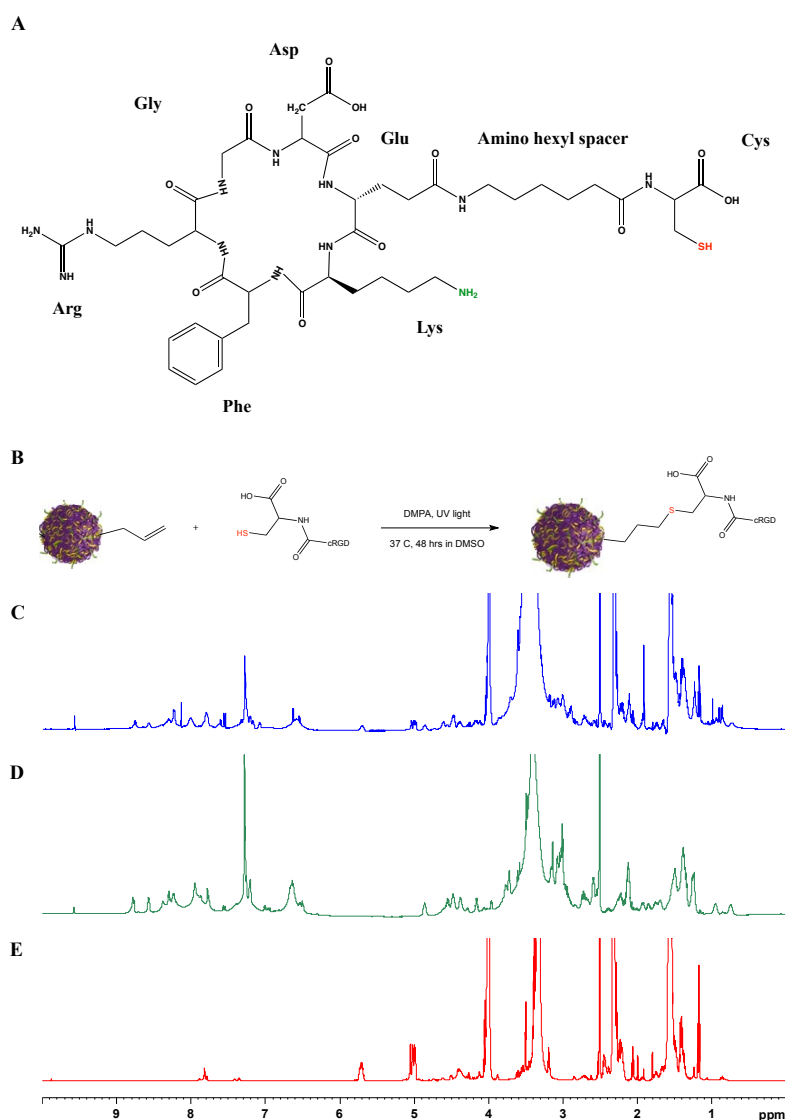


**Figure 4.2.** Photoinitiated thiol-ene ‘click’ attachment of cyclic RGD to nanosponges. (A) Cyclic RGDEKf-Ahx-C peptide, (B) Reaction scheme,  $^1\text{H}$  NMR (600 MHz) spectra (C) cyclic RGD-NP (blue), (D) cyclic RGD (green), (E) NP in dms0-d6 (red).

Nanosponges functionalized with cyclic RGDEKf-Ahx-C peptide and fluorescent imaging moieties were then tested in A549 human lung cancer models to validate  $\alpha_v\beta_3$  integrin receptor targeting (Figure 4.3). Cells were cultured overnight and treated with targeted nanosponges, targeted nanosponges and competitor (vitronectin), or untargeted control nanosponges. Following incubation for 1 hr, they were washed twice with phosphate buffered saline and prepared for confocal microscopy.

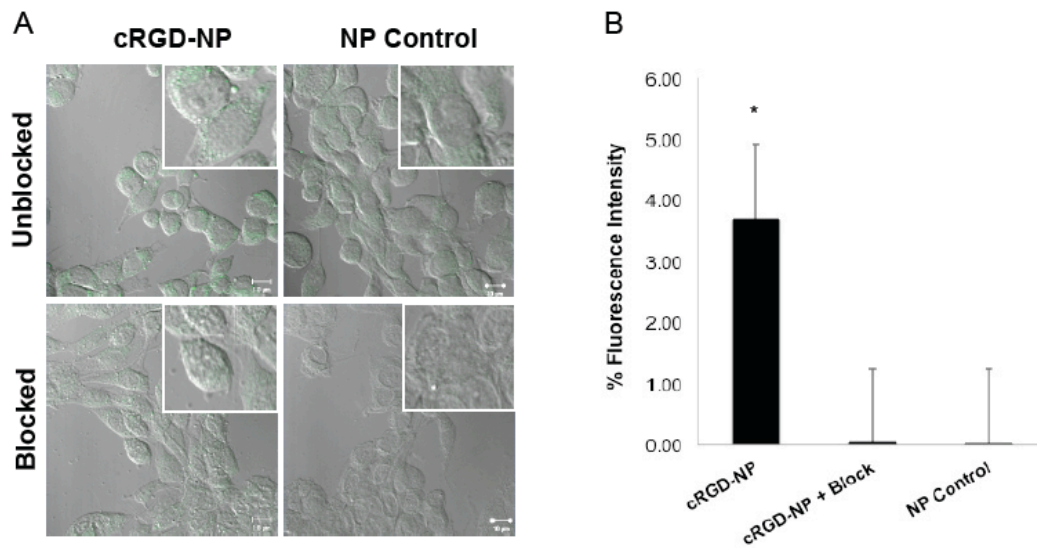


**Figure 4.3.** Imaging RGDEKf-Ahx-C-NP-AF488 binding to cells (cell imaging, bar graph of fluorescence). (A) Confocal microscopy analysis of integrin specific targeting in A549 lung carcinoma cells treated with synthesized cRGD-NP, untargeted NP controls, or blocked with 1 mg/ml Vitronectin for 1 hr. Cells were fixed and visualized by confocal microscopy. Zeiss LSM 710, 63x magnification. (B) Bar graph of fluorescence intensity. Bars, mean and SE for 3 fields of view. Unpaired Student's t test ( $P \leq 0.05$ )

The  $\alpha_v\beta_3$  integrin receptor present on cancer cell membranes is known to bind RGD ligands and peptides with RGD motifs. In order to determine preferential RGD peptide binding to integrin receptors, vitronectin (a glycoprotein with an RGD sequence) was used to compete with the specific binding of peptides to integrins. Cells treated with the targeted group alone show significantly greater fluorescence along the membrane and peripheral areas compared to cells treated with vitronectin competitor and untargeted controls (Figure 4.4). These studies validate cyclic RGD peptide targeting to integrin receptors in human lung cancer cells and show preferential binding compared to untargeted controls.

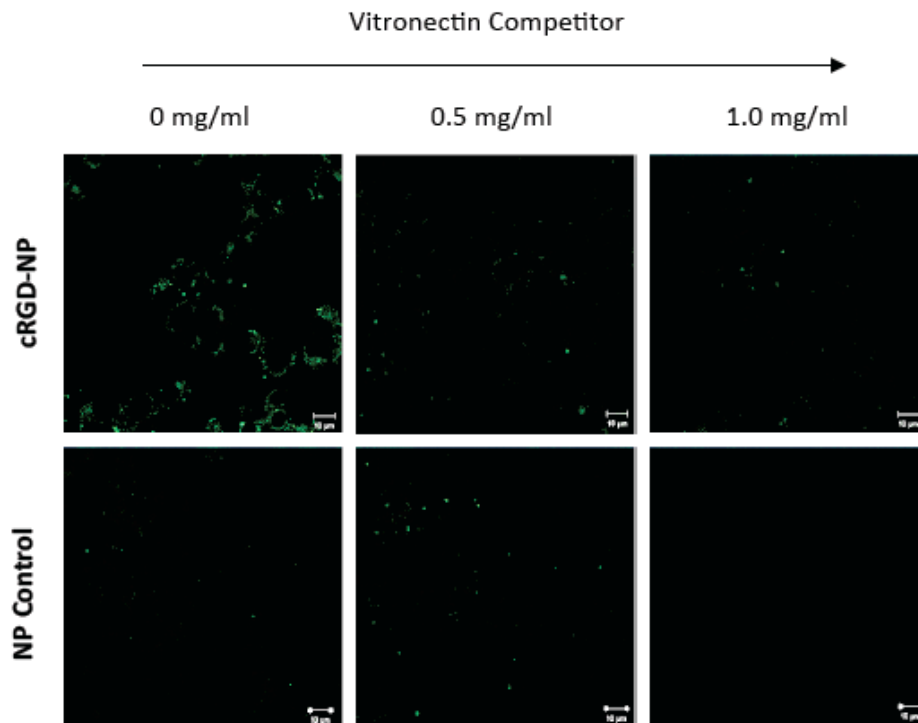


**Figure 4.4.** Imaging vitronectin competition studies with RGDEKf-Ahx-C-NP-AF488. (cell imaging, bar graph of fluorescence). Competition assay with 0, 0.5 and 1 mg/ml Vitronectin for 1 hr.

## ***Conclusion***

These studies show the synthesis of a cyclic RGDEKf-Ahx-C tumor targeting peptide, attachment to nanosponges, and modification with a fluorescent probe for *in vitro* cell imaging applications. Confocal microscopy shows competitive binding of cyclic RGD targeted NPs compared to untargeted controls and competitive binding controls with vitronectin competitor. These results indicate that this cyclic RGD peptide binds specifically in a dose responsive way to the  $\alpha_v\beta_3$  integrin receptor present on lung cancer cells *in vitro*, and can be used to target nanosponges specifically to this receptor on cancer cells.

## References

1. Sheldrake H.M., and Patterson L.H. Function and Antagonism of beta 3 integrins in the development of cancer therapy. *Current Cancer Drug Targets* 2009, 9(4), 519-540.
2. Hynes R.O. Integrins: bidirectional, allosteric signaling machines. *Cell* 2002, 110, 673-687.
3. Hood J.D, Cheresch D.A. Role of integrins in cell invasion and migration. *Nat. Rev. Cancer* 2002, 2(2), 91-100.
4. Mizejewski G.J. Role of integrins in cancer: survey of expression patterns. *P. Soc. Exp. Biol. Med.* 1999, 222(2), 124-138.
5. Desgrosellier J.S., Cheresch D.A. Integrins in cancer: biological implications and therapeutic opportunities. *Nat. Rev. Cancer* 10(1), 9-22 (2010).
6. Silletti, S., et al. Disruption of matrix metalloproteinase 2 binding to integrin  $\alpha_v\beta_3$  by an organic molecule inhibits angiogenesis and tumor growth in vivo. *Proc. Nat. Acad. Science* 2001, 98, 119-124.
7. Buckley C.D., et al. RGD peptides induce apoptosis by direct caspase-3 activation. *Nature* 1999, 397, 534-539.
8. Dechantsreiter M.A., Planker E., Matha B., Lohof E., Holzemann G., Jonczyk A., et al. N-methylated cyclic RGD peptides as highly active and selective  $\alpha_v\beta_3$  integrin antagonists. *J. Med. Chem.* 1999, 42, 3033-3040.
9. Ruoslahti E., et al. Tumor-penetrating peptides. *Frontiers in Oncology* 2013, 3(216) 1-20.
10. Ruoslahti E. RGD and other recognition sequences for integrins. *Ann. Rev. Cell Develop. Biol.* 1996, 12, 697-715.
11. Ruoslahti E. The RGD story: a personal account. *Matrix Biology* 2003, 22, 459-65.
12. Ruoslahti E. RGD and other recognition sequences for integrins. *Ann. Rev. Cell Dev. Biol.* 1996, 12, 697-715.
13. Thumshirn G., Hersel U., Goodman S. and Kessler H. Multimeric cyclic RGD peptides as potentials tools for tumor targeting: solid-phase peptide synthesis and chemoselective oxime ligation. *Chem. Eur. J.* 2003, 9, 2717-2725.

14. Bogdanowich-Knipp S.J., Jois D.S.S, and Siahaan T.J. The effect of conformation on the solution stability of linear vs. cyclic RGD peptides. *J. Peptide Res.* 1999, 53, 523-529.
15. El-Faham A., Funosas R.S., Prohens R., and Albericio F. COMU: A safer and more effective replacement for benzotriazole-based uronium coupling reagents. *Chem. Eur. J.* 2009, 15, 9404-9416.
16. Chantell C.A., Onaiyekan M.A. and Menakuru M. Fast conventional Fmoc solid-phase peptide synthesis: a comparative study of different activators. *J. Pept. Sci.* 2012, 18(2), 88-91.
17. Merrifield R.B. Solid phase peptide synthesis I: The synthesis of a tetrapeptide. *J. Am. Chem. Soc.* 1963, 85, 2149-2154.
18. Conroy T., Jolliffe K.A. and Payne R.J. Efficient use of the Dmab protecting group: applications for the solid-phase synthesis of N-linked glycopeptides. *Org. Biomol. Chem.* 2009, 7, 2255-2258.
19. Berthelot T., Goncalves M., La G., Estieu-Gionneta K. and Deleris G. New strategy towards the efficient solid phase synthesis of cyclopeptides. *Tetrahedron* 2006, 62, 1124-1130.
20. Dijkgraaf I., Kruijtz J.A.W., Liu S., Soede A.C., Oyen W.J.G., Corstens F.H.M., Liskamp R.M.J. and Boerman O.C. Improved targeting of the  $\alpha_v\beta_3$  integrin by multimerisation of RGD peptides. *Eur. J. Nucl. Med. Mol. Imaging* 2007, 34, 267-273.
21. Montet X., Funovics M., Montet-Abou K., Weissleder R., Josephson L. Multivalent effects of RGD peptides obtained by nanoparticle display. *J. Med. Chem.* 2006, 49(20), 6087-6093.
22. Cheng Z., Wu Y., Xiong Z., Gambhir S.S. and Chen X. Near-infrared fluorescent RGD for optical imaging of integrin  $\alpha_v\beta_3$  expression in living mice. *Bioconjugate Chem.* 2005, 16, 1433-1441.
23. Zako T., Nagata H., Terada N. et al. Cyclic RGD peptide-labeled upconversion nanophosphors for tumor cell-targeted imaging. *Biochem. Biophys. Res. Co.* 2009, 381(1), 54-58.
24. Arosio D., Manzoni L., Araldi E.M.V., Caprini A., Monferini E. and Scolastico C. Functionalized cyclic RGD peptidomimetics: conjugable ligands for  $\alpha_v\beta_3$  receptor imaging. *Bioconjugate Chem.* 2009, 20, 1611-1617.
25. Montet X., Montet-Abou K., Reynolds F., Weissleder R., Josephson L. Nanoparticle imaging of integrins on tumor cells. *Neoplasia* 2006, 8(3), 214-222.

26. Loyer P., Bedhouche W., Huang Z.W. Degradable and biocompatible nanoparticles decorated with cyclic RGD peptide for efficient drug delivery to hepatoma cells in vitro. *Int. J. Pharm.* 2013, 454(2), 727-737.
27. Arap W., Pasqualini R. and Ruoslahti E. Cancer treatment by targeted drug delivery to tumor vasculature in a mouse model. *Science* 1998, 279, 377-380.
28. Chen K. and Chen X. Integrin targeted delivery of chemotherapeutics. *Theranostics* 2011, 1, 189-200.
29. Arosio D., et al. Cyclic RGD functionalized gold nanoparticles for tumor targeting. *Bioconjugate Chemistry* 2011, 22, 664-672.
30. Sugahara K.N., et al. Coadministration of a tumor-penetrating peptide enhances the efficacy of cancer drugs. *Science* 2010, 329, 1031-1035.
31. Temming K., Schiffelers R.M., Molema G., Kok R.J. RGD-based strategies for selective delivery of therapeutics and imaging agents to the tumour vasculature. *Drug Resist. Update* 2005, 8(6), 381-402.
32. Danhier F., Vroman B., Lecouturier N., et al. Targeting of tumor endothelium by RGD-grafted PLGA-nanoparticles loaded with paclitaxel. *J. Control. Release* 2009, 140(2), 166-173.
33. Lowe A.B. Thiol-ene “click” reactions and recent applications in polymer and materials synthesis. *Polym. Chem.* 2010, 1, 17-36.
34. Hoyle C.E. and Bowman C.N. Thiol-ene click chemistry. *Ang. Chem. Int. Ed.* 2010, 49(9), 1540-73.

## CHAPTER 5

### SEQUENTIAL TARGETED DELIVERY OF PACLITAXEL AND CAMPTOTHECIN USING A CROSS-LINKED ‘NANOSPONGE’ NETWORK FOR LUNG CANCER CHEMOTHERAPY

#### ***Abstract***

The applicability of a HVGGSSV peptide targeted ‘nanosponge’ drug delivery system for sequential administration of a microtubule inhibitor (paclitaxel) and topoisomerase I inhibitor (camptothecin) was investigated in a lung cancer model. *In vivo* molecular imaging and TEM studies validated HVGGSSV-NP tumor binding at 24 hrs and confirmed the presence of Nanogold labeled HVGGSSV-NPs in tumor microvascular endothelial cells. Therapeutic efficacy studies conducted with sequential HVGGSSV targeted NP PTX and NP CPT showed 2-fold greater tumor growth delay in combination versus monotherapy treated groups, and 4-fold greater delay compared to untargeted and systemic drug controls. Analytical HPLC/MS methods were used to quantify drug content in tumor tissues at various time points, with significant paclitaxel and camptothecin levels in tumors 2 days post-injection and continued presence of both drugs up to 23 days post-injection. The efficacy of the NP drug delivery system in sequential treatments was demonstrated in *in vivo* lung cancer models resulting in enhanced apoptotic cell death, decreased cell proliferation and vascular density.



## ***Introduction***

Many conventional chemotherapy protocols for the treatment of cancer produce side effects that limit biological efficacy and compromise patient outcomes.<sup>1</sup> In addition to affecting proliferating cancer cells, these cytotoxic drugs also affect other rapidly dividing cells including cells in the gastrointestinal tract, bone marrow cells and hair follicles. Additionally, due to the hydrophobic nature of many chemotherapeutic drugs, parenteral administration via intravenous infusion typically requires the use of formulation vehicles (such as Cremophor<sup>®</sup> EL), which have been noted to produce undesirable biological reactions such as hypersensitivity and toxicity. Although the development of targeted drug delivery systems has allowed cytotoxic chemotherapeutics to be administered selectively to malignant tumors while sparing healthy tissues from undesirable side effects, solubilization of drugs and tailoring the drug dosage remain a challenge.<sup>2,3</sup> Therefore, degradable drug carriers are being developed to target and release drugs in a controlled fashion.<sup>4-6</sup> In particular, ‘nanosponge’ materials have been found suitable due to their degradable polyester based nano-network, comprised of a cross-linked 3-dimensional scaffold, which can be synthesized in different sizes, network densities and can be functionalized with tumor targeting units and imaging agents to enable visualization *in vivo*.<sup>7-9</sup> Moreover, hydrophobic drugs can be loaded into these nanosponges via a developed nanosolubilization method to result in readily injectable formulations for direct administration to create a linear release of the drug.<sup>8</sup>

Previous studies have shown that functionalization of nanosponges with tumor targeting peptides enhances targeting and significantly reduces tumor growth in a breast cancer model compared to systemic paclitaxel.<sup>10</sup> Targeting of a wide variety of tumors

(breast, brain, lung, prostate, colon, etc.) with peptides to radiation-inducible receptors expressed following exposure to sub-therapeutic levels of ionizing radiation has been previously established.<sup>2,10-13</sup> These results motivated us to investigate combination chemotherapy with paclitaxel and camptothecin in order to capitalize on the advantageous features of the nanosponge drug delivery system for tumor-specific drug targeting, release and solubilization. In this study, the Tax-interacting protein 1 (TIP-1) targeting peptide (HVGGSSV) was used to guide the delivery system to lung tumors treated with ionizing radiation in a murine lung cancer model.<sup>14</sup>

In addition to tumor targeting, the potential of sequential combination drug delivery using these targeted nanocarriers is investigated using mitotic inhibitors and topoisomerase I inhibitors, in addition to establishing tumor targeting of these nanosponges. Paclitaxel (Taxol) has shown promise as a chemotherapeutic alone and in combination with other drugs such as camptothecin in the treatment of a variety of cancers.<sup>15,16</sup> As a mitotic inhibitor, its main mechanism of action involves the stabilization of microtubules, G2/M phase cell cycle arrest, disruption of mitosis, and apoptosis.<sup>15</sup> Camptothecin is a topoisomerase I inhibitor that causes DNA damage by reversibly stabilizing the covalent enzyme-DNA intermediate, causing DNA double strand breaks, S/G2 cell cycle arrest and apoptosis.<sup>17-19</sup> Despite its potency, the use of camptothecin in the clinic has been limited greatly due to its poor water solubility, toxicity and side effects. While analogues of camptothecin, such as Irinotecan and Topotecan, have been developed to enhance water solubility, toxicity still remains a limiting side effect.<sup>20</sup> As a result, targeted drug delivery systems that can provide sustained release of highly hydrophobic small molecules specifically at tumor sites

exhibit particular promise for combination chemotherapy where delivery of lower doses for extended times can help enhance efficacy and reduce toxicity. Moreover, continuous low doses of drug over time (metronomic chemotherapy), also allow for greater anti-angiogenic efficacy.<sup>21</sup> Biodegradable targeted nanosponges with a cross-linked polymeric architecture create controlled low dose drug release profiles that are highly suitable for this application. Furthermore, development of a tumor-specific drug delivery system that enhances drug solubility, provides sustained low dose drug release, and can be used with different drug combinations provides a unique opportunity for maximizing the potential of chemotherapy while reducing the limiting toxicities that lower treatment efficacy.<sup>22, 23</sup>

This work describes a comprehensive study using a developed targeted ‘nanosponge’ nanoparticle as carriers in a sequential combination treatment approach for lung cancer, which has not been investigated despite the known potency of both paclitaxel and camptothecin. Briefly, HVGGSSV targeted nanosponges were labeled with near-infrared fluorophores and Nanogold<sup>®</sup> to allow for *in vivo* optical imaging of nanoparticle biodistribution and ultrastructural studies with transmission electron microscopy (TEM) showing tumor targeting at the cellular level. *In vitro* studies compare drug loaded nanoparticles (NP PTX and NP CPT) in sequential, simultaneous and single drug treatment to determine the optimum combination and sequence (see chapter 3). Based on these findings, tumor targeted nanoparticles loaded with paclitaxel and camptothecin (HVGGSSV-NP PTX and HVGGSSV-NP CPT) are then administered sequentially in an *in vivo* lung cancer mouse model to study therapeutic efficacy of sequential treatment compared to controls. The following new findings are presented: (1) sequential administration of paclitaxel prior to camptothecin increases G2 cell cycle

arrest compared to simultaneous treatment in lung cancer cells (see chapter 3) (2) nanosponge formulation affords metronomic delivery of these drugs *in vitro* and *in vivo* (3) Tumor-specific targeting lowers increases bioavailability and enhances metronomic therapy.

## ***Experimental Materials and Methods***

### *Nanoparticle Preparation*

#### *Materials*

Chemical reagents were purchased from Sigma-Aldrich and Strem Chemicals, chemotherapeutic drugs from LC Laboratories. Peptides (GCGGGNHVGGSSV) were purchased from EZBiolab Inc. (Carmel, IN). Spectra/Por Dialysis membrane (MWCO=10,000) in 0.05% sodium azide was purchased from Spectrum Laboratories.

#### *Characterization*

*NMR Spectroscopy.* All  $^1\text{H}$  NMR spectra were acquired using a 400 MHz Bruker AV-400 NMR with deuterated chloroform ( $\text{CDCl}_3$ ) and tetramethylsilane as internal standard. Peptide labeled nanoparticles were analyzed using a 600 MHz Bruker AV-II NMR with deuterated dimethyl sulfoxide ( $\text{DMSO-d}_6$ ) and tetramethylsilane as internal standard.

*Purification.* Biotage Isolera Spektra One flash purification system equipped with a UV  $\lambda$  absorbance detector was used to purify AVL monomers. Purification was performed using a SNAP HP 50 g silica column with a 5-20% ethyl acetate gradient in n-hexanes with a flow rate of 50 ml/min. All monomers (AVL and VL) were vacuum distilled using a Kugelrohr distillation apparatus (Sigma Aldrich).

*Gel-permeation chromatography (GPC).* All GPC was performed using a Waters chromatography system equipped with refractive index and dual  $\lambda$  absorbance detectors, four 5 mm Waters columns (300 mm x 7.7 mm) with pore size (100, 1000, 100,000 and 1,000,000 Å respectively). All samples were dissolved in tetrahydrofuran (THF), with a 20  $\mu$ l injection volume and 1 mL/min flow rate.

*Transmission electron microscopy (TEM).* TEM imaging was performed on nanoparticles by dissolving approximately 5 mg in a solution of 1:0.4 mL isopropanol/acetonitrile. The dissolved nanoparticles were sonicated for 5 minutes and stained with 4 drops of a 3% phosphotungstic acid/water solution for 10 minutes. This solution was sonicated once more for 5 minutes before the copper grids were prepared. Ultrathin Carbon Type-A 400 mesh copper grids (Ted Pella, Redding, CA) were gently immersed into the stained nanoparticle solution and allowed to dry for 2 hrs prior to analysis. A 200 kV Philips CM20T transmission electron microscope was used to acquire micrographs of the nanoparticles.

#### *Preparation of Monomers*

##### *$\delta$ -valerolactone monomer (VL)*

Technical grade  $\delta$ -valerolactone was Kugelrohr distilled to produce a colorless liquid product.

##### *$\alpha$ -allyl- $\delta$ -valerolactone monomer (AVL)*

A flame dried 500 mL two-necked round bottom flask was equipped with a stir bar, sealed with a rubber septum, and purged with nitrogen for 30 min. To the flask, 156.25 mL of anhydrous THF was added and cooled to -78 °C in a dry ice/acetone bath. Following this, a basic solution of lithium diisopropylamine was produced by adding

redistilled n,n-diisopropylamine (3.3 mL, 23.63 mmol) and n-butyl lithium (2.5 M in hexanes) (9.35 mL, 23.38 mmol) dropwise via syringe. This solution was stirred for 20 minutes. A nitrogen purged solution of distilled  $\delta$ -valerolactone (1.97 mL, 21.23 mmol) in anhydrous THF (56 mL) was then added dropwise via syringe over 30 min. After an additional 30 min of stirring, a nitrogen purged solution of allyl bromide (2.21 mL, 25.54 mmol) in hexamethylphosphoramide (4.43 mL, 25.46 mmol) was added via syringe. The reaction mixture was warmed up to -40 °C and stirred for 2 hrs. The reaction was quenched with excess NH<sub>4</sub>Cl solution. The crude product was concentrated via rotary evaporator, washed three times with saturated NaCl solution, and dried with anhydrous magnesium sulfate. The crude product was purified via column chromatography (Biotage Isolera), analyzed by thin layer chromatography and Kugelrohr distilled. Chromatography with a gradient of 5-20% ethyl acetate in n-hexanes as eluent gave a yellow liquid product. Kugelrohr distillation produced a colorless liquid product. Yield: 3.56 g (89%). <sup>1</sup>H NMR (400MHz, CDCl<sub>3</sub>/TMS, ppm)  $\delta$ : 5.7 (m, 1H, H<sub>2</sub>C=CH-), 5.08 (m, 2H, H<sub>2</sub>C=CH-), 4.28 (m, 2H, -C(O)OCH<sub>2</sub>-), 2.53-2.58 (m, 2H, H<sub>2</sub>C=CHCH<sub>2</sub>-), 2.27 (m, 1H, H<sub>2</sub>C=CHCH<sub>2</sub>CH-), 2.06 (m, 1H, H<sub>2</sub>C=CHCH<sub>2</sub>CHCH<sub>2</sub>-), 1.89 (m, 2H, C(O)OCH<sub>2</sub>CH<sub>2</sub>-), 1.55 (m, 1H, H<sub>2</sub>C=CHCH<sub>2</sub>CHCH<sub>2</sub>-).

### *Preparation of Linear Polymer Precursors*

#### *Poly(VL-co-AVL) from Sn(OTf)<sub>2</sub> catalyst*

A flame dried 25 mL 3-necked round bottom flask was equipped with a stir bar, sealed with rubber septa and nitrogen purged. A stock solution of anhydrous ethanol in anhydrous tetrahydrofuran was prepared (1.7 M) in a 50 mL flame dried and nitrogen

purged round bottom flask, and a stock solution of Sn(OTf)<sub>2</sub> catalyst in anhydrous tetrahydrofuran was prepared ( $3.7 \times 10^{-2}$  M) in a 10 mL flame dried and nitrogen purged round bottom flask. Ethanol (584  $\mu$ L, 1.0 mmol) and Sn(OTf)<sub>2</sub> (261  $\mu$ L,  $9.64 \times 10^{-6}$  mol) were added via syringe to the 25 mL 3-neck round bottom flask and the catalyst/initiator solution was allowed to stir at room temperature for 30 minutes prior to simultaneous addition of  $\delta$ -valerolactone (2.22 g, 22.0 mmol) and  $\alpha$ -allyl(valerolactone) (0.777 g, 5.548 mmol) monomers via syringe. After addition of both monomers, the reaction was stirred for 24 hrs at room temperature. The resulting polymer was diluted with 1 mL anhydrous THF and purified by dropwise addition into 1 L of chilled methanol to remove any remaining monomer and catalyst. The methanol was decanted and the precipitate dissolved in methylene chloride, rotary evaporated and dried *in vacuo*. The resulting polymer was observed as a waxy white solid.  $M_w = 3000$  Da; PDI = 1.09; <sup>1</sup>H NMR (400 MHz, CDCl<sub>3</sub>/TMS, ppm)  $\delta$ : 5.72 (m, H<sub>2</sub>C=CH-), 5.04 (m, H<sub>2</sub>C=CH-), 4.08 (m, -CH<sub>2</sub>-O-), 3.64 (m, CH<sub>3</sub>CH<sub>2</sub>O-), 2.34 (m, vl, -CH<sub>2</sub>CH<sub>2</sub>C(O)O-, avl, H<sub>2</sub>C=CHCH<sub>2</sub>CH-, H<sub>2</sub>C=CHCH<sub>2</sub>CH-), 1.68 (m, avl and vl, -CHCH<sub>2</sub>CH<sub>2</sub>-), 1.26 (t, CH<sub>3</sub>CH<sub>2</sub>O-).

#### *Poly(VL-co-AVL) from Sn(Oct)<sub>2</sub> catalyst*

A flame dried 25 mL 3-necked round bottom flask was equipped with a stir bar, sealed with rubber septa and nitrogen purged. A stock solution of anhydrous ethanol in anhydrous tetrahydrofuran was prepared (1.7 M) in a 25 mL flame dried and nitrogen purged round bottom flask, and a stock solution of Sn(Oct)<sub>2</sub> catalyst in anhydrous tetrahydrofuran was prepared in a 10 mL flame dried and nitrogen purged round bottom flask. Ethanol (360  $\mu$ L,  $6.14 \times 10^{-1}$  mol) and Sn(Oct)<sub>2</sub> (330  $\mu$ L,  $1.22 \times 10^{-2}$  mol) were added via syringe to the 50 mL 3-neck round bottom flask and the catalyst/initiator

solution was allowed to stir at room temperature for 30 minutes prior to simultaneous addition of  $\delta$ -valerolactone (2.46 g,  $28.53 \times 10^{-3}$  mol) and  $\alpha$ -allyl(valerolactone) (0.93 g,  $7.134 \times 10^{-3}$  mol) monomers via syringe. After addition of both monomers, the reaction was stirred for 48 hrs at 105 °C in an oil bath. The resulting polymer was diluted with 1 mL methylene chloride and purified by dropwise addition into 1.5 L of chilled diethyl ether to remove any remaining monomer and catalyst. The ether was decanted and the precipitate dissolved in methylene chloride, rotary evaporated and dried *in vacuo*. The resulting polymer was observed as a viscous yellow liquid.  $^1\text{H}$  NMR (300 MHz,  $\text{CDCl}_3/\text{TMS}$ , ppm)  $\delta$ : 5.72 (m,  $\text{H}_2\text{C}=\text{CH}-$ ), 5.04 (m,  $\text{H}_2\text{C}=\text{CH}-$ ), 4.08 (m,  $-\text{CH}_2-\text{O}-$ ), 3.64 (m,  $\text{CH}_3\text{CH}_2\text{O}-$ ), 2.34 (m, vl,  $-\text{CH}_2\text{CH}_2\text{C}(\text{O})\text{O}-$ , avl,  $\text{H}_2\text{C}=\text{CHCH}_2\text{CH}-$ ,  $\text{H}_2\text{C}=\text{CHCH}_2\text{CH}-$ ), 1.68 (m, avl and vl,  $-\text{CHCH}_2\text{CH}_2-$ ), 1.26 (t,  $\text{CH}_3\text{CH}_2\text{O}-$ ).

#### *Poly(VL-co-AVL-co-EVL)*

In a 100 mL round bottom flask, equipped with stir bar and rubber septum, a solution of poly(VL-co-AVL) (1.0 g,  $1.55 \times 10^{-3}$  mol) was dissolved in 8.5 mL of methylene chloride. To this solution, meta-chloroperoxybenzoic acid (121.25 mg,  $7.03 \times 10^{-4}$  mol) was added. The solution was stirred for 24 hrs at room temperature and then concentrated via rotary evaporator. The crude product was dissolved in a minimal amount of dichloromethane (2 mL) and precipitated into an Erlenmeyer flask containing 500 mL cold diethyl ether. The solution was decanted, and the white solid was rotary evaporated and dried *in vacuo* to obtain the final white waxy polymer. Yield: 0.768 g (76.8%).  $^1\text{H}$  NMR (400MHz,  $\text{CDCl}_3/\text{TMS}$ , ppm)  $\delta$ : Decrease in allylic protons at 5.7 and 5.09 ppm and the appearance of small broad resonance peaks at 2.96, 2.75 and 2.47 ppm due to the formation of the epoxide.



### *Formation of nanosponges*

In a 250 mL round bottom flask equipped with stir bar and reflux condenser, a solution of 2,2'-(ethylenedioxy) diethylamine (10.5  $\mu\text{L}$ ,  $7.18 \times 10^{-5}$  mol) in 29.55 mL methylene chloride was heated at 45 °C. A solution of poly(VL-*co*-AVL-*co*-EVL), (0.200 g,  $M_w = 3000$  Da) dissolved in methylene chloride was added. The mixture was refluxed at 45 °C for 12 hrs. Residual diamine crosslinker was removed via dialysis against methylene chloride with Spectra/Por Dialysis Tubing (MWCO = 10,000). Nanosponges were made from poly(VL-*co*-AVL) using  $\text{Sn}(\text{OTf})_2$  and  $\text{Sn}(\text{Oct})_2$  catalysts.  $^1\text{H}$  NMR (400 MHz,  $\text{CDCl}_3/\text{TMS}$ , ppm)  $\delta$ : Decrease in number of epoxide protons at 2.96, 2.75 and 2.47 ppm and the appearance of signals at 3.5 and 2.89 ppm corresponding to the protons near the secondary amine of the diamine crosslinker after the reaction.

### *Addition of targeting peptide via photoinitiated thiol-ene 'click' reaction*

Poly(VL-*co*-AVL-*co*-EVL) nanoparticles were dissolved in dichloromethane and purified using Sephadex column chromatography, rotary evaporated and dried *in vacuo*. Anhydrous, degassed DMSO (1 mL) was used to dissolve 20 mg of poly(VL-*co*-AVL-*co*-EVL) nanoparticles, 7.2 mg of GCGGGNHVGGSSV peptide (EZ BioLabs) and 3.4 mg DMPA (2 eq. with respect to peptide). Mixture was stirred for 2 days in an oil bath at 37 °C under ultraviolet light at 365 nm. The product was purified by dialysis (MWCO = 10,000) against methanol/acetonitrile (1:1) for 2 days, rotary evaporated and dried *in vacuo*.

### *Quantification of peptide units on nanoparticles via $^1\text{H}$ NMR:*

Since the primary thiol functional group from the cysteine residue in the peptide (GCGGGNHVGGSSV) reacts with the allyl groups in the nanoparticle in a 1:1

stoichiometry, the allyl groups that are consumed in the reaction directly correlate with how many peptides are bound to the nanoparticle. By comparing the percent allyl groups in the nanoparticle before and after peptide attachment, the difference can be used to calculate the number of bound peptides. The nanoparticle peak at 4.08 ppm is used as an internal standard for determining the number of unmodified allyl groups remaining after the photoinitiated thiol-ene click reaction for peptide attachment.

*Modification of HVGGSSV-NPs for in vivo NIR imaging with NHS Alexa Fluor 750 and Mono-Sulfo-NHS Nanogold<sup>®</sup>*

HVGGSSV modified poly(VL-co-AVL-co-EVL) nanoparticles (30 mg) and unmodified nanoparticles (30 mg) were separately dissolved in anhydrous DMSO (600 uL). To each solution, NHS Alexa Fluor 750 (75 uL) and Mono-Sulfo-NHS Nanogold<sup>®</sup> (10 uL) was added simultaneously and the resulting mixture was stirred for 6 hrs (covered in foil to protect from light). The product was purified by dialysis (MWCO=10,000) against methanol/acetonitrile (1:1) overnight, rotary evaporated and dried *in vacuo* (covered in foil to protect from light).

*Cell Culture*

Murine Lewis lung carcinoma (LLC) cells were obtained from the American Type Culture Collection (Rockville, MD,). They were grown to 70% confluence in Dulbecco's Modified Eagle Medium supplemented with 10% fetal bovine serum and 1% antibiotic/antimycotic. All cultures maintained at 37°C in incubator with 95% humidity and 5% CO<sub>2</sub>.

### *Animal models*

Male athymic nude mice (*nu/nu*) and C57BL6 mice were purchased from Harlan Laboratories (Indianapolis, IN). All *in vivo* animal protocols were approved by the Institutional Animal Care and Use Committee (IACUC). Animals were anesthetized using a ketamine and xylazine solution prior to injection of  $1 \times 10^6$  LLC cells subcutaneously in the hind limbs. Once tumors reached an approximate size of 0.5 cm in diameter mice were used for *in vivo* studies.

### *Radiation treatment*

In order to stimulate expression of radiation-induced TIP-1 in tumors, each tumor was treated with sub-therapeutic levels of ionizing radiation prior to drug administration. Mice were anesthetized to inhibit movement and covered with lead blocks of 1 cm thickness, leaving only the hind limb tumor exposed for treatment. Tumors were treated with 3 Gy ionizing radiation at 300 kV, using a Pantak Therapax 3 linear accelerator system (Pantak), with an adjustable collimator set to focus dosage exclusively to tumors. Four hours following irradiation, mice were intravenously administered nanoparticle drug treatments via lateral tail vein.

### *NIR fluorescence imaging and analysis*

Near-infrared (NIR) fluorescence imaging was done on athymic nude mice using a Xenogen IVIS 200 small animal imaging system (Xenogen Inc., CA). A filter with excitation and emission at 680/775 nm was used for acquisition of all images. Briefly, a single dose of 3 Gy radiation was given to tumors in mice receiving targeted HVGSSV-NP and no radiation was applied for HVGSSV-NP controls and untargeted controls. Four hours after irradiation, nanoparticles were injected. At 24 hrs post-injection, mice

were immobilized with continuous administration of isoflurane gas, and images were acquired, with exposure times of 1 second and an f/stop of 2. In order to compare fluorescence in tumor regions quantitatively, regions of interest (ROIs) were created over tumor areas, and the total radiance for each ROI was measured in p/s/cm<sup>2</sup>/sr. Results are presented as mean and standard error for groups of three mice.

#### *Tumor growth delay studies*

For *in vivo* studies, six-week-old male C57BL6 mice were used. All mice were injected with  $1 \times 10^6$  LLC cells subcutaneously above their right hind limbs. Tumor volume was measured manually using calipers, and tumor volume was calculated using the formula: volume =  $0.5 (\text{length} \times \text{width}^2)$ . Upon reaching an approximate diameter of 0.5 cm, mice were divided into groups and administered nanoparticle drug conjugates (10 mg/kg calculated for amount of each drug, 50-100  $\mu\text{L}$  volume in PBS) intravenously through lateral tail vein. Mice receiving targeted treatments on day 1, were given 3 Gy radiation and injected 4 hrs later with either HVGGSSV-NP PTX, HVGGSSV-NP CPT, or HVGGSSV-NP PTX (day 1)  $\rightarrow$  HVGGSSV-NP CPT (day 9). Mice receiving untargeted treatments on day 1 were given no radiation and injected with NP PTX, NP CPT, or systemic (free) PTX. Mice receiving radiation (RT) only on day 1 received 3 Gy radiation, and mice receiving no drug (control) on day 1 were injected with PBS vehicle.

#### *Tissue transmission electron microscopy (TEM)*

Peptide modified nanoparticles labeled with Nanogold<sup>®</sup> were injected intravenously via lateral tail vein in a volume of 0.1-0.2 mL. At 24 hrs after injection, tumor tissues were excised and cut into 1-2 mm<sup>3</sup> cubes with a razor blade and fixed in a solution of 3% glutaraldehyde in cacodylate buffer overnight at 4 °C. Tissue sections were subsequently

fixed in 2% osmium tetroxide in 100 mM cacodylate buffer, pH 7.4, overnight at 4 °C. Following treatment with 2% uranyl acetate for 48 hrs at 37 °C, tumor tissues were embedded in epoxy resin and thick-sectioned. Regions of interest were selected under a light microscope and recut into thin sections subsequently stained with lead citrate. Sections were placed onto copper grids and examined with a Philips/FEI T-12 high-resolution transmission electron microscope with a 2000 x 2000 AMT CCD camera system. Acquired images were then analyzed using AMT image capture software.

#### *Drug quantification*

At determined time points (days 2, 7, 14, 23) following injections, tumors were excised and homogenized. Tumor tissue homogenates (200 µL) were extracted by protein precipitation with 500 µL acetonitrile spiked with 100 µL internal standard. Samples were vortexed and centrifuged for 10 minutes at 3000 rpm. The supernatant was then filtered using centrifugal filters (Amicon Ultra, Millipore) for another 30 minutes at 3000 rpm, and the resulting filtrate was evaporated. It was reconstituted in 20 mM ammonium formate in acetonitrile/water (1:1) and analyzed by HPLC/MS using a Phenomenex Luna C18 analytical column, with an injection volume of 20 µL and flow rate of 300 µL/minute. Mobile phase A was 20 mM ammonium formate in water/acetonitrile (95:5, v:v) and mobile phase B was 20 mM ammonium formate in water/acetonitrile (5:95, v:v).

#### *Immunohistochemistry*

To determine changes in cell proliferation, cell death and tumor vascular density *in vivo*, six-week-old male C57BL6 mice were injected with  $1 \times 10^6$  LLC cells subcutaneously above their right hind limbs. Upon reaching an approximate diameter of 0.5 cm, mice were divided into groups and administered drug loaded nanoparticles (10 mg/kg

calculated for each drug, 50-100  $\mu$ L volume in PBS) intravenously through lateral tail vein. Mice receiving targeted treatments on day 1, were given 3 Gy radiation and injected 4 hrs later with either HVGGSSV-NP PTX, HVGGSSV-NP CPT, or HVGGSSV-NP PTX (day 1)  $\rightarrow$  HVGGSSV-NP CPT (day 9). Mice receiving untargeted treatments on day 1 were given no radiation and injected with either NP PTX or NP CPT. Mice receiving no drug (control) on day 1 were injected with PBS vehicle. Fourteen days following injections, tumors were excised and fixed in a solution of 10% formalin for 48 hrs. Paraffin-embedded tissues were sectioned into 10  $\mu$ m thick sections and treated with anti-cleaved caspase-3 antibody for detection of apoptotic cells, anti-Ki67 antibody for detection of cell proliferation, and anti-CD31 antibody for detection of blood vessels. Slides were viewed using a Zeiss Axiophot wide field microscope, and images taken at 10x magnification. Images were acquired from three fields of view and the number of cells expressing either cleaved caspase-3, Ki67, or CD31 was counted. Dark stained nuclei were scored positive, and blue nuclei were scored as negative. Bar graphs shown represent the number of cells as a percentage of total cells counted. All images were analyzed using MetaMorph image acquisition and analysis software.

#### *Statistical analysis*

Statistical analysis was performed using mean and standard error (SE), with student's *t* test and *p* values less than 0.05 considered significant. *P* values are shown on bar graphs with asterisks, where \* represents  $p \leq 0.05$ , \*\* represents  $p \leq 0.01$ , and \*\*\* represents  $p \leq 0.001$  per statistical convention.

### ***Results and discussion***

Previously, the HVGGSSV peptide has been shown to have tumor-specific binding to the TIP-1 protein found in irradiated tumors.<sup>14, 28</sup> In this study we report the use of HVGGSSV peptide for targeting of polyester nanoparticles in a murine LLC tumor model. Nanoparticles were synthesized and functionalized with HVGGSSV peptide (HVGGSSV-NP), and labeled with Alexa Fluor<sup>®</sup> 750 near-infrared fluorophore (Figure 5.1A,B). These targeted fluorescent nanoparticles were then injected into nude mice with irradiated LLC tumors, and imaged via NIR fluorescent imaging to visualize tumor binding *in vivo* (Figure 5.2A). At 24 hrs post-injection, mice receiving HVGGSSV targeted nanoparticles exhibited 7.9 times greater fluorescence in irradiated tumors compared to unirradiated controls, and over two times greater fluorescence compared to untargeted nanoparticle controls (Figure 5.2B). In order to determine specifically where in the tumor tissue these targeted nanoparticles were delivered, targeted and untargeted nanoparticles were functionalized with Nanogold<sup>®</sup> (Figure 5.1C).

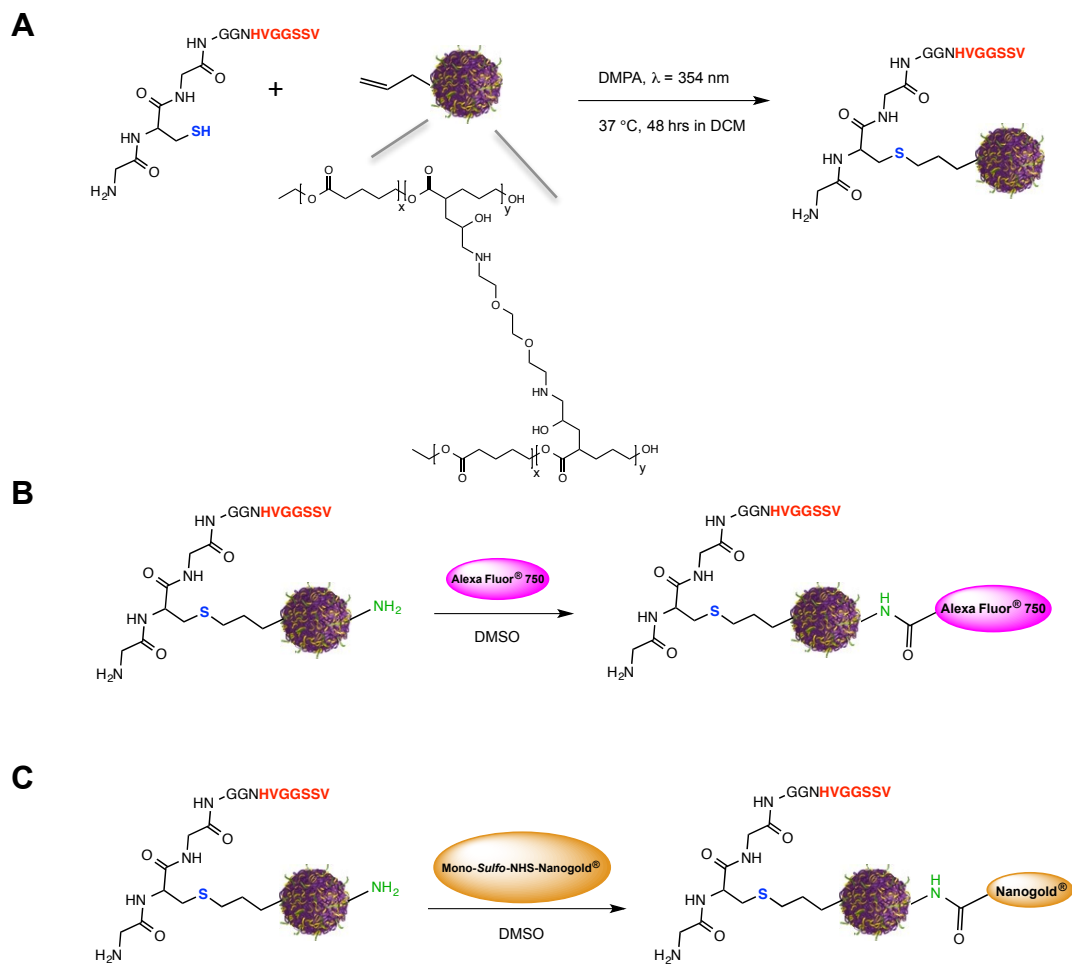


**Figure 5.1.** Synthesis of polyester nanoparticles functionalized with HVGGSSV targeting peptide (A) and Alexa Fluor<sup>®</sup> 750 near-infrared fluorophore imaging agents (B) and Nanogold<sup>®</sup> -HVGGSSV nanoparticles (C).



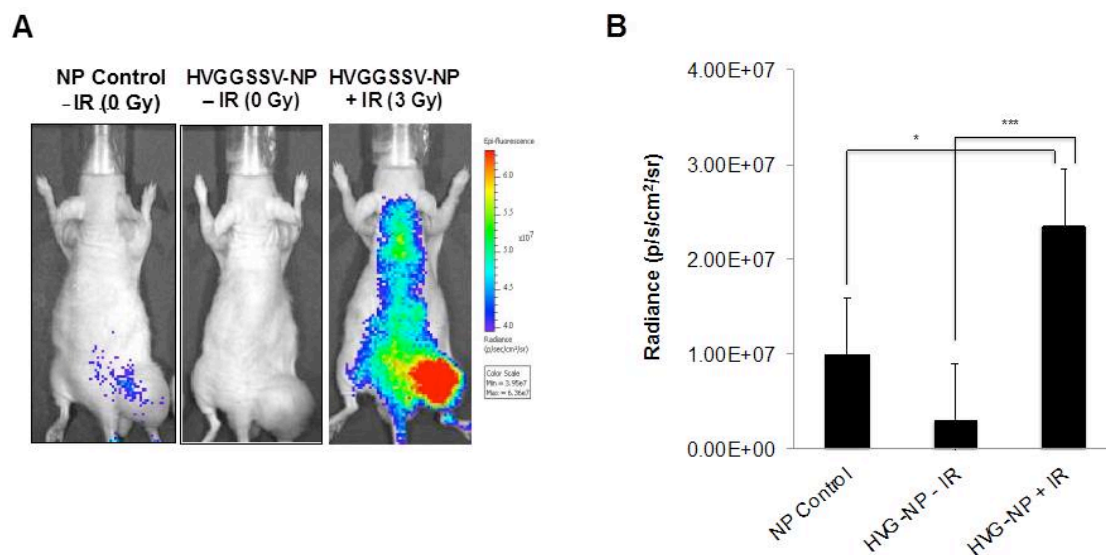


**Figure 5.2.** Near-infrared (NIR) fluorescence imaging of HVGGSSV-NPs in an LLC model at 24 hrs post-injection (A). Nude athymic mice with heterotopic tumors (right hind limb) were intravenously injected with untargeted nanoparticle controls and unirradiated (0 Gy) (left), HVGGSSV-NPs in unirradiated (0 Gy) tumor controls (middle), or HVGGSSV-NPs in irradiated (3 Gy) tumors (right). Radiance for HVGGSSV-NPs in irradiated tumors and unirradiated control tumors compared to untargeted nanoparticle controls (B). Color scale bar, radiance in units of photons/s/cm<sup>2</sup>/sr. Bars, mean and SE for n=3, unpaired Student's t test (p<0.05).

These small (1-2 nm) gold particles have high electron density, producing enhanced image contrast in TEM due to greater absorption of these electrons at lower magnification. Nanogold<sup>®</sup> functionalized HVGGSSV-NP and untargeted NP controls were injected intravenously into C57BL6 mice and tumors excised 24 hrs post-injection. TEM images show preferential accumulation of Nanogold (seen as black 'dots' in yellow regions of interest) within tumor vascular endothelium in HVGGSSV targeted tumors but not in untargeted control tumors at 24 hrs (Figure 5.3 A,B). Areas with higher concentrations of Nanogold indirectly show presence of HVGGSSV targeted nanoparticles (see insets), and confirm tumor-specific binding of these nanoparticles compared to untargeted controls.

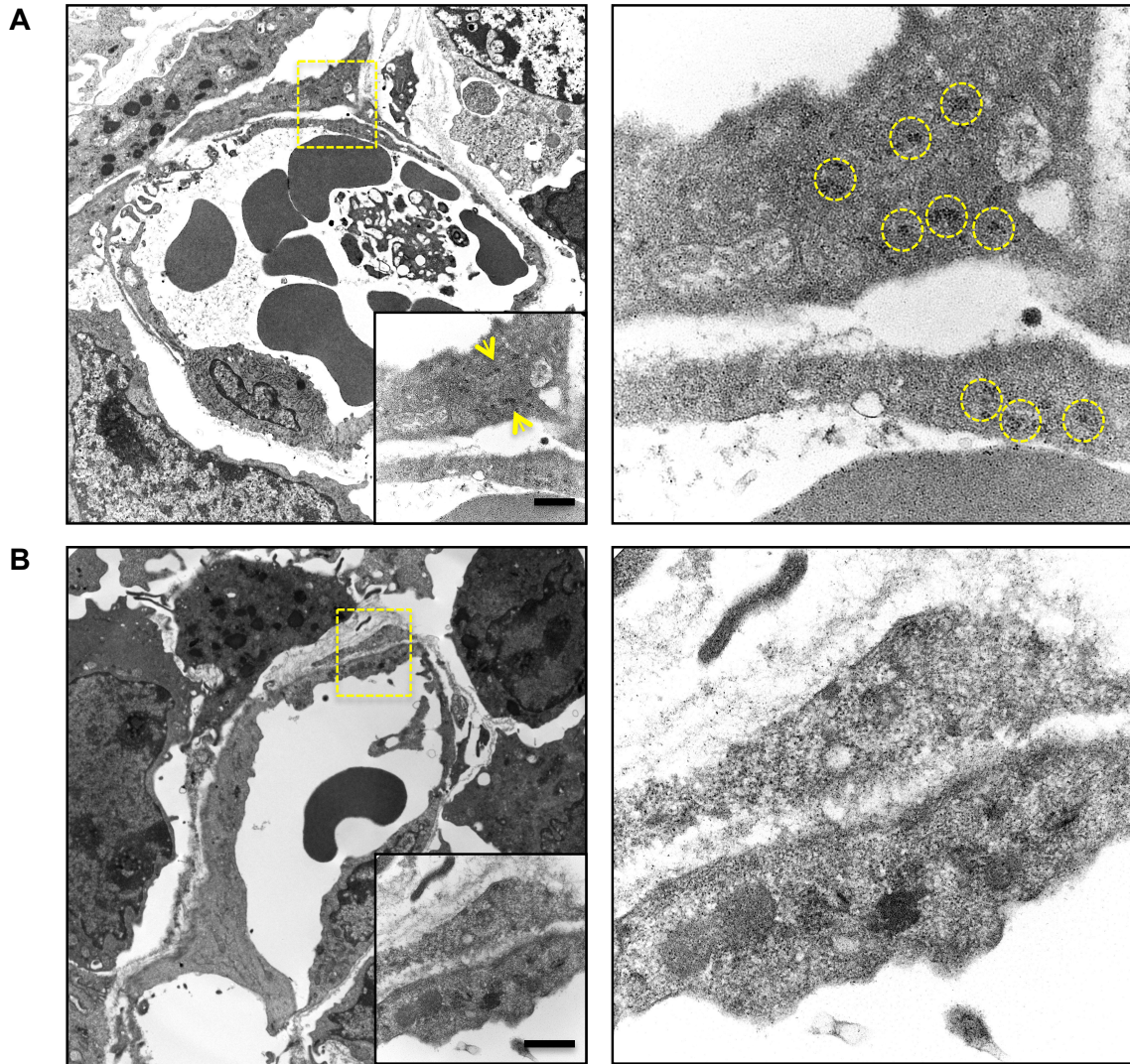


**Figure 5.3.** TEM micrographs of LLC tumors treated with Nanogold<sup>®</sup> labeled HVGSSV-NPs in a murine model at 24 hrs post-injection. C57BL6 mice with heterotopic tumors (right hind limb) were intravenously injected with (A) Nanogold<sup>®</sup> labeled HVGSSV-NP in irradiated (3 Gy) tumors or (B) untargeted nanoparticle controls. Tumors were excised at 24 hrs post injection, fixed and processed for TEM analysis. A cross-section of a tumor blood vessel is shown in each micrograph. Nanoparticles (dark spheres indicated by arrows and yellow regions of interest) can be seen localized inside tumor microvascular endothelial cells. Scale bar indicates 2  $\mu$ m.

Based on the results observed *in vitro* (see chapter 3), the nanoparticle drug combination and sequence with the greatest therapeutic effect on cells was selected for functionalization with tumor-specific peptide HVGGSSV, and was tested *in vivo* to evaluate tumor-specific targeting, drug delivery and therapeutic efficacy. Specifically, sequential targeted HVGGSSV-NP PTX → HVGGSSV-NP CPT (i.e. HVGGSSV-NP paclitaxel administered before HVGGSSV-NP camptothecin) was compared to targeted and untargeted monotherapy controls, radiation only, and untreated controls. To evaluate therapeutic efficacy, tumor growth delay studies in a LLC model were performed to compare the tumor volume doubling time across different treatment groups. Figure 5.4A shows that untargeted monotherapy controls showed no significant tumor growth delay compared to untreated controls, with radiation only and systemic (free) paclitaxel controls showing a slight increase (1 day). Both HVGGSSV targeted NP PTX and NP CPT showed significant growth delay compared to untargeted controls (4 days). Sequential injection of camptothecin 8 days after paclitaxel administration produced a tumor doubling time of 21 days vs. 9 days for HVGGSSV targeted single drug controls (Figure 5.4B). The greatest growth delay was observed between sequential targeted treatment groups and untargeted single drug controls (16 days) (Figure 5.4A).

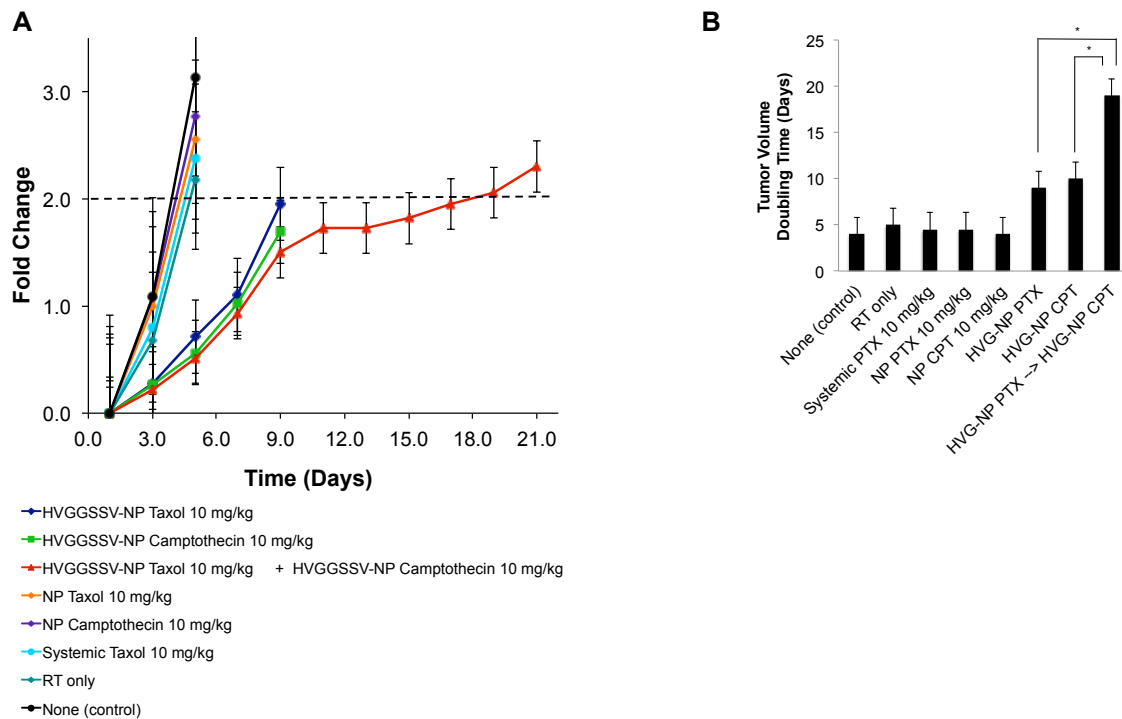


**Figure 5.4.** Tumor growth delay analysis of HVGGSSV peptide targeted nanoparticles loaded with paclitaxel or camptothecin. C57BL6 mice with LLC tumors grown on hind limbs were irradiated with 3 Gy on day 1 and injected 4 hrs later with either HVGGSSV-NP PTX, HVGGSSV-NP CPT, HVGGSSV-NP PTX → HVGGSSV-NP CPT, NP PTX, NP CPT, systemic (free) PTX, radiation only, or untreated. Sequential HVGGSSV-NP PTX → HVGGSSV-NP CPT treatment group was given second injection on day nine. All drugs were administered at a dose of 10 mg/kg, intravenously via tail vein (A). Time in days for tumors to reach two-fold volume (B). Bars, mean and SE for n=3, unpaired Student's t test ( $p < 0.05$ ).

To validate presence of drugs in tumor tissues, analytical HPLC/MS was used to quantify drug levels at 2, 7, 14 and 23 days post-injection. Tumors treated with targeted HVGGSSV-NP PTX showed the highest levels of paclitaxel at day 2 post-injection with continued presence of paclitaxel up to 23 days post-injection as shown in Figure 5.5A. Tumors treated with targeted HVGGSSV-NP CPT showed similar levels of camptothecin over time, in lower concentrations at day 2, with steady concentrations up to day 23 as

well. Chromatograms of both drugs present in sequentially treated HVGGSSV-NP PTX → HVGGSSV-NP CPT tumor tissues can be seen at day 14 (Figure 5.5B). Differences in metabolism, elimination and half-life for each drug can cause changes in drug levels seen over time, with NP CPT showing faster metabolism and elimination compared to paclitaxel. Continuous and steady levels of both drugs can be seen from day 7 to 23, indicating sustained and linear levels of drug release from nanoparticles over time, which is important for metronomic chemotherapy (Figure 5.5A).

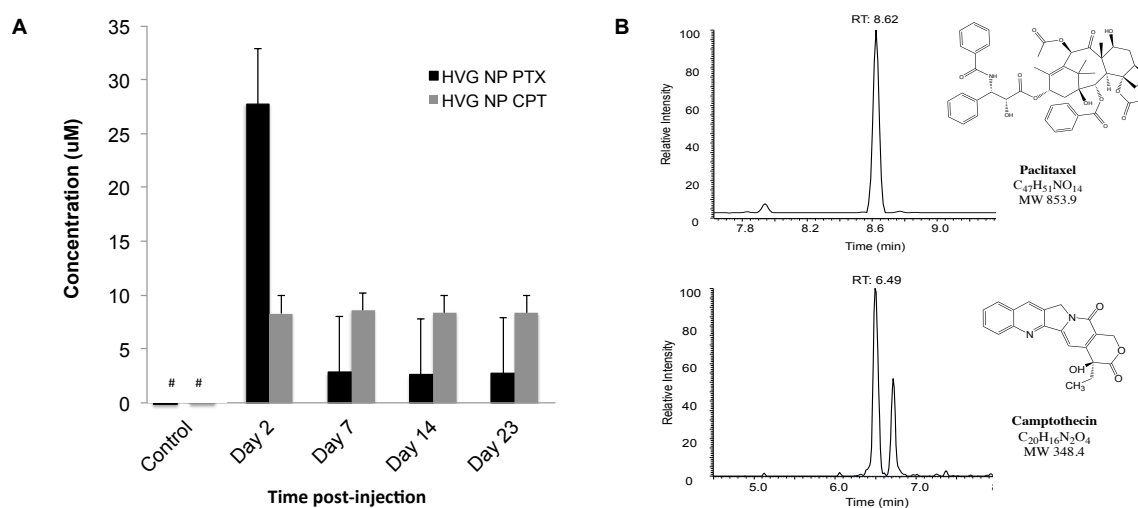


**Figure 5.5.** Quantification of paclitaxel and camptothecin content in LLC tumor tissues following treatment with HVGGSSV-NP PTX, HVGGSSV-NP CPT, and HVGGSSV-NP PTX → HVGGSSV-NP CPT. Concentrations of paclitaxel and camptothecin in tumors at 2, 7, 14 and 23 days post-injection (A). PTX and CPT levels in untargeted controls were below the limit of detection (indicated by #). Chromatograms for tumor tissue excised at 14 days post-injection show presence of paclitaxel (top) and camptothecin (bottom) (B).

To determine the mechanism of cell death, further immunohistochemical analyses were performed on tumor tissues to probe for cell proliferation, cell death and microvascular endothelial cells. Cellular proliferation seen with sequentially targeted treatment (i.e. HVGSSV-NP paclitaxel administered before HVGSSV-NP camptothecin) was significantly decreased compared to targeted camptothecin monotherapy and untreated controls, but not targeted paclitaxel monotherapy controls (Figure 5.6A,B).

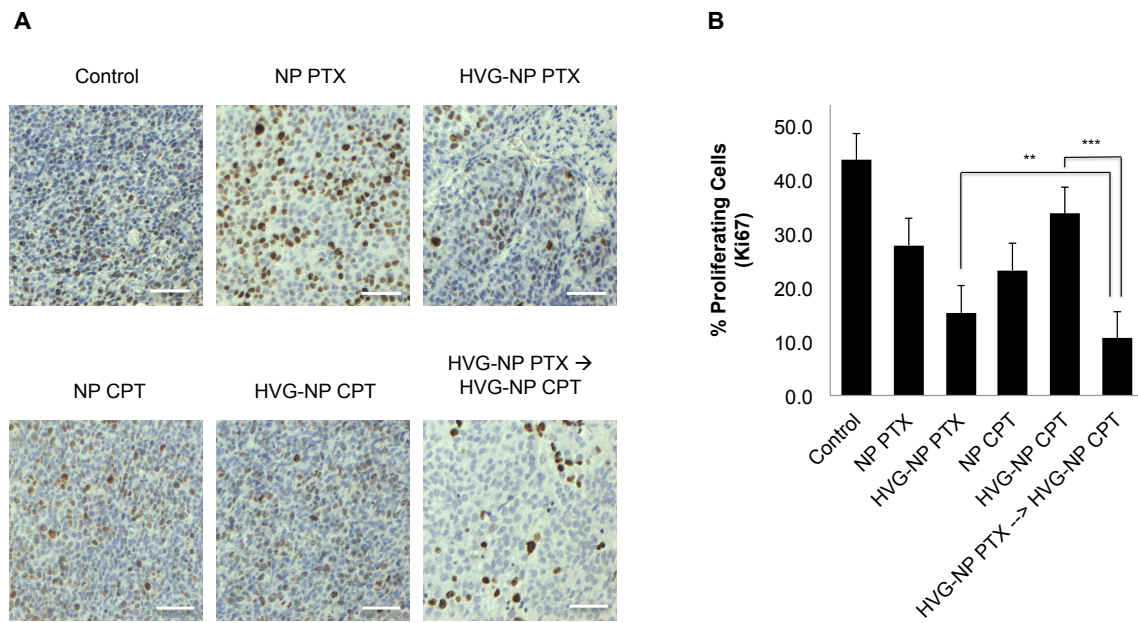


**Figure 5.6.** Immunohistochemical analysis of cell proliferation. C57BL6 mice with LLC tumors were treated with saline (control), NP PTX, HVGSSV-NP PTX, NP CPT, HVGSSV-NP CPT, or sequential HVGSSV-NP PTX → HVGSSV-NP CPT for fourteen days. Paraffin sections were stained for cell proliferation via Ki67 nuclear protein (A). All sections were counterstained with hematoxylin. Dark stained nuclei were scored as positive, and blue nuclei were scored as negative. Zeiss Axiophot, 10x magnification, scale bar indicates 100  $\mu$ m. Percentage of proliferating cells in all treatment groups (B). Bars show mean and SE for n=3, unpaired Student's t test ( $p < 0.05$ ).

Sequentially targeted treatment achieved the greatest number of caspase-3 positive apoptotic cells, with over 5 times higher levels of apoptosis compared to both monotherapy and untreated controls (Figure 5.7A,B).

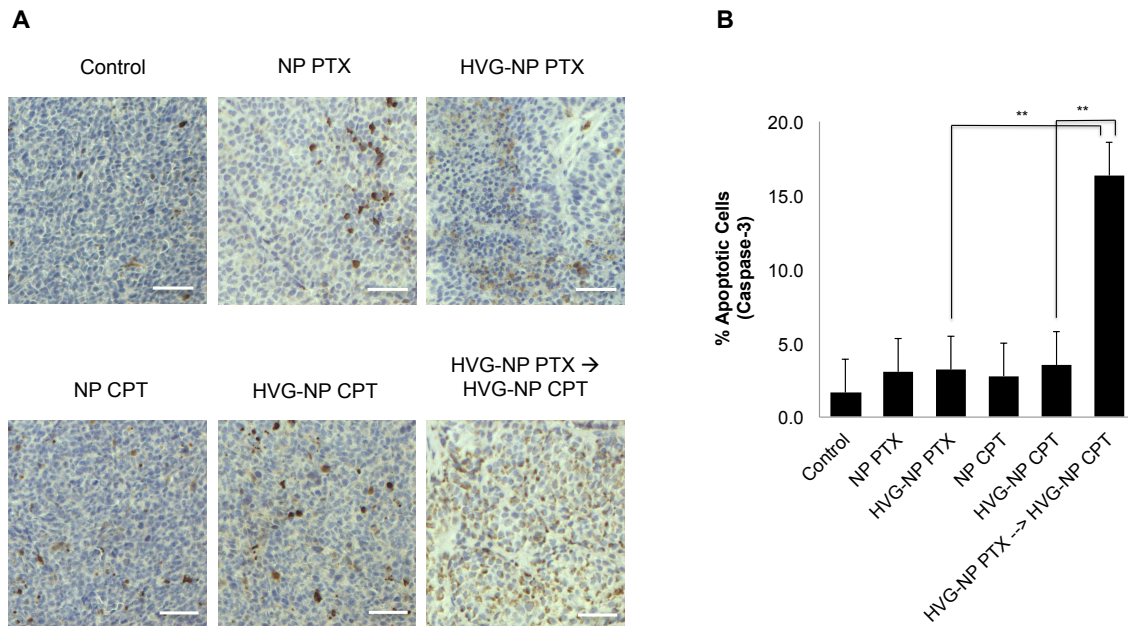


**Figure 5.7.** Immunohistochemical analysis of cell death. C57BL6 mice with LLC tumors were treated with saline (control), NP PTX, HVGSSV-NP PTX, NP CPT, HVGSSV-NP CPT, or sequential HVGSSV-NP PTX → HVGSSV-NP CPT for fourteen days. Paraffin sections were stained for apoptosis by presence of active caspase-3 (A). All sections were counterstained with hematoxylin. Dark stained nuclei were scored as positive, and blue nuclei were scored as negative. Zeiss Axiophot, 10x magnification, scale bar indicates 100  $\mu$ m. Percentage of apoptotic cells in all treatment groups (B). Bars show mean and SE for n=3, unpaired Student's t test ( $p < 0.05$ ).

Additionally, sequentially targeted groups displayed fewer blood vessels overall compared to targeted paclitaxel and camptothecin monotherapy and untreated controls (Figure 5.8A,B).

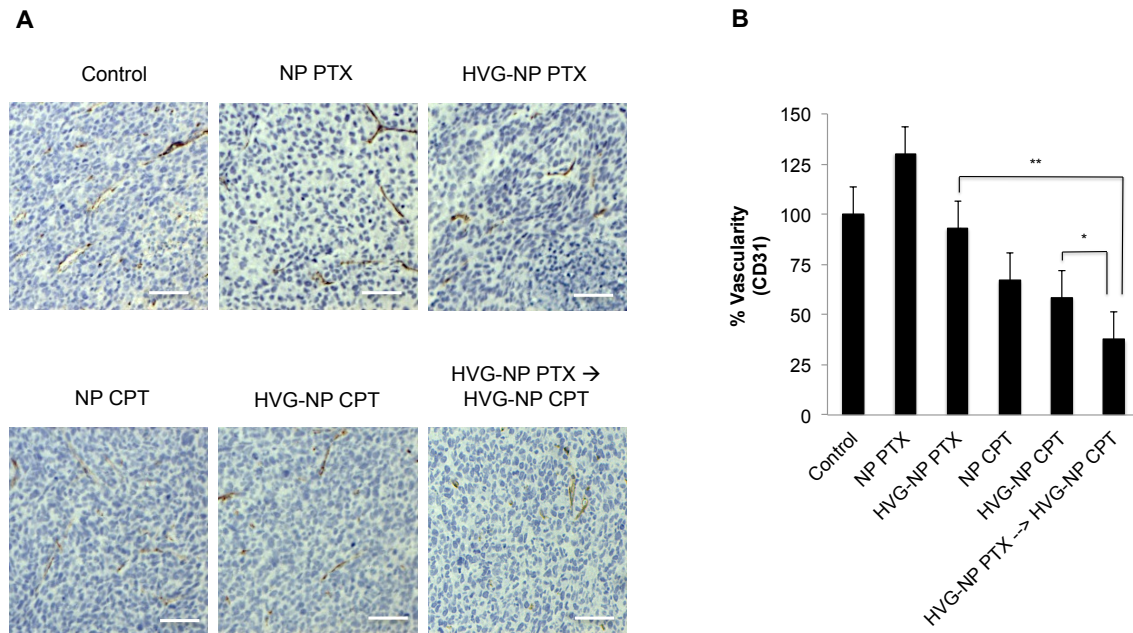


**Figure 5.8.** Immunohistochemical analysis of tumor vascularity. C57BL6 mice with LLC tumors were treated with saline (control), NP PTX, HVGSSV-NP PTX, NP CPT, HVGSSV-NP CPT, or sequential HVGSSV-NP PTX → HVGSSV-NP CPT for fourteen days. Paraffin sections were stained for CD31 expression on vascular endothelium (A). All sections were counterstained with hematoxylin. Dark stained nuclei were scored as positive, and blue nuclei were scored as negative. Zeiss Axiophot, 10x magnification, scale bar indicates 100  $\mu$ m. Percentage of vascular density in all treatment groups (B). Bars show mean and SE for n=3, unpaired Student's t test ( $p < 0.05$ ).

These results suggest that paclitaxel is more influential in inhibiting cell proliferation and camptothecin is driving the anti-angiogenic effect by reducing the number of blood vessels, thus inhibiting access to nutrients and growth factors necessary for continued tumor growth. Therefore, targeted sequential treatment with these two



drugs produces a more powerful effect than either drug alone. This optimized effect may be due to paclitaxel enhancing sensitivity to camptothecin, resulting in cells undergoing G2/M phase arrest and inducing apoptotic cell death. Subsequent administration of camptothecin results in a decrease in vascular density and reduction in blood flow available to tumors, further enhancing apoptotic effects produced by exposure to paclitaxel. In addition to these effects, decreased cell proliferation observed in the sequential sequence validate results from *in vitro* studies (see chapter 3) where treatment with paclitaxel followed by camptothecin produced the greatest changes in microtubule morphology and decreased the number of proliferating cells. These results jointly suggest enhanced sensitivity of cells to camptothecin after treatment with paclitaxel and indicate this drug sequence as having the greatest biological effect *in vitro* and *in vivo*.

Prior studies using the nanosponge delivery system have demonstrated the importance of targeting and the unique features of the nanosponge for supporting drug solubilization and release, resulting in greater drug efficacy.<sup>10</sup> This study investigated the feasibility of tumor-specific delivery and metronomic release of paclitaxel and camptothecin to determine the optimum drug combination and sequence for treating lung cancer. Initial studies (see chapter 3), examined the role of drug combination and sequence *in vitro*, in both mouse and human lung cancer cell lines, with synthesized untargeted nanosponges loaded with either paclitaxel (NP PTX) or camptothecin (NP CPT). Results showed not only that paclitaxel and camptothecin combination therapy produced the greatest G2/M phase arrest compared to monotherapy, but also that sequential administration of NP PTX followed by NP CPT further enhanced caspase-dependent cell death compared to simultaneous administration. Paclitaxel, more so than

camptothecin, was observed to drive cells into G2/M phase arrest and subsequent apoptosis. Further studies are necessary to determine the molecular basis for this effect in lung cancer. Sequential administration (NP PTX → NP CPT) of nanoparticle drug delivery systems resulted in greater cell death and decreased cell proliferation.

These results were validated in an *in vivo* mouse model of lung cancer after tumor binding of HVGGSSV functionalized targeted nanoparticles (Figure 5.1A-B) were confirmed. The targeting enabled nanoparticles to be selectively and specifically guided to tumors within 24 hrs after injection (Figure 5.2). TEM images showed preferential intracellular accumulation of Nanogold<sup>®</sup> functionalized targeted nanoparticles (Figure 5.1C) in tumor vascular endothelial cells at 24 hrs compared to untargeted controls (Figure 5.3). Use of the targeted nanoparticle drug delivery system in a sequential paclitaxel → camptothecin scheme demonstrated greater cell death, decreased cell proliferation and vascular density (Figure 5.7, 5.6, 5.8), translating to increased therapeutic efficacy in an *in vivo* lung cancer model. *In vitro* studies (see chapter 3) showed that the greatest changes in microtubule morphology were seen in cells exposed to paclitaxel → camptothecin sequential treatment, and this specific order suggests an increased sensitivity to camptothecin following paclitaxel exposure. Based on these results, the best drug combination and sequence was selected for targeting and therapeutic studies *in vivo*. Therapeutic efficacy studies conducted with sequential HVGGSSV targeted NP PTX and NP CPT showed 2.3 fold greater tumor growth delay in combination versus monotherapy treated groups, and 4.2 fold greater delay compared to untargeted and systemic (free) drug controls (Figure 5.4). Additionally, effects of these two drugs in combination on tumor angiogenesis were studied to determine changes in

vascular density (Figure 5.8A,B). Tumor neovasculature presents an attractive therapeutic target, with its role in providing nutrients and growth factors to growing tumors, as well as abnormally permeable architecture.<sup>29</sup> Disrupting blood flow to tumors provides a key element in many therapies as it diminishes tumor access to vital growth factors needed for continued growth, invasion and metastasis. Drugs with anti-angiogenic properties, like camptothecin, provide not only cytotoxic effects to tumor cells, but also damage their associated vasculature, providing multiple benefits as demonstrated. Moreover, use of nanoparticle carriers with controlled and sustained low dose drug release allows for metronomic chemotherapy, which has been shown to enhance anti-angiogenic effects.<sup>30</sup>

### ***Conclusion***

In conclusion, sequential paclitaxel → camptothecin chemotherapy exhibited a ‘priming’ effect on lung cancer cells that enhanced camptothecin’s effect on cells when given second. Nanosponge functionalization with targeting and imaging agents, sustained drug release profiles, and improved water solubility make them ideal for metronomic chemotherapy. Tumor-specific targeting of nanosponges to radiation-induced receptors increased bioavailability and enhanced therapeutic efficacy. Additionally, radiation treatment is commonly included with many chemotherapy regimens, and presents a clinically relevant opportunity for combining nanomedicine treatments with radiosensitizing drugs like paclitaxel and camptothecin.

## References

1. Chabner B.A., Roberts T.G. Timeline - chemotherapy and the war on cancer. *Nat. Rev. Cancer* 2005, 65-72.
2. Hallahan D.E., Qu S.M., Geng L. et al. Radiation-mediated control of drug delivery. *Am. J. Clin. Oncol.* 2001, 24, 473-480.
3. Rosa D.D., Ismael G., Dal Lago L., Awada A. Molecular targeted therapies: lessons from years of clinical development. *Cancer Treat. Rev.* 2008, 34, 61-80.
4. Steichen S.D., Caldorera-Moore M., Peppas N.A. A review of current nanoparticle and targeting moieties for the delivery of cancer therapeutics. *Eur. J. Pharm. Sci.* 2013, 48, 416-427.
5. Wang A.Z., Langer R., Farokhzad O.C. Nanoparticle Delivery of Cancer Drugs. *Annu. Rev. Med.* 2012, 63, 185-198.
6. Park J.H., Lee S., Kim J.H., Park K., Kim K., Kwon I.C. Polymeric nanomedicine for cancer therapy. *Prog. Polym. Sci.* 2008, 33, 113-137.
7. van der Ende, A.E., Kravitz E.J., Harth E. Approach to formation of multifunctional polyester particles in controlled nanoscopic dimensions. *J. Am. Chem. Soc.* 2008, 130, 8706-8713.
8. van der Ende A.E., Sathiyakumar V., Diaz R., Hallahan D.E. and Harth E. Linear release nanoparticle devices for advanced targeted cancer therapies with increased efficacy. *Polym. Chem.* 2010, 1, 93-96.
9. van der Ende A., Croce T., Hamilton S., Sathiyakumar V. and Harth E. Tailored polyester nanoparticles: post-modification with dendritic transporter and targeting units via reductive amination and thiol-ene chemistry. *Soft Matter* 2009, 5, 1417-1425.
10. Passarella R.J., Spratt D.E., van der Ende A.E. et al. Targeted nanoparticles that deliver a sustained, specific release of paclitaxel to irradiated tumors. *Cancer Res.* 2010, 70, 4550-4559.
11. Hallahan D.E., Geng L., Cmelak A.J. et al. Targeting drug delivery to radiation-induced neoantigens in tumor microvasculature. *J. Control Release.* 2001, 74, 183-191.
12. Hariri G., Yan H.P., Wang H.L., Han Z.Z., and Hallahan D.E. Radiation-guided drug delivery to mouse models of lung cancer. *Clin. Cancer Res.* 2010, 16, 4968-4977.

13. Wang H.L., Yan H.P., Fu A., Han M.J., Hallahan D., Han Z.Z. TIP-1 translocation onto the cell plasma membrane is a molecular biomarker of tumor response to ionizing radiation. *PLoS One* 2010, 5.
14. Weigel T.L., Lotze M.T., Kim P.K., Amoscato A.A., Luketich J.D., Odoux C. Paclitaxel-induced apoptosis in non-small cell lung cancer cell lines is associated with increased caspase-3 activity. *J. Thorac. Cardiovasc. Surg.* 2000, 119, 795-803.
15. Joung Y.K. and Park K.D. Controlled release systems of growth factors using heparinized polymeric carriers. *Tissue Eng. Regener. Med.* 2008, 5, 156-164.
16. Pommier Y. Drugging topoisomerases: lessons and challenges. *ACS Chem. Biol.* 2013, 8, 82-95.
17. Pommier Y., Leo E., Zhang H.L. and Marchand C. DNA topoisomerases and their poisoning by anticancer and antibacterial drugs. *Chem Biol.* 2010, 17, 421-433.
18. Pommier Y. DNA topoisomerase I inhibitors: chemistry, biology, and interfacial inhibition. *Chem. Rev.* 2009, 109, 2894-2902.
19. Pommier Y. Topoisomerase I inhibitors: camptothecins and beyond. *Nat. Rev. Cancer* 2006, 6, 789-802.
20. Kerbel R.S., Kamen B.A. The anti-angiogenic basis of metronomic chemotherapy. *Nat. Rev.* 2004, 4, 423-436.
21. Yurkovetskiy A.V., Fram R.J. XMT-1001, a novel polymeric camptothecin pro-drug in clinical development for patients with advanced cancer. *Adv. Drug Delivery Rev.* 2009, 61, 1193-1202.
22. Mu L., Elbayoumi T.A., Torchilin V.P. Mixed micelles made of poly(ethylene glycol)-phosphatidylethanolamine conjugate and D-alpha-tocopheryl polyethylene glycol 1000 succinate as pharmaceutical nanocarriers for camptothecin. *Int. J. Pharm.* 2005, 306, 142-149.
23. Rusan N.M., Fagerstrom C.J., Yvon A.M.C. and Wadsworth P. Cell cycle-dependent changes in microtubule dynamics in living cells expressing green fluorescent protein-alpha tubulin. *Mol. Biol. Cell* 2001, 12, 971-980.
24. Hughes J.R., Meireles A.M., Fisher K.H., et al. A microtubule interactome: Complexes with roles in cell cycle and mitosis. *PLoS Biol.* 2008, 6, 785-795.
25. Roberts J.R., Rowinsky E.K., Donehower R.C., Robertson J. and Allison D.C. Demonstration of the cell-cycle positions of Taxol-induced asters and bundles by sequential measurements of tubulin immunofluorescence, DNA content, and

- autoradiographic labeling of Taxol-sensitive and Taxol-resistant cells. *J. Histochem. Cytochem.* 1989, 37, 1659-1665.
26. Gan P.P., McCarroll J.A., Po'uha S.T., Kamath K., Jordan M.A. and Kavallaris M. Microtubule dynamics, mitotic arrest, and apoptosis: drug-induced differential effects of beta III-tubulin. *Mol. Cancer Ther.* 2010, 9, 1339-1348.
27. Wang H., Fu A., Han Z. and Hallahan D. Tax interacting protein (TIP-1): A potential radiation inducible receptor within cancer. *Int. J. Radiat. Oncol.* 2007, 69, S590-S591.
28. Neri D. and Bicknell R. Tumour vascular targeting. *Nat. Rev. Cancer* 2005, 5, 436-446.
29. Pasquier E., Kavallaris M. and Andre N. Metronomic chemotherapy: new rationale for new directions. *Nat. Rev. Clin. Oncol.* 2010, 7, 455-465.

## CHAPTER 6

### CONCLUSION AND FUTURE OUTLOOK

#### Conclusions

This work shows the development, optimization and evaluation of tumor-specific nanosponge drug delivery systems as chemotherapeutics. Nanoparticles made from biomedical polymers are commonly used in drug delivery applications because they allow for controlled release of drugs and degradation of nanoparticles over time. Development of nanoparticles for drug delivery and improved conjugating methods make it possible to design and create multifunctional nanoparticles for tumor-targeted drug delivery. Multifunctional nanoparticles composed of biodegradable polymers can be used to deliver controlled release of therapeutic drugs, functionalized with imaging agents for diagnostic purposes, and tumor-specific ligands for targeting of cancer. In this work, biodegradable polymeric ‘nanosponges’ were used to optimize targeted delivery of paclitaxel and camptothecin to lung cancer.

Linear polymers of narrow polydispersity were produced from tin (II) triflate catalyzed ring-opening polymerization methods in order to produce nanosponges with more uniform size distributions. These linear polymers showed greater monomer incorporation, higher yields, and faster reaction times at room temperature. By using ‘nanosponges’ produced from these optimized linear polyester copolymers, greater control over size distribution was able to be achieved producing higher quality nanoparticles for *in vitro* and *in vivo* applications. These nanosponges were then loaded

with hydrophobic chemotherapy drugs paclitaxel and camptothecin for enhanced solubility and drug release properties.

Initial studies were performed to determine the feasibility of using nanosponge encapsulated paclitaxel and camptothecin in combination treatment, and to determine the optimum drug combination and sequence for treating lung cancer. Here, the role of drug combination and sequence *in vitro*, in both mouse and human lung cancer cell lines, was investigated using synthesized nanosponges loaded with either paclitaxel (NP PTX) or camptothecin (NP CPT). Results showed not only that paclitaxel and camptothecin combination therapy produced the greatest G2/M phase arrest compared to monotherapy, but also that sequential administration of NP PTX followed by NP CPT further enhanced caspase-dependent cell death compared to simultaneous administration. Paclitaxel, more so than camptothecin, was observed to drive cells into G2/M phase arrest and subsequent apoptosis. The use of a sequential paclitaxel → camptothecin chemotherapy schedule was demonstrated to exhibit a “priming” effect on lung cancer cells that enhanced camptothecin’s effect on cells when given second.

Nanosponges were functionalized with  $\alpha_v\beta_3$  integrin targeting peptides such as cyclo RGD and a TIP-1 receptor targeting peptide HVGGSSV. These tumor targeting peptides allowed for greater tumor cell-specific delivery of drug-loaded nanosponges, optimizing bioavailability and therapeutic efficacy of chemotherapy drugs in tumors. In addition, nanosponge functionalization with targeting and imaging agents, sustained drug release profiles, and improved water solubility make them ideal for combination treatment and metronomic chemotherapy.



While nanosponges are a suitable platform for the delivery of hydrophobic chemotherapy drugs, other types of nanoparticles have also been used in the literature to achieve this purpose. Micelles and liposomes, due to their lipophilic properties, have been used to encapsulate a variety of hydrophobic drugs for the treatment of cancer and other diseases. These nanoparticles, however, are often difficult to produce in uniform size distributions due to processing methods, and consistent production of nanoparticles in smaller size ranges (under 200 nm) remains difficult. As a result, these types of nanoparticles are not ideal for intravenous therapeutic applications, but can be used in other situations where nanoparticle size is not as critical an issue. In addition to micelles and liposomes, other types of nanoparticles such as dendrimer-based scaffolds have also been used to deliver hydrophobic drugs. These branched structures offer the opportunity for covalent attachment of many drug molecules directly to the scaffold, with different methods of cleavage and release of the drugs. Consequently, achieving more gradual drug release profiles tends to be more difficult as these methods of cleavage and release support more “burst-like” drug release profiles. Nanoparticles made from proteins, such as albumin, offer another way to deliver drug molecules to tissues, but also show more rapid initial drug release profiles. Comparing lipophilic micelles and liposomes, dendrimer-based and protein-based nanoparticles to nanosponges reveals advantages for delivery of chemotherapy drugs such as improved size dimensions and drug release profiles. These observations highlight the significance of application type to the selection of a suitable nanoparticle platform. Thus, matching the requirements of a particular application with the attributes of a nanoparticle is key for producing a drug delivery system that produces the desired effects.

The use of synergistic drug combinations, sequences and ratios presents an opportunity for customization of treatments to patients. Selection of drugs and drug combinations that an individual patient responds to best, tumor-specific targeting, and optimized dosing and delivery of drugs are all effective ways to personalize treatment and improve the likelihood of positive therapeutic outcomes while reducing adverse side effects. While many of the developments in personalized medicine require genomic information and are tailored to individual patients at the genetic level, the use of synergistic drugs in combination with nanoparticle drug delivery can help support customization of therapy alongside genetic analysis, and provide an excellent complement to modern personalized medicine.

#### Future Aims

Future studies using these nanosponges should explore a large panel of small molecule drugs of varying molecular weight, solubility, and hydrophobicity in order to determine the drugs that are best suited to this particular drug delivery system. In vitro studies examining the effect of varying nanoparticle drug release rates with drug combinations should be performed to determine if drug release rates can be tailored to produce optimal drug combination schedules. Synergistic drug combinations could be used in sequences that are administered as single bolus injections, with the drug release properties of the nanoparticle serving as modulators of sequence administration. Similar studies can also be done using nanoparticles of varying crosslinking density to produce drug combination cocktails that provide synergistic ratios of multiple drugs to tumors over time.

Additional areas for further work involve the development of OPD containing polymers. Reduction in polydispersity among OPD containing polymers is an area that needs to be explored in order to produce nanoparticles with more consistent uniform size distributions. Further studies are also necessary to determine the ideal amount of OPD monomer incorporation in polyesters needed to produce polymers that are both water soluble while still retaining the ability to hold hydrophobic small molecule drugs. These polyesters also hold the potential for producing nanoparticles that can encapsulate hydrophilic drugs and small molecules, and this possibility is also worthy of further consideration. The studies contained in this work offer a potential starting point for investigating these opportunities in future works.

APPENDIX

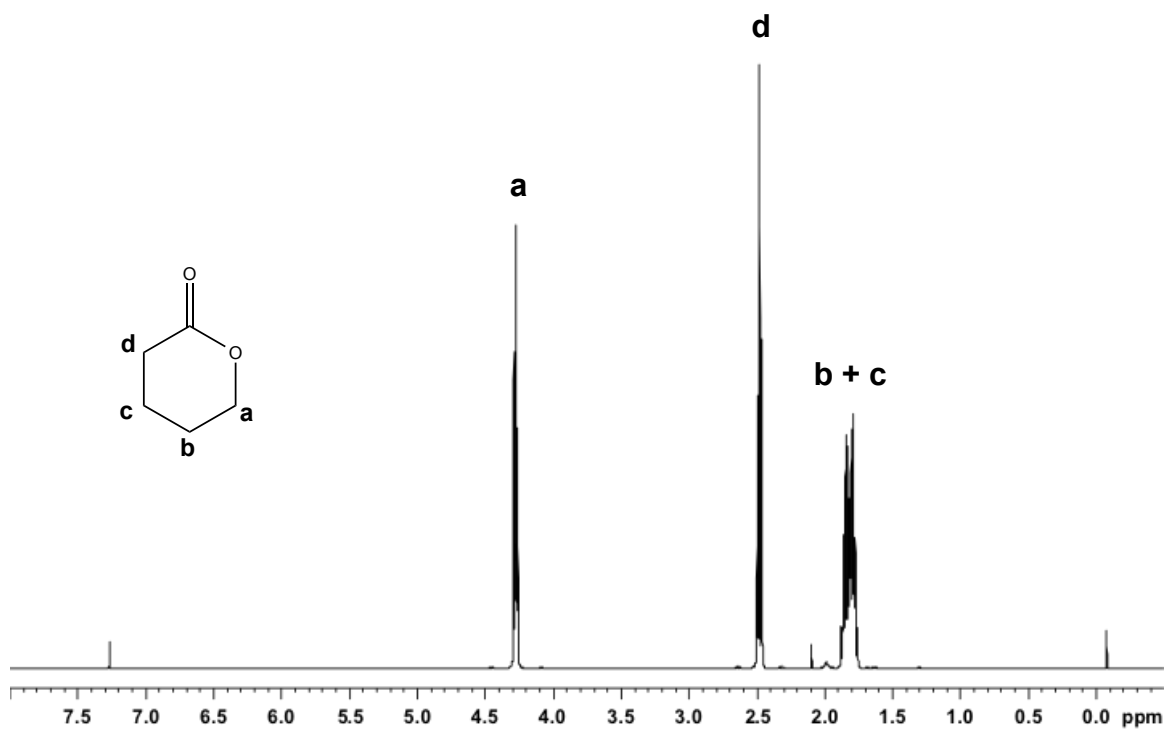
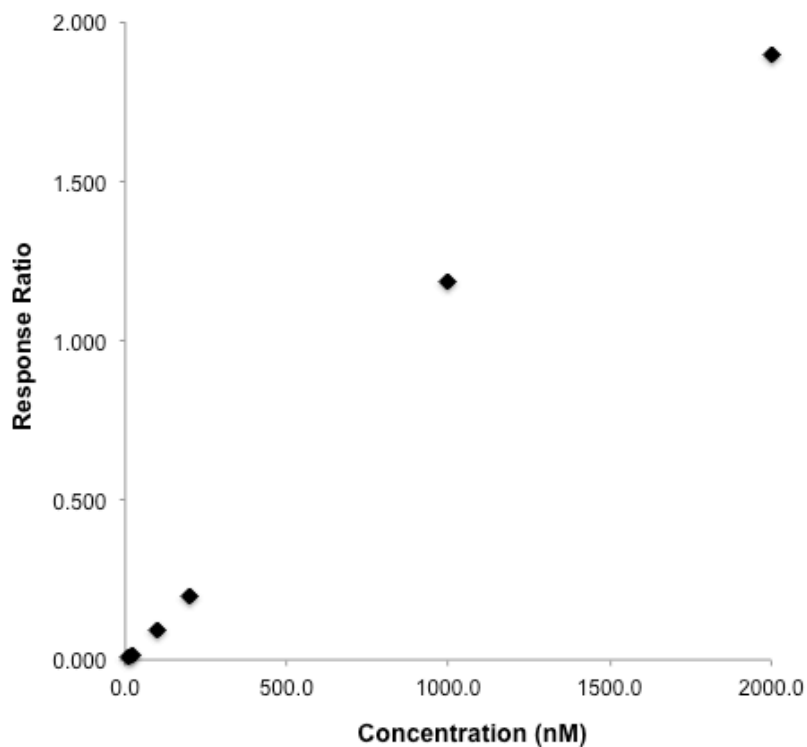


**Figure A.**  $^1\text{H}$  NMR of  $\delta$ -valerolactone monomer in  $\text{CDCl}_3$ .

## Drug Quantification

A.

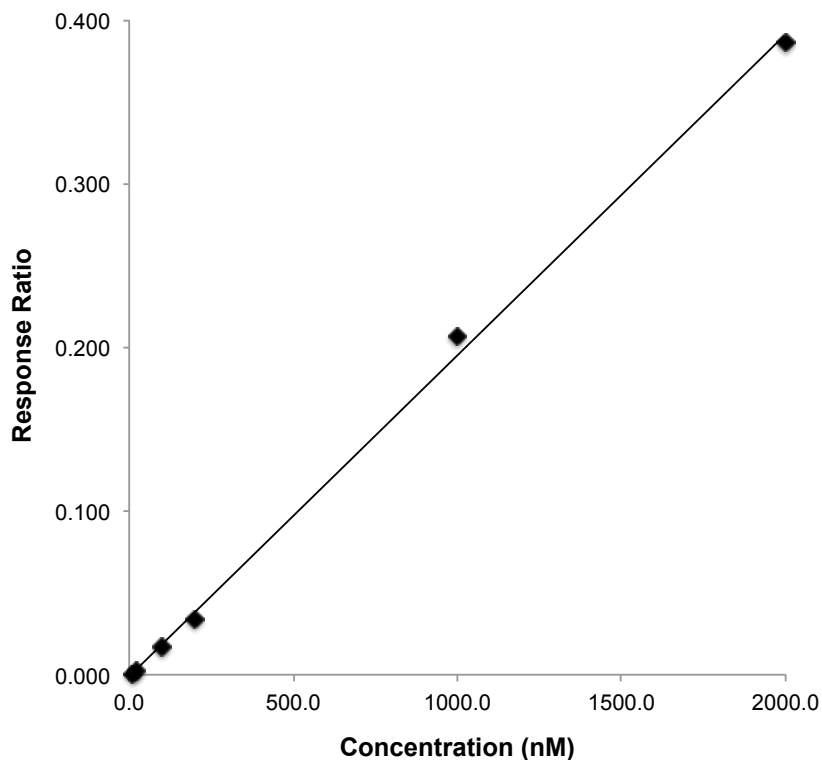


B.

Standard	Specified Concentration (nM)	Calculated Concentration (nM)	% Diff
P1	2000.0	1850.6	-7
P2	1000.0	1159.2	16
P3	200.0	196.7	-2
P4	100.0	94.0	-6
P5	20.0	19.1	-5
P6	10.0	10.4	4

**Figure B.** Calibration curve for paclitaxel analyte using docetaxel as internal standard. Paclitaxel (internal standard, Docetaxel) was extracted from tumor tissue homogenate, producing a linear calibration curve over the dynamic range of 10-2000 nM with an  $r^2$  coefficient of 0.9885. Samples were run in triplicate at concentrations of 10, 20, 100, 200, 1000 and 2000 nM. (A) Paclitaxel standards show a linear fit over 10-2000 nM range. (B) Accuracy of paclitaxel standards extracted from tumor tissue.

A.



B.

Standard	Specified Concentration (nM)	Calculated Concentration (nM)	% Diff
C1	2000.0	2014.1	1
C2	1000.0	1080.1	8
C3	200.0	180.2	-10
C4	100.0	97.1	-3
C5	20.0	21.3	7
C6	10.0	9.7	-3

**Figure C.** Calibration curve for camptothecin analyte using SN-38 as internal standard. Camptothecin (internal standard, SN-38) was extracted from tumor tissue homogenate, producing a linear calibration curve over the dynamic range of 10-2000 nM with a slope and intercept of  $y = 0.0002x - 0.001$  and an  $r^2$  coefficient of 0.9985. Samples were run in triplicate at concentrations of 10, 20, 100, 200, 1000 and 2000 nM. (A) Camptothecin standards show a linear fit over 10-2000 nM range. (B) Accuracy of camptothecin standards extracted from tumor tissue.

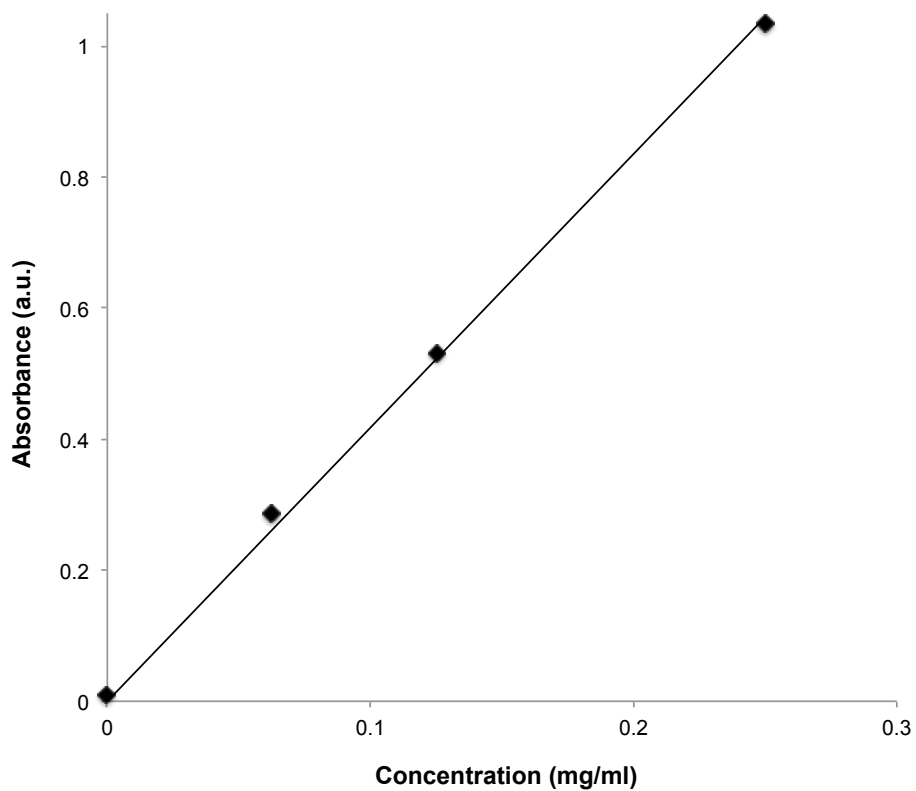


**Figure D.** Calibration curve for camptothecin using UV-Vis spectrophotometry. Camptothecin was dissolved in DMSO at varying concentrations and absorbance was measured using UV-Vis NanoDrop. Samples were run in triplicate and a linear calibration curve was produced with a slope and intercept of  $y = 4.177x + 0$  and an  $r^2$  coefficient of 0.99841.

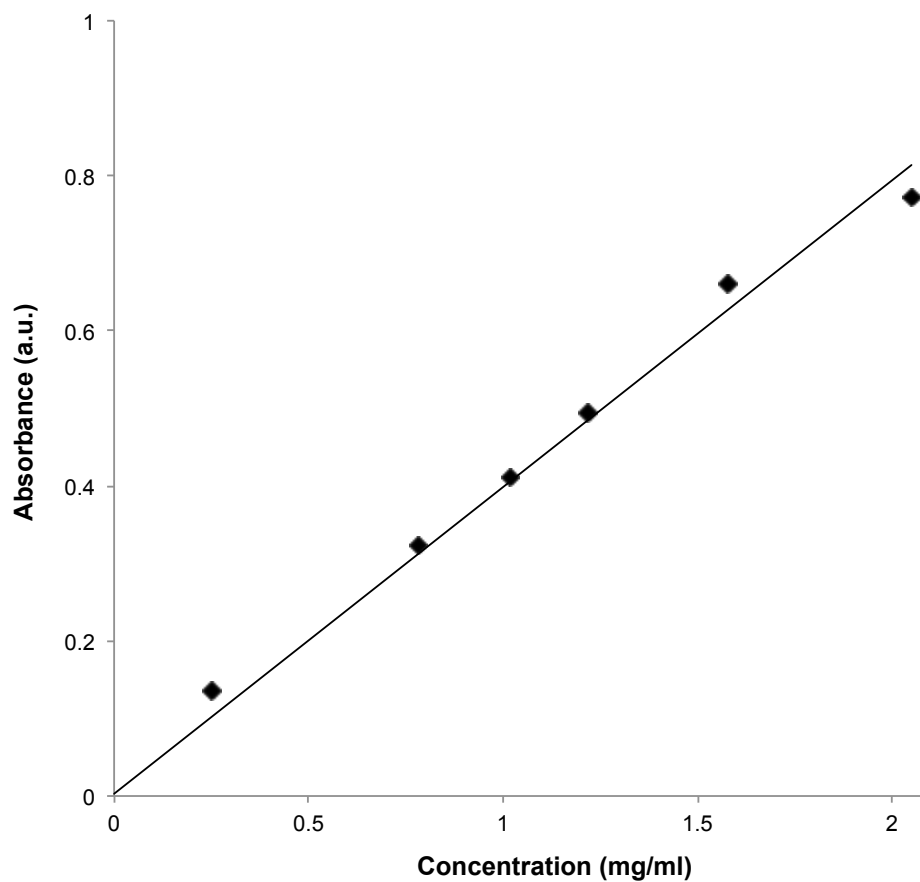


**Figure E.** Calibration curve for paclitaxel using UV-Vis spectrophotometry. Paclitaxel was dissolved in DMSO at varying concentrations and absorbance was measured using UV-Vis NanoDrop. Samples were run in quadruplicate and a linear calibration curve was produced with a slope and intercept of  $y = 0.3956x + 0.0029$  and an  $r^2$  coefficient of 0.98689.